Automated Tape Placement and Plasma Surface Modification for High-Performance Hybrid Thermoplastic Composites

A Dissertation Presented for the

Doctor of Philosophy

Degree

The University of Tennessee, Knoxville

Georges Chahine

December 2025

Copyright © 2025, by Georges Chahine

All Rights Reserved

DEDICATION

To my parents, Rosette and Hammam, who kept believing I was doing something important-even when I couldn't quite explain what. To my brother, Ricardo, for reminding me there's more to life than code, composites, and caffeine. To my advisor, Dr. Uday Vadiya, for asking questions that came with just enough answers to keep me up at night. And to my friends, for sticking around through the disappearing acts, the data spirals, and the "I swear I'll be done soon" lies. This work is for all of you, thank you for being the constants in a very nonlinear equation.

ACKNOWLEDGMENTS

First and foremost, I owe the deepest gratitude to my advisor, Dr. Uday Vaidya. Working with you has been one of the most enriching experiences of my life-not only because of your scientific guidance, but because of the kind of person you are. Your humility, wisdom, and unwavering encouragement have shaped the way I approach research and life. You didn't just advise a dissertation; you mentored a person. Thank you for believing in me when I doubted myself, for your calm presence in moments of chaos, and for always making time-even when you had none. I leave this PhD with more than technical skills, I leave with inspiration.

Further, I would like to thank my dissertation committee, Dr. Merlin Theodore. Dr. Claudia Rawn, and Dr. Krishnan Veluswamy, their great support and allowing me to use their facilities for my thesis work.

I am immensely grateful for the financial support and research opportunities provided by the U.S. Department of Energy (DOE), the Southeastern Advanced Machine Tools Network (SEAMTN), the Department of Defense (DoD), the Institute for Advanced Composites Manufacturing Innovation (IACMI), the Manufacturing Demonstration Facility (MDF), Oak Ridge National Laboratory (ORNL), and the University of Tennessee. This work would not have been possible without your generous backing and resources.

To Dr. Umesh Marathe, Dr. Pritesh Yeole, and Dr. Romeo Fono Tamo-thank you for your mentorship and guidance across so many scales, both technical and personal. To Dr. Ryan Spencer and Benjamin Schwartz, who not only introduced me to the world of composites, but also to the American way of life-thank you for shaping both my professional and cultural journey.

To my lab mates and colleagues, thank you for your help during testing, your camaraderie, and your tolerance for stress-induced rants. Special thanks to Yalcin Meraki,

Abdallah Barakat, and Chase Muccllar for the hands-on support and shared lab chaos. And to Dr. Hicham Ghossein-your industrial mentorship, guidance, and belief in my potential have been instrumental. But more than that, I am deeply grateful to you and your family for standing beside me during hard times and embracing me with unconditional love and support.

To my roommates, Marc Ghazal and Moula Hanna, thank you for being more than roommates. You were family, travel companions, and co-survivors of life's many storms. You walked beside me through breakdowns, breakthroughs, and all the moments in between. Without your humor, late-night talks, and shared existential dread, this ride would've been unbearable. You made a foreign land feel like home.

To all my friends and extended family who reminded me of the real meaning of existence-thank you for pulling me out of my academic echo chamber when I needed it most. You helped me keep perspective when all I could see was a blinking cursor.

To my brother, Dr. Ricardo Chahine, your presence has been my steady anchor. You reached the title first, and yet never let it be a competition-only motivation. Your strength, patience, and constant belief in me were my daily bread. All the love to you.

And finally, to my grandmother Farida, who taught me-without ever needing to say that life is not for the weak. That no matter how heavy it gets, we live it with love and peace. To my father Hammam Chahine and my mother Rosette Sarkis-this moment was your dream long before it became mine. Your love, your sacrifices, and your belief in the impossible carried me through every setback. I am forever grateful for the foundation you built beneath my feet.

ABSTRACT

Thermoplastic composites have emerged as promising candidates for next-generation structural materials due to their recyclability, rapid processing, and superior impact and thermal performance. However, discontinuous fiber systems such as long fiber thermoplastics (LFTs) remain limited in directional reinforcement and load-transfer efficiency, restricting their use in demanding structural environments. This dissertation investigates an integrated approach to overcome these limitations through the Automated Tape Placement (ATP) overmolding of continuous carbon fiber-reinforced thermoplastics onto LFT substrates, atmospheric plasma surface modification to enhance interfacial bonding, and the development of a semi-empirical model to predict plasma-induced surface evolution.

In the first study, glass fiber (GF) reinforced polyphenylene sulfide (PPS) LFT substrates were overmolded with a single layer of unidirectional carbon fiber (CF)/PPS tape using an ATP robotic system. The hybrid structures exhibited significant mechanical enhancements compared with the baseline LFT: tensile strength increased by 129% (from 51 MPa to 117 MPa), flexural strength by 192% (from 99 MPa to 290 MPa), and interlaminar shear strength by 33%, reaching an average interface strength of 7.52 ± 0.34 MPa. Differential scanning calorimetry confirmed stable crystallinity near 33%, and thermogravimetric analysis indicated thermal stability up to 425 °C, verifying compatibility under ATP conditions. Finite element simulations predicted a further 60% gain in flexural strength with five CF-tape layers, highlighting the scalability of this hybrid approach.

The second study addressed interfacial adhesion through atmospheric plasma treatment of low-melt polyaryletherketone/carbon fiber (LMPAEK/CF) unidirectional tapes. Plasma activation increased surface polarity and oxygen concentration, forming hydroxyl and carboxyl groups confirmed by X-ray Photoelectron Spectroscopy (XPS) and Fourier Transform Infrared Spectroscopy (FTIR). Atomic Force Microscopy (AFM) showed a

pronounced increase in nanoscale roughness, while contact angle measurements revealed over a 40% reduction, confirming improved wettability. Composites fabricated from treated tapes exhibited higher load-bearing capacity, with increases of 7.6% in tensile strength, 18% in flexural strength, and 18.7% in interlaminar shear strength, accompanied by a shift from delamination to cohesive matrix-dominated failure.

The final study established a semi-empirical model to describe the evolution of surface roughness and contact angle as functions of plasma exposure time, energy density, and thermal conductivity. The model achieved $R^2 > 0.95$ (meaning it explained more than 95% of the variation in the measured data) and errors below 5% compared with experimental AFM and goniometric measurements, accurately capturing the nonlinear transition between surface activation and saturation.

Collectively, this work presents a validated pathway for manufacturing high-performance, recyclable hybrid thermoplastic composites. The combination of ATP overmolding, plasma-assisted surface engineering, and semi-empirical modeling provides both mechanistic understanding and practical tools for optimizing interfacial behavior, enabling scalability, reliability and sustainable composite structures for automotive, aerospace, and advanced industrial applications.

Keywords: Long Fiber Thermoplastic, Automated Tape Placement (ATP), Overmolding, Atmospheric Plasma Treatment, Finite Element Analysis, Surface Roughness Modeling.

TABLE OF CONTENTS

1. CHAPTER 1 1

1.1 Background and Motivation 2

1.2 Long Fiber Thermoplastics and Extrusion Compression Molding 5

1.3 Automated tape placement in composites manufacturing 6

1.4 Overmolding with Continuous Reinforcement 8

1.5 Atmospheric Plasma Surface Treatment of Thermoplastic Composites 10

1.6 Surface Modeling of Plasma-Treated Interfaces 12

1.7 Research Objectives and Organization 15

2. CHAPTER 2 20

Abstract 21

2.1 Introduction 22

2.2 Materials and Methods 25

2.2.1 Materials 25

2.2.2 Processing 25

2.2.3 Testing and Analysis 28

2.3 Materials and Methods 31

2.3.1 Interface Bonding 31

2.3.2 Thermal Analysis 31

2.3.3 Flexural testing and morphology 33

2.3.4 (Through-Thickness) Tensile Strength 35

2.3.5 Tensile (in-plane) test 37

2.3.6 Drop-Tower (low-Velocity) Impact Test 41

2.3.7 Finite Element Analysis 44

Summary 49

3. CHAPTER 3 53
Abstract 54
3.1 Introduction 54
3.2 Experimental 56
3.2.1 Materials 56
3.2.2 Plasma Treatment of the UD tape 57
3.2.3 Development of ATP-based composite laminate 57
3.2.4 Characterization of LMPAEK/UD tape 58
3.2.4.1 Contact angle study 58
3.2.4.2 Electron microscopy of LMPAEK/CF UD tape 59
3.2.4.3 Fourier Transform infrared of LMPAEK/CF UD tape 59
3.2.5 Characterization of the treated and untreated composites 60
3.3 Results 62
3.3.1 Characterization of the LMPAEK/CF UD tape 62
3.3.2 Characterization of the treated and untreated composites 71
Summary 81
4. CHAPTER 4 83
Abstract 84
4.1 Introduction 85
4.2 Experimental Section 87
4.2.1 Material 87
4.2.2 Plasma Treatment Mechanism 88
4.2.3 Contact Angle and Atomic Force Microscopy Measurements 90
4.3 Numerical Methodology 91
4.3.1 Overview 91

4.3.2 Surface Roughness Model 92

4.3.3 Contact Angle Model 94

4.4 Numerical Methodology 96

4.4.1 Atomic Force Microscopy Model 99

4.4.2 Contact Angle Model 104

4.5 Discussions 106

Summary and Future Work 107

References 109

Overall Summary 123

Vita ` 124

LIST OF TABLES

Table 2.1..... Dimensions and peak load of the overmolded samples tested under flatwise tension.While thickness normalization was applied in the stress calculations, variability in peak load remained due to factors such as interfacial bonding quality and adhesive layer consistency. 38

Table 2.2. Results summary of the tested specimens. 41

Table 2.3. Materials properties for the finite element model collected from the experimental measurement and from the Material Data Sheet (MDS) of the material provided by the manufacturer[66].....45

Table 2.4. Failure limits of the CF-Tape. 48

Table 3.1 Surface Composition (at. %) for the U and T LMPAEK/CF UD tape for element C,O and N. 68

Table 3.2 T5 and T10 temperatures for composite C_U and C_T.....72

Table 3.3. Storage moduli and glass transition temperature by dynamic mechanical analysis. 74

Table 4.1.Material properties of LMPAEK/CF. 88

Table 4.2. A summary of Atmospheric plasma treatment parameters.....90

LIST OF FIGURES

Figure 1.1. Extrusion-compression molding process. (a) The LFT is placed in the hopper and fed at a constant speed. (b) It is melted during extrusion through a single-screw extruder. (c) The molten LFT is transformed into a charge. (d) The charge is compressed under specific pressure to form the final part (matching the mold shape). 5

Figure 1.2. Plasma treatment modifies the polymer surface by creating micro and nanoscale textures, and introducing reactive groups, which allows biomolecules to bind directly through physical and covalent interactions without the need for linkers. 11

Figure 2.1 Chemical structure of Polyphenolic sulfide (PPS). 24

Figure 2.2 Schematic of the extrusion compression molding process for LFT composites. G-LFT are melted and conveyed through a screw extruder to form a charge, which is then transferred into a mold cavity and compressed into the final part shape. 26

Figure 2.3. Illustration of the ATP robot: 1) CF-Tape 12.7mm (½- inch), 2) The compaction roller, 3) The HGT, 4) The G-LFT substrate 5) The overmolded part. (a) The G-LFT substrate before overmolding. (b) The CF-Tape will pass through a guide slot, the tape will be heated with the HGT, and in-situ consolidated on the substrate with a load of 64.5 Kg (140 lb). applied by the compaction roller. 27

Figure 2.4. Flexural setup for the overmolded specimen, the tape was from the bottom side, as CF performed in Tensile better than compression. 28

Figure 2.5 (a) Sample preparation of the overmolded part and surface modification of the aluminum end tabs. Aluminum tabs were modified to achieve failure on the interface and not in the glue part. (b) Glue placed on the end tabs and specimens were mounted for out of plane tension test. 30

Figure 2.6. (a) OM image showing the bonding adhesion on the interface after the overmolding process between the G-LFT and the CF-Tape. (b) A slight delamination has been

noticed on the interface of an ILSS tested sample, the GF/PPS attached on the failed tape evidence the strong bonding on the interface. 32
Figure 2.7 (a) DSC of G-LFT and G-LFT/CF-Tape, showing the melting point (285°C) and the crystallization point (225°C), (b) TGA analysis of G-LFT and G-LFT/CF-Tape showing that the degradation temperature of the composites started at 425°C.....34
Figure 2.8 (a) The average flexural properties of the manufactured composites with and without tape. An increment of 192% in flexural strength and 120% in modulus has been noticed along the fiber direction of the tape. (b) Load versus displacement for the three-point bending testing illustrating a brittle failure in the G-LFT and the overmolded samples. 35
Figure 2.9. SEM image of the fractured overmolded G-LFT/CF-Tape sample after flexural testing. The image shows crack initiation in the G-LFT region and slight delamination at the interface, indicating good bonding. Fiber breakage within the G-LFT and matrix remnants on the CF-Tape surface suggest a mixed cohesive-interfacial failure mode.....36
Figure 2.10 Load-displacement curves from flatwise tensile tests of G-LFT/CF-Tape overmolded specimens. The sudden load drops indicate brittle failure behavior. Variations in peak load are attributed to differences in sample thickness, while all specimens showed similar failure mechanisms. 37
Figure 2.11 Flatwise tensile strength of the G-LFT/CF-Tape overmolded part. (b) A partial failure of the CF-Tape on the interface between the G-LFT and each patch of the tape processed on the ATP. 38
Figure 2.12 Tensile properties of the G-LFT and G-LFT/CF-Tape. An improvement of 128% and 62% in tensile strength and modulus, respectively, were achieved in the G-LFT/CF-Tape compared to G-LFT.....39
Figure 2.13 Load versus displacement for the tensile test showed the failure behavior for the G-LFT and the G-LFT/CF-Tape, demonstrating a strong in-plane bonding on the interface. 39

Figure 2.14. SEM image of the fractured G-LFT/CF-Tape interface after tensile testing. Matrix cracking and carbon fiber breakage are observed due to strong interfacial bonding, which enabled effective load transfer into the CF-PPS layer. The resulting fiber and matrix failure confirms good adhesion at the interface and the activation of composite action rather than premature delamination.....40
Figure 2.15 10.16 x 15.24 cm (4x6 in) G-LFT tested composite panels. (b) 10.16 x 15.24 cm (4x6 in) G-LFT/CF-Tape tested panel. A vertical crack along the direction of the CF orientation was observed in the overmolded sample. The crack orientation was observed due to the delamination of CF tape.....42
Figure 2.16. Force-displacement curves from low-velocity impact (LVI) testing of G-LFT and G-LFT/CF-Tape specimens. Both samples show a loading-unloading response typical of hybrid composites. The overmolded sample exhibits greater deformation and slightly lower peak force, attributed to energy dissipation through interfacial delamination and fiber-matrix failure mechanisms. Blue G-LFT/CF-Tape specimens, orange G-LFT specimens.....43
Figure 2.17 LVI Force/Energy-time response depicting the damage initiation energy "E_i" at both peaks and the damage propagation energy "E_A" at the two minimal values during unloading phases. (a) G-LFT/CF-Tape specimens (b) G-LFT specimens.....44
Figure 2.18 Mesh distributions for G-LFT substrate and CF-Tape layer. The figure illustrates the mesh for the tested parts and the three-point bending mechanism as rigid bodies.....46
Figure 2.19 Comparison between experimental and numerical stress-strain curves for flexural testing of G-LFT and G-LFT/CF-Tape, demonstrating good agreement and validating the simulation model.....47
Figure 2.20 (A) Von Mises stress of the applied load, (B) deflection of the part. (C) and (D) failure monography of the CF-Tape layer numerically and experimentally respectively.....48

Figure 2.21. On top, Von Mises Stresses for the overmolded part with different number of CF-Tape layers. The stress range shows the ability of the overmolded parts of supporting more load by adding additional layers of tapes. On bottom, the corresponding failure response of each layer individually. From the left side, the single layer of tape failed quickly, however adding more layers distributed the load evenly through thickness and prevented progressive failure. 50
Figure 2.22. Numerical prediction of stress–strain behavior for G-LFT with increasing numbers of overmolded CF-Tape layers. The results show that adding CF-Tape layers progressively enhances the composite's stiffness and ultimate strength, indicating improved load-bearing capacity and more efficient stress distribution. 51
Figure 2.23. Normalized stress predictions showing the strengthening effect of multiple CF-Tape layers overmolded onto G-LFT, with up to 60% improvement after five layers. 51
Figure 3.1. Illustration of the treatment setup used to treat the LMPAEK/CF UD tape. The tape was treated at the same speed as the deposition rate of the ATP (76 mm/s). 57
Figure 3.2.Schematic depicting the ATP working principle. The LMPAEL CF- tape originates from the feedstock, is subsequently heated by the HGT, and undergoes in-situ consolidation as a specific load is applied through the compaction roller. 58
Figure 3.3. The contact angle for the treated tape as a function of treatment time: With the increase in plasma treatment time, the contact angle reduced drastically. Additionally, with the increase in contact angle after 15 sec treatment time, it increases again due to an excessive increase in surface roughness [67]. The right Y axis shows the increase in oxygen content on the surface (analysed from XPS spectra), i.e., polarity with treatment time. An increase in oxygen content on the treated tape surface was found to be nonlinear with treatment time, however, demonstrates the effectiveness of treatment. 63

Figure 3.4. Contact angle measurement optical image plasma untreated tape (a) and the treated tape (b). Reduced contact angle post plasma treatment is effect of formation of hydrophilic moieties on the surface of ATP tape, cleaner surface. 64
Figure 3.5. Possible chemical changes of LMPAEK/CF UD tape due to air plasma treatment [68, 69]. 64
Figure 3.6. FTIR spectrum of the LMPAEK/CF UD treated and untreated tape. Appearance of a new peak between 2160 and 2250 Cm^{-1}. The intensity of the hydroxylic group and C-O stretch and C-H stretch are higher in the T tape compared to U. 66
Figure 3.7 XPS survey spectrum (a) for the U and T LMPAEK/CF UD tape. The peaks intensity of Oxygen (O) and Nitrogen (N) are higher in the T samples compared to the U emphasizing the effect of plasma treatment on the surface. (b) deconvoluted XPS spectra for C 1s and O 1s. 67
Figure 3.8. SEM micrographs for U (a) and T (b) LMPAEK/CF UD tape: SEM micrographs depict nature of attack of plasma species. U (untreated tape) tape depicts uniform and coherent surface with no surface damage, whereas the plasma treated tape shows vivid feature i.e., increased surface roughness, deeper crevices, and blistering of LMPAEK in the T (treated tape) tape. 69
Figure 3.9. Comparative AFM topography imaging of LMPAEK/CF UD tape for both untreated (a, c) vs. treated (b, d) samples. Panels (a) and (b) depict 3D topography focusing on fiber-rich regions. Panels (c) and (d) are 2d images for polymer rich regions, illustrating changes in surface structure post-treatment. 71
Figure 3.10. 2D profile of polymer rich region of untreated (a) and treated (b) LMPAEK/CF UD Tape by AFM. 72
Figure 3.11. Thermogravimetric analysis for composite C_U and C_T 72

Figure 3.12 Visco-elastic performance of developed composites (a) storage modulus and (b) tan δ. 74
Figure 3.13. X-ray diffractogram for the developed composites C_T and C_U. 75
Figure 3.14 (a, b). Average interlaminar shear strength of the C_T and C_U. An improvement of 18.75% has been noticed in the C_T compared to C_U. Load vs displacement depicting the failure behavior of the ILSS samples. 76
Figure 3.15 (a, b). SEM images of failed ILSS samples of C_T and C_U respectively. Delamination was observed almost between each laminate in the C_U, and just in one spot for the C_T. 76
Figure 3.16 (a, b). Average flexural strength and modulus of C_T and C_U in accordance with ASTM D790. The flexural strength and modulus of C_T is 18% and 8.3% higher than C_U. Load vs displacement depicting the failure behavior of the flexural samples. 77
Figure 3.17 (a, b). Optical microscopy (OM) images show ASTM D790 acceptable failure behavior for the C_T, brittle failure mode in tension, and interlaminar failure mode in the C_U specimens, illustrating delamination in the samples. 78
Figure 3.18 (a, b). (a) Average tensile strength and modulus for C_T and C_U. An increase of 7.6% in strength and 8% in modulus has been noticed in the C_T. (b) Shows load versus displacement, illustrating the failure behavior of the tensile samples. 79
Figure 3.19 (a, b). SEM micrographs depicting failed samples during tensile test (a) CU and (b) CT. 79
Figure 4.1.Mechanism of Surface Roughness Induced by Plasma Treatment. 88
Figure 4.2.Flowchart of the numerical algorithm used to model plasma-induced surface roughness and contact evolution in LMPAEK. The process initializes with experimental surface roughness, contact angle and iteratively computes roughness at each step using material properties and plasma exposure parameters. 94

Figure 4.3 Surface roughness evolution over time under constant intensity of plasma exposure. From Top left to right, exposure time of 0s, 5s, 10s, etc. The surface roughness apparently increases until around 20s, then it reaches to a saturation point, where the surface roughness changes but within the same roughness range. 98
Figure 4.4.Surface roughness evolution as predicted by numerical modeling and validated by experimental AFM data, clearly illustrating rapid initial changes and subsequent stabilization phases critical for optimal plasma treatment time selection. 100
Figure 4.5. 2-D surface topography of the untreated LMPAEK/CF tape (0s) and treated (5s). Comparison between AFM-measured roughness distributions (a, b), and numerically simulated roughness profiles (c, d) for untreated (0s) and plasma-treated (5s) LMPAEK/CF surfaces. The numerical model effectively captures the increase in surface roughness observed experimentally after plasma treatment, demonstrating strong qualitative agreement. 101
Figure 4.6.The 3-D surface roughness comparison between experimental (a, b) and numerical (c, d) models provides a more detailed insight into the spatial variations induced by plasma treatment. 102
Figure 4.7.Comparison of experimental and numerical surface profiles for untreated and treated conditions. For the untreated surface, the MAE and MSE are approximately 4.62% and 2.29%, respectively, while for the treated surface, they decrease to approximately 3.69% and 2.12%, indicating improved numerical prediction accuracy after treatment. 103
Figure 4.8 illustrates the predicted and measured contact angles over plasma exposure time. The dual-term model, incorporating both exponential decay and hyperbolic tangent stabilization, accurately describes the rapid initial decrease in contact angle due to plasma-induced functionalization, followed by a gradual stabilization phase. 105

1. CHAPTER 1

INTRODUCTION

1.1 Background and Motivation

Thermoplastic composites have gained significant attention in structural applications due to their recyclability, rapid processing, and high damage tolerance [1]. Their potential to replace thermoset composite systems in demanding environments, such as automotive, aerospace, and industrial sectors, makes them a critical component of the shift toward lightweight and sustainable engineering solutions [2]. Within the class of thermoplastics, long fiber thermoplastics (LFTs) offer an appealing balance between mechanical strength and manufacturing versatility. Reinforced typically with glass fibers, LFTs exhibit excellent impact resistance, corrosion tolerance, and ease of forming into complex geometries using extrusion-compression or injection-compression molding [3, 4].

LFTs bridge the performance gap between short fiber compounds and fully continuous fiber composites. They contain fiber lengths typically ranging from 3 mm to 25 mm and aspect ratios between 300 and 1000 [5]. These dimensions allow LFTs to achieve mechanical properties suitable for semi-structural parts, provided that fiber lengths exceed the critical fiber length, which determines whether fibers can effectively carry load [6]. This length lc is defined as:

$$lc = \frac{\sigma_{max} \cdot d}{2\tau} \quad \text{(Eq 1.1)}$$

where σ_{max} is the tensile strength of the fiber, d is the fiber diameter, and τ is the interfacial shear strength. Fibers longer than lc ensure more efficient load transfer to the matrix, resulting in higher strength and stiffness [6].

However, LFTs remain limited by their discontinuous nature, which leads to challenges in achieving direction-specific reinforcement and consistent fiber alignment. Fiber orientation varies depending on mold geometry, flow behavior, and charge placement, often resulting in anisotropic or suboptimal properties [7]. Moreover, conventional LFT molding processes

rarely yield perfectly aligned fibers, which restricts their use in high-performance structural applications.

To address these limitations, hybrid manufacturing strategies have emerged, including overmolding continuous fiber-reinforced thermoplastic (CFRTP) tapes onto LFT substrates. This technique allows targeted reinforcement in regions prone to stress concentration, while preserving the processing benefits of LFTs. In particular, ATP has shown promise as a flexible robotic process capable of precisely depositing continuous fibers onto complex geometries [8, 9]. Traditionally used in aerospace, ATP provides localized control of reinforcement with reduced waste and labor, making it suitable for hybrid composite manufacturing.

ATP in thermoplastic applications faces barriers such as suboptimal tape consolidation and limited interfacial bonding, especially when combining dissimilar reinforcements. To enhance bonding at the fiber-matrix interface, atmospheric plasma treatment has emerged as a surface engineering method that modifies surface roughness and chemistry without altering the bulk properties of the tape. This treatment improves wettability, adhesion and offers a scalable route for improving consolidation quality in ATP-processed parts.

In parallel, the development of semi-empirical models for plasma-induced surface evolution enables more precise control of interface characteristics, reducing reliance on purely experimental approaches. Existing studies have largely described plasma treatment effects qualitatively, emphasizing general improvements in adhesion or wettability without establishing quantitative relationships between processing parameters and surface behavior. The semi-empirical framework, grounded in plasma energy flux, transient surface heating, and polymer relaxation kinetics, allows the estimation of surface roughness (Ra) and contact angle (θ) as functions of plasma power, exposure time, and material thermal properties. Such modeling is crucial for linking processing conditions to interfacial performance, enabling

rational optimization of plasma treatments across different thermoplastic systems. Despite growing research on plasma activation, there remains a clear gap in the literature: validated, parameter-dependent models for high-performance thermoplastics such as PPS and LMPAEK are still limited. Addressing this need provides both a predictive understanding of surface modification mechanisms and a scalable tool for improving interface reliability in hybrid thermoplastic composites.

The present work integrates ATP overmolding, atmospheric-plasma surface activation, and a semi-empirical model to deliver a process-to-performance pathway for recyclable thermoplastic composites. Chapter 2 quantifies the structural benefit of overmolding CF/PPS tape onto GF-PPS LFT plaques molded by ECM, with pre-registered targets of $\geq 120\%$ gain in tensile strength, $\geq 100\%$ gain in flexural strength, ILSS ≥ 24 MPa, and flatwise tensile bond strength 7.5 ± 0.3 MPa, while maintaining $\sim 33 \pm 2\%$ crystallinity and ≥ 425 °C thermal stability; scalability is assessed via FE projections targeting $\geq 60\%$ additional flexural gain with five tape layers. Chapter 3 establishes a plasma-enabled interface, aiming for $\geq 40\%$ reduction in static water contact angle, AFM roughness $Ra \geq 1.5$ nm (from ~0.2 nm), $\geq 30\%$ increase in surface oxygen by XPS, and laminate improvements of $\geq 7\%$ tensile, $\geq 15\%$ flexural, and $\geq 15\%$ ILSS relative to untreated controls, with a shift from delamination-dominated to cohesive failure. Chapter 4 develops and validates a semi-empirical model that predicts $Ra(t)$ and $\theta(t)$ from plasma power, exposure time/line speed, and material thermal properties, with accuracy targets of $R^2 \geq 0.95$ and RMSE $\leq 5\%$, capturing activation–saturation kinetics with stabilization in 25–30s and generalizing across PPS and LMPAEK via a nondimensional energy-density metric. Together, these chapters constitute a unified study that links processing parameters to interface quality and structural response with quantified, testable criteria.

1.2 Long Fiber Thermoplastics and Extrusion Compression Molding

LFTs are a class of discontinuous fiber-reinforced composites designed to bridge the performance and processing gap between short fiber compounds and continuous fiber-reinforced materials. LFTs typically consist of glass or carbon fibers embedded within thermoplastic matrices such as polypropylene (PP), polyamide (PA), polyphenylene sulfide (PPS), or polyaryletherketone (PAEK). The fiber lengths in LFTs generally range between 3 mm and 25 mm, providing better load transfer than short fiber composites while maintaining moldability [10].

A key processing method for LFTs is extrusion compression molding (ECM)[3]. In this technique, LFT pellets or strands are first melted and extruded through a die, after which the extrudate is cut and transferred into a heated compression mold. The mold is then closed and pressed under temperature and pressure, allowing the material to flow and conform to the mold geometry while preserving relatively long fiber lengths as shown in Figure 1.1.

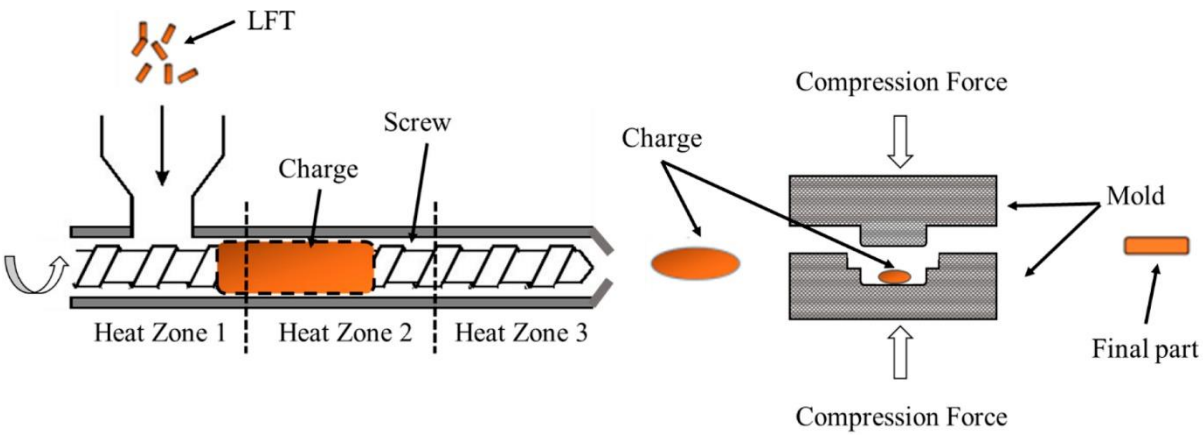


Figure 1.1. Schematic of the extrusion compression molding process for LFT composites. G-LFT are melted and conveyed through a screw extruder to form a charge, which is then transferred into a mold cavity and compressed into the final part shape.

The ECM process offers several benefits, including improved fiber dispersion, better control over part geometry, and reduced fiber breakage compared to injection molding. However, due to complex flow behavior during mold filling, fiber alignment is often non-uniform and

strongly dependent on the charge placement, mold design, and part geometry. As a result, LFT components processed via ECM typically exhibit random or semi-aligned fiber orientations, which can introduce variability in tensile modulus, flexural strength, and impact energy absorption, depending on local orientation distribution [11].

Despite these limitations, ECM remains an efficient method for producing large, lightweight components with moderate structural requirements. It is widely used in automotive and industrial applications where recyclability, impact resistance, and corrosion protection are important [12].

In this research, ECM-processed glass fiber-reinforced LFT substrates are used as the base structure for hybrid composite overmolding. The substrates consist of PPS matrix reinforced with 60 wt% glass fiber, with average fiber lengths of 6–10 mm after molding. The resulting plaques, 3 – 4 mm thick, provide a balance between stiffness and processability, making them suitable for localized reinforcement through robotic deposition techniques such as ATP.

1.3 Automated tape placement in composites manufacturing

ATP has emerged as a transformative manufacturing technology, representing a paradigm shift from traditional manual layup processes to precision-controlled robotic composite manufacturing. The global ATP market, valued at USD 366.1 million in 2023, is projected to reach USD 703.1 million by 2032, exhibiting a compound annual growth rate (CAGR) of 8.5%. This substantial market growth reflects the technology's increasing adoption across aerospace, automotive, and renewable energy sectors, driven by demands for enhanced manufacturing precision and production efficiency [8, 13-15].

The fundamental advantage of ATP lies in its ability to achieve placement accuracies of ±0.25 mm with layup rates ranging from 5-25 m/min, representing a 300-500% improvement over manual processes. These capabilities are particularly critical for thermoplastic composites, where processing temperatures of 300-400°C and pressures of 0.5-2.0 MPa during in-situ

consolidation demand precise thermal and mechanical control. Research conducted by NASA Langley Research Center has demonstrated that ATP processing of PEEK/carbon fiber tapes achieves consolidation temperatures of 400°C with temperature uniformity of ±10°C across the nip point, enabling crystallinity levels of 30-35% necessary for optimal mechanical performance [16-19].

The evolution of ATP technology has addressed specific thermoplastic processing challenges through advanced heating systems. Hot gas torch (HGT) configurations can deliver power densities up to 2.5 kW/cm², while laser-assisted systems provide focused heating with energy densities reaching 5-15 kW/cm². These heating methods enable processing speeds of 50-200 mm/s, substantially higher than the 5-10 mm/s typical for autoclave processes, resulting in cycle time reductions of 75% and energy efficiency improvements of 80% [20, 21].

However, significant technical challenges persist in thermoplastic ATP manufacturing. Process-induced defects, including gaps (0.1-2.0 mm width) and overlaps (0.5-3.0 mm), occur in 15-25% of placed material due to tow lateral movement variations of ±0.5 mm and width variations of ±0.1 mm. These manufacturing variations contribute to interlaminar shear strength reductions of 10-15% and void content increases of 2-4%, directly impacting structural performance. Furthermore, thermal management challenges during processing result in temperature gradients of 50-100°C across tape thickness, leading to non-uniform consolidation and residual stress development [16-19].

To address these ATP limitations, this research will develop an integrated approach combining ATP overmolding with atmospheric plasma surface treatment. The study will systematically investigate the overmolding of continuous carbon fiber-PPS tapes onto glass fiber-PPS LFT substrates using a KAWASAKI ZZX130L 6-axis robot equipped with hot gas torch heating. Processing parameters will be optimized to achieve target mechanical improvements of 120% in tensile strength and 180% in flexural strength while maintaining

crystallinity above 33%. This work will demonstrate that ATP can be effectively utilized for hybrid manufacturing when combined with appropriate surface modification techniques, providing a pathway to overcome traditional consolidation limitations in thermoplastic processing.

1.4 Overmolding with Continuous Reinforcement

Overmolding is a composite manufacturing technique in which one material is molded or deposited over another to form an integrated, bonded structure. In thermoplastic systems, this process exploits the remeltable nature of the matrix, allowing components to be joined without the need for adhesives or fasteners. In hybrid thermoplastic composites, overmolding provides a versatile means of combining dissimilar fiber architecture, typically a discontinuous fiber substrate and continuous fiber reinforcement-to achieve a balance between mechanical performance, design flexibility, and processing efficiency. Overmolding technology enables the integration of localized reinforcement in stress-critical regions while maintaining the economic advantages of discontinuous fiber processing for secondary structural elements [22].

The overmolding process begins with the placement of a pre-formed thermoplastic part, such as a compression-molded LFT plaque, into a mold or a fixture. Continuous fiber-reinforced thermoplastic tape, often unidirectional and pre-impregnated, is then deposited onto the surface of the substrate using a heat-assisted method. The interface bonding occurs through the application of heat and pressure, enabling molecular diffusion and entanglement between the matrix polymers of the tape and substrate. Upon cooling, this interdiffusion results in a unified structure with enhanced local properties [23].

The interfacial bonding mechanisms in overmolding are governed by thermal and rheological parameters that determine the degree of polymer chain entanglement. Differential scanning calorimetry (DSC) analysis reveals that effective bonding requires substrate temperatures

exceeding the matrix glass transition temperature by 50-80°C, with crystallinity matching within ±3% to ensure thermal expansion compatibility. Processing studies indicate that mold temperatures of 280-300°C and injection pressures of 80-120 MPa result in interfacial shear strengths of 25-35 MPa, approaching 80-90% of matrix cohesive strength [24].

Manufacturing process parameters critically influence defect formation and structural integrity. Injection molding simulations using Moldflow analysis demonstrate that gate placement affects fiber orientation distribution, with flow front velocities of 50-200 mm/s producing alignment angles within ±15° of the intended direction. However, processing challenges include weld line formation at flow convergence points, resulting in strength reductions of 20-30%, and residual stress development due to differential shrinkage between continuous and discontinuous fiber regions [25].

Economic analysis reveals that overmolding processes can reduce manufacturing costs by 25-40% compared to fully continuous fiber construction while maintaining 70-85% of the mechanical performance. Cycle times of 2-5 minutes for complex geometries compare favorably with autoclave processing (4-8 hours), enabling production rates suitable for automotive applications requiring 100,000+ parts annually [26].

In this work will pioneer the application of ATP-based overmolding for thermoplastic composites, targeting unprecedented mechanical property improvements through systematic optimization of processing parameters. The research will demonstrate overmolding of CF-PPS tapes onto GF-PPS LFT substrates using ATP processing with target interface strengths exceeding 7.5 MPa measured through flatwise tensile testing. Optical microscopy and SEM analysis will be employed to characterize interfacial bonding quality and failure mechanisms. The study will establish that ATP overmolding can achieve superior performance compared to traditional compression molding approaches while maintaining compatibility with high-

volume manufacturing requirements, with finite element modeling predicting scalability to multi-layer configurations.

1.5 Atmospheric Plasma Surface Treatment of Thermoplastic Composites

Atmospheric plasma surface treatment has emerged as a transformative technology for enhancing interfacial properties in thermoplastic composites without altering bulk material characteristics. Operating at atmospheric pressure (101 kPa) with electron densities of 10^{14}-10^{16} m^{-3} and temperatures of 300-500K, atmospheric plasma systems eliminate the need for vacuum chambers while achieving surface modification depths of 10-100 nm. [27, 28]. Its application in the context of thermoplastic composites has gained increasing attention due to its effectiveness in enhancing surface wettability, promoting interfacial bonding, and improving the performance of multi-material structures [29].

Process parameter optimization studies reveal critical relationships between treatment conditions and surface properties. Power densities of 0.5-2.0 W/cm² with exposure times of 5-60 seconds produce optimal surface activation while avoiding thermal degradation. Treatment speeds of 10-100 mm/s enable integration with manufacturing processes, with surface activation persisting for 24-48 hours under ambient conditions before hydrophobic recovery occurs [30].

Mechanical property enhancements following plasma treatment are substantial and well-documented. Kosmachev et al. reported interlaminar shear strength improvements of 40% for carbon fiber-PPS laminates following 15-minute plasma treatment, with oxygen content increasing from 23% to 33% as measured by XPS. Jung et al. achieved lap shear strengths of 22 MPa for plasma-treated carbon fiber thermoplastic composites compared to 10 MPa for untreated samples, representing a 120% improvement [27].

The science behind plasma treatment lies in the interaction between high-energy plasma species and the polymer surface. When a thermoplastic surface is exposed to an atmospheric

plasma discharge-generated using air, oxygen, or other reactive gases-a complex mixture of ions, radicals, UV photons, and electrons bombards the surface. This bombardment leads to the removal of weak boundary layers, etching of the surface at the nanoscale, and the introduction of polar functional groups such as hydroxyl (–OH), carbonyl (C=O), and carboxyl (–COOH) as shown in Figure 1.1. These chemical groups increase the surface energy of the polymer, improving its ability to form adhesive or cohesive bonds with other materials.

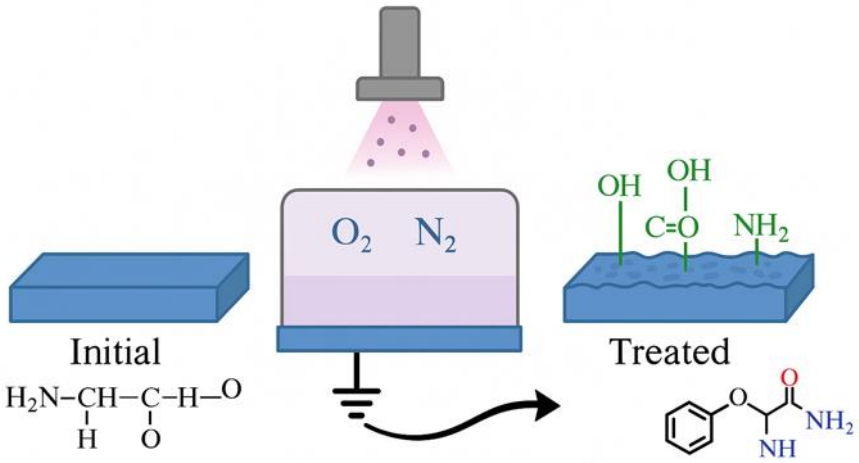


Figure 1.2. Plasma treatment modifies the polymer surface by creating micro and nanoscale textures, and introducing reactive groups, which allows biomolecules to bind directly through physical and covalent interactions without the need for linkers.

For fiber-reinforced thermoplastic composites, particularly those using chemical inert matrices such as PPS, PAEK, or LMPAEK, poor surface energy can limit adhesion during consolidation or bonding with other components. In such systems, atmospheric plasma treatment can be used to increase interfacial adhesion between the thermoplastic tape and substrate by activating the surface prior to bonding. This is especially important in processes

like ATP and overmolding, where bonding occurs under thermal and mechanical consolidation without chemical adhesives.

The plasma-induced surface roughness also contributes to mechanical interlocking at the interface, which becomes especially relevant in composite systems with mismatched stiffness or thermal expansion properties. Furthermore, since the treatment depth is limited to a few nanometers, the bulk mechanical and thermal properties of the material remain unchanged, preserving the integrity of high-performance composite laminates.

This research will conduct the first systematic investigation of atmospheric plasma treatment specifically optimized for LMPAEK/carbon fiber tapes in ATP processing applications. The study will achieve quantifiable surface modifications targeting contact angle reductions from 90° to below 25° (>70% decrease) and surface roughness increases from 0.2 nm to above 1.5 nm. XPS analysis will confirm oxygen content increases exceeding 30%, while FTIR will validate the formation of hydroxyl and carboxyl functional groups. The plasma-treated composites will demonstrate target improvements of 15% in interlaminar shear strength, 18% in flexural strength, and 7% in tensile strength. Critically, this work will establish optimal treatment parameters (processing speeds of 76 mm/s, standoff distances of 12.7 mm) that integrate seamlessly with ATP manufacturing, providing a scalable solution for industrial implementation.

1.6 Surface Modeling of Plasma-Treated Interfaces

While experimental surface treatments provide valuable insights into interface behavior, The development of predictive models for plasma-induced surface evolution represents a critical advancement in understanding and controlling interfacial behavior in thermoplastic composites. Current modeling approaches integrate plasma physics, surface chemistry, and material science to establish quantitative relationships between treatment parameters and resulting surface properties.

Empirical modeling studies have achieved significant predictive accuracy for surface roughness evolution. Semi-empirical models incorporating logarithmic growth functions with activation and saturation terms demonstrate correlation coefficients (R^2) exceeding 0.95 when validated against AFM measurements. These models successfully predict roughness evolution according to established kinetic relationships accounting for plasma energy input, material thermal properties, and surface softening effects[31].

Surface roughness modification during plasma treatment follows complex kinetics driven by ion bombardment, radical etching, and thermal effects. Semi-empirical models incorporating logarithmic growth functions with activation and saturation terms have demonstrated correlation coefficients (R^2) exceeding 0.95 when validated against AFM measurements. These models successfully predict roughness evolution according to established kinetic relationships that account for plasma energy input, material thermal properties, and surface softening effects near the glass transition temperature.

In the case of thermoplastic composites like LMPAEK, surface roughness evolution can be described using logarithmic or empirical relationships, taking into account plasma energy input, thermal diffusivity of the polymer, and surface softening effects near the glass transition temperature. An improved generalized roughness model can be expressed as:

$$Ra(t) = Ra_0 + A\log(1 + Bt) + C \times \frac{\gamma_s(t)}{K_{th} \cdot f(T_g, T_{pl})} \qquad \text{(Eq 1.2)}$$

where Ra_0 represents initial surface roughness, parameters A and B govern logarithmic growth amplitude and characteristic time scaling respectively, C scales the coupling between surface energy and roughness evolution, K_{th} is thermal conductivity,

and $f(T_g, T_{pl})$ represents temperature-dependent chain mobility effects. This formulation captures the transition from rapid initial activation to saturation behavior observed experimentally [31].

Contact angle evolution incorporates dual-mechanism approaches accounting for both rapid surface activation and long-term stabilization effects. The Wenzel equation modified for plasma-treated surfaces accurately predicts wettability evolution with mean absolute errors (MAE) below 3°, enabling precise control of surface energy modifications. Surface energy modeling utilizes the Owens-Wendt approach to quantify polar and dispersive components following plasma treatment, with experimental validation demonstrating surface energy increases from 35-40 mJ/m² to 65-75 mJ/m² for high-performance thermoplastics [32]. Machine learning approaches have recently emerged for contact angle prediction, with XGBoost algorithms achieving R^2 values of 0.86 when validated against experimental datasets. These models incorporate multiple surface parameters including roughness, chemical composition, and material properties to predict wettability more accurately than single-parameter correlations [33].

The stability of plasma-induced modifications represents a critical modeling challenge. Post-treatment recovery studies demonstrate that surface modifications exhibit remarkable stability for cellulose-based and synthetic polymers, with hydrophilic character maintained for extended periods. However, some thermoplastics show gradual hydrophobic recovery due to molecular rearrangement, requiring time-dependent modeling approaches [34].

In this work we established the first validated semi-empirical model specifically designed for LMPAEK/carbon fiber composites under atmospheric plasma treatment conditions. The model will achieve target accuracy metrics of $R^2 > 0.95$ and errors below 5% compared to experimental AFM and contact angle measurements. The mathematical framework will incorporate material-specific parameters including thermal conductivity (0.2-0.4 W/m·K), glass transition temperature (145-155°C), and plasma energy density to predict surface roughness and wettability evolution. The model will successfully capture the nonlinear transition between surface activation and saturation phases, providing optimal treatment

windows of 25-30 seconds for maximum enhancement. This predictive capability will enable real-time process optimization and quality control in manufacturing environments, representing a significant advance in plasma surface engineering for advanced composites. The model will be validated through comprehensive experimental campaigns using AFM, and contact angle goniometry, establishing a robust framework for industrial implementation.

1.7 Research Objectives and Organization

The cumulation of current literature reveals substantial knowledge gaps at the intersection of ATP, plasma surface treatment, and hybrid thermoplastic composite manufacturing. While individual technologies have demonstrated promising capabilities, the integration of these approaches to achieve superior structural performance remains underexplored, representing a critical opportunity for advancing next-generation composite manufacturing. This dissertation aims to develop and understand hybrid thermoplastic composite structures by combining LFTs, continuous fiber reinforcements, and surface engineering techniques. The central hypothesis is that combining ATP with atmospheric plasma surface treatment can significantly improve the interfacial bonding and mechanical performance of overmolded thermoplastic composites.

To address this hypothesis, the work is organized around three interrelated research objectives:

Objective 1: *Hybrid Overmolding of Continuous CF Tape onto LFT Substrates via ATP* - Quantify the tensile strength, flexural strength, and interlaminar shear strength of hybrid thermoplastic composites manufactured through ATP overmolding of continuous CF tapes onto LFT substrates, establishing baseline performance metrics and identifying interfacial debonding versus cohesive matrix failure modes that limit load transfer efficiency.

Objective 2: *Atmospheric Plasma Surface Treatment of LMPAEK/CF Tape* - Develop and validate atmospheric plasma surface treatment protocols optimized for

LMPAEK/CF composite tapes, achieving quantifiable improvements in interfacial bonding strength through surface oxidation and hydroxyl group formation while maintaining compatibility with ATP processing conditions and production rates.

Objective 3: *Predictive Numerical Modeling of Plasma-Induced Surface Roughness and Wettability Evolution in LM-PAEK/CF Tape*- Establish predictive semi-empirical models based on logarithmic growth kinetics for plasma-induced surface roughness (Ra) and contact angle evolution that accurately describe surface topography and wettability changes as functions of treatment parameters, enabling process optimization and quality control in manufacturing environments.

Research Significance and Innovation:

This research addresses a critical gap in composite manufacturing by integrating three advanced technologies – ATP, atmospheric plasma treatment, and hybrid overmolding – to achieve performance levels unattainable through individual approaches. The investigation provides fundamental understanding of interfacial phenomena governing load transfer efficiency in hybrid structures while establishing manufacturing protocols suitable for industrial implementation.

The economic impact is substantial, with potential cost reductions of 30-50% compared to traditional autoclave processing while achieving performance levels approaching fully continuous fiber systems. Processing cycle times of 2-5 minutes versus 4-8 hours for conventional methods enable production scales suitable for automotive and aerospace applications requiring 50,000-500,000 parts annually.

Contributions to Knowledge from This Research.**:**

This work will provide the first quantitative understanding of plasma-induced surface modifications specifically optimized for thermoplastic matrices in ATP applications, filling a critical knowledge gap in surface engineering for advanced composites. The research will

develop predictive models that enable process optimization and quality control capabilities previously unavailable, advancing the field toward intelligent manufacturing systems. The integration of ATP processing with real-time surface treatment represents a paradigm shift from post-processing surface modification to in-situ enhancement during manufacturing, potentially transforming composite production methodologies across multiple industries.

Research Organization:

Chapter 2 investigated ATP overmolding of continuous carbon fiber-PPS tapes onto glass fiber-PPS substrates, establishing mechanical performance baselines with targets of 129% tensile strength improvement and 192% flexural strength enhancement, while identifying interfacial bonding mechanisms through comprehensive materials characterization and finite element modeling.

Chapter 3 explored atmospheric plasma treatment optimization for LMPAEK/carbon fiber tapes, quantifying surface modifications that targeted a 73% contact angle reduction and demonstrated mechanical property enhancements of 18.7% in interlaminar shear strength through advanced characterization techniques that correlated treatment parameters with performance improvements.

Chapter 4 developed and validated semi-empirical models for predicting plasma-induced surface evolution, creating mathematical frameworks that achieved $R^2 > 0.95$ accuracy, indicating that the model reliably explained over 95% of data variability, for process control and optimization in industrial manufacturing environments, enabling real-time parameter adjustment and quality assurance.

Research Impact and Contributions:

Hybrid thermoplastic composites are transforming aerospace manufacturing by enabling up to 50% weight reduction, significantly lowering fuel consumption and emissions. Boeing's 777X uses these materials in flight control surfaces to enhance damage tolerance and

repairability, while Airbus employs ATP to rapidly produce lightweight A350 fuselage sections with greater design flexibility. NASA's Orion spacecraft relies on thermoplastic composites for thermal protection systems that withstand extreme re-entry heat. Deep space missions use these composites in rocket nozzles for tailored thermal performance, and the Mars rover incorporates radiation-resistant, lightweight composite panels. Wind turbines and high-speed trains utilize plasma surface modifications and ATP to extend lifespan and improve efficiency.



Figure 1.3. Industrial aerospace composite programs showcasing structural components that benefit from advanced thermoplastic manufacturing technologies.

As shown in Figure 1.3 the Clean Sky and CORAC aerospace research programs demonstrate the industrial need for advanced manufacturing technologies in next-generation aircraft structures. These programs showcase critical components including thermoplastic composite floor grids, wing panels, cockpit frames, and fuselage sections that require enhanced interfacial bonding and manufacturing efficiency. Large-scale structural elements, ranging from 4.2 m wing panels to integrated fuselage sections with lightning strike protection, represent ideal applications for hybrid thermoplastic composite manufacturing approaches. The integration of ATP with plasma surface modification addresses manufacturing challenges in complex geometries such as stringers, frames, and overmolded junction areas where traditional bonding methods may be insufficient. This work aims to advance manufacturing methods and surface engineering to unlock the full potential of hybrid thermoplastic composites across these industries, developing predictive models and validated processing protocols that will accelerate adoption and enable safer, lighter, and more sustainable systems for next-generation high-performance technologies.

2. CHAPTER 2

Hybrid Overmolding of Continuous CF Tape onto LFT Substrates via ATP

Abstract

LFT composites have gained significant attention in various industries due to their desirable properties, including ease of processing, recyclability, superior strength, and corrosion resistance. Glass fiber (GF) is commonly used as a reinforcing material in LFT composites, given its low cost and excellent mechanical properties. However, there are challenges associated with the existing manufacturing processes, such as fiber attrition and limitations in achieving anisotropic properties. In this study, the overmolding of glass fiber-reinforced polyphenylene sulfide long fiber thermoplastic (G-LFT) and unidirectional continuous carbon fiber/polyphenylene sulfide tape (CF-Tape) using an ATP robotic system has been investigated. The aim is to explore the potential of ATP for improving the mechanical properties of LFT composites. The results reveal that the overmolding process using CF-Tape on G-LFT leads to significant enhancements in mechanical performance. A 129% increase in tensile strength and a 192% improvement in flexural strength were observed compared to the G-LFT baseline. The bond strength at the interface was evaluated through flatwise tensile testing, which resulted in partial failure within the CF-Tape and a measured bond strength of 7.52 MPa ±0.34. Thermogravimetric analysis (TGA) and differential scanning calorimeter (DSC) were conducted to analyze the thermal behavior of the parts. The crystallinity was measured using DSC data, and a value of 33.4% was obtained. Low-velocity impact testing has been conducted to understand the dynamic behavior of G-LFT and G-LFT/CF-Tape. The impact energy absorbed was found to be similar in both cases. A numerical model was used to reduce the number of experiments. It was found that the flexural strength improved by 60% by adding five layers of CF-Tape. In summary, this research contributes to expanding the knowledge of overmolding techniques and highlights the potential of ATP-based overmolding for enhancing the localized strength and easily applied to intricate geometries.

Keywords: Overmolding, Long fiber thermoplastic, Finite Element Analysis, Micromechanics Analysis, Automated tape placement.

2.1 Introduction

LFT composites are a popular choice in the automotive and transportation sector due to their ease of processing, recyclability, superior specific modulus and strength, excellent impact, corrosion resistance, and long shelf life[35]. Various thermoplastic polymers ranging from commodity (e.g.: polypropylene (PP), high-density polyethylene (HDPE), etc.) to high-performance engineering (e.g.: polyamide (PA), polyphenylene sulfide (PPS), polyether ether ketone (PEEK) etc.) have been used as matrices in LFTs [6, 36]. As a result, LFTs have become one of the most advanced lightweight engineering materials, and their demand is continuously increasing in various sectors such as automotive, aerospace, electrical, etc. [37]. Glass fiber (GF) is frequently employed as reinforcing material in LFTs because of low-cost and superior mechanical properties[38]. LFT composite parts are manufactured via injection molding (IM) or extrusion compression molding (ECM). The IM process provides higher mechanical properties in the direction of the flow[39]; However, it results in higher fiber attrition due to the shear stresses induced in the compounding screw. ECM composites provide pseudo-isotropic properties in the finished part with more fiber length retention as compared to IM [40]. However, both IM and ECM parts are limited by the aspect ratio of the discontinuous fiber [41-43].

One approach to enhance the mechanical performance of discontinuous fiber i.e. LFTs is overmolding [22, 44, 45]. The purpose of composite overmolding is to integrate advantages and reduce shortcomings of a 100% discontinuous composite, like LFT. Alwekar et. al.[40] studied the overmolding of glass/polypropylene LFT and unidirectional continuous glass-polypropylene tape. The overmolded panel was manufactured by compression molding. The authors reported 119-142% and 60-70% increase in flexure strength and modulus,

respectively. However, they observed an out-of-plane warpage in the finished consolidated panel. Heer et al [46], studied the mechanical properties of overmolded GF/polyamide 6 (PA6) long fiber thermoplastic-direct (LFT-D) and glass mat thermoplastic (GMT). The authors compared the properties of the overmolded sample with constituents such as LFT-D and GMT and observed that the properties ranked as follows- GMT > overmolded > LFT-D. Therefore, based on the particular application, the properties of the overmolded part could be tailored according to the placement of the constituent. However, the process consists of some drawbacks such as out-of-plane warpage that could occur in the finished part. Gan et al. [47] studied the absorption properties of grid-stiffened thermoplastic composites under transverse loading. Commingled unidirectional Twintex® E-glass-PP and commingled woven Twintex® E-glass-PP were used to construct the ribs and skin, respectively. The commingled fibers were arranged in grooves to create the ribs, with the skin made up of commingled woven fabric and integrally bonded to the ribs. This approach provided uniform fiber distribution and fibers oriented in the direction of the ribs. However, despite its numerous benefits, this technique is highly time-consuming and not cost-effective. Lee et al [48] developed a rib-stiffened composite side impact beam (SIB) by co-molding LFT ribs with woven glass fabric prepregs. The authors conducted tension and compression tests. The results showed that the specific strength of the composite SIB was 130% and 10% higher than steel SIB in tension and compression, respectively. It was reported that hybrid composites could be a good replacement as compared to steel for SIB.

This study consists of fabricating and analyzing the overmolded LFT panel, the overmolding conducted with ATP. In recent years, ATP has become a main stream composite manufacturing technique with significant increase in demand from 6% in 1990 to 35% by 2020 [49]. ATP in-situ thermoplastic composites has witnessed an interest from various industries such aerospace, oil and gas, due to elimination of secondary post-curing process

such as autoclave molding, resulting in cost and energy effectiveness [21, 50-52]. More details about ATP can be found in [53-61].

In this work, glass fiber reinforced polyphenylene sulfide G-LFT and unidirectional continuous carbon fiber/polyphenylene sulfide tape (CF-Tape) was used. PPS is an engineering thermoplastic polymer known for its high temperature resistance, featuring a molecular structure composed of alternating aromatic rings and sulfur atoms as shown Figure 2.1.

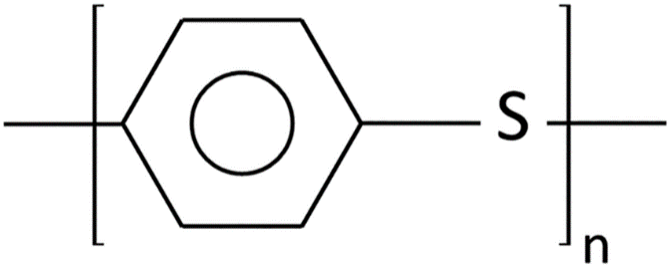


Figure 2.1 Chemical structure of Polyphenolic sulfide (PPS).

PPS boasts a noteworthy array of properties, including thermal stability, chemical resistance, flame resistance, wear resistance, processability, low coefficient of thermal expansion, and impressive mechanical characteristics. The semi-crystalline nature of PPS provides benefits such as the capability to be utilized above the glass transition temperature without compromising modulus and resistance to creep deformation [62]. Therefore, PPS finds application in the automotive industry, particularly in situations requiring elevated temperatures [63, 64].

To the best of the authors' knowledge, no research has been conducted on the overmolding of CF-Tape and G-LFT processed with the ATP robotic system. Previous studies have explored hybrid overmolding using injection or compression molding, mostly involving pre-consolidated laminates or short-fiber substrates. However, the overmolding of in-situ consolidated continuous CF-Tape tapes onto long glass fiber-reinforced thermoplastics using ATP has not been reported. The interface bonding behavior, thermal compatibility, and

mechanical performance under ATP processing conditions remain largely unaddressed. In this study, an overmolded panel of G-LFT and CF-Tape was manufactured. A morphological study was conducted to examine the bonding at the LFT-Tape interface. The interface mechanism was further evaluated mechanically using a flat-wise tensile test. A number of mechanical tests such as tensile (ASTM D3039), flexural (ASTM D790), and short beam shear (ASTM D2344) were performed in order to understand the effect of overmolding. Low velocity impact (ASTM D7136) testing was also carried out to analyze the effect of energy absorption after CF-Tape overmolding. A numerical analysis was implied to minimize experimental iterations by evaluating the effect of CF-tape layer quantity and orientation on localized strength, using a validated model of the three-point bending test.

2.2 Materials and Methods

2.2.1 Materials

A 12.7 mm (½-inch) 60% weight (wt.) GF reinforced PPS LFT pellets (PPS-GF60, LFT Celstran®) were procured from Celanese (Ticona/Celanese, Winona, MN, USA). A 12.7 mm (½- inch) wide unidirectional CF-tape (AS4/PPS) tape, 66% wt. CF and with an approximate thickness of 0.16 mm was provided by Cytec Engineered materials, now, Solvay S.A Inc. (Alpharetta, GA, USA). ATP KAWASAKI ZZX130L 6-axis robot, located at the IACMI-Composites Institute, Knoxville was used for the fabrication of the overmolding panel using the hot gas torch head (HGT) developed by Automated Dynamics in 2013, now, Trelleborg Group, Sweden.

2.2.2 Processing

The process to obtain an overmolded panel was divided into two steps. (a) The first step was the manufacturing of the substrate LFT plate(s). G-LFT pellets and CF-Tape were dried at 80 °C for 8 hours before any processing. Dried G-LFT pellets were used in the ECM process to manufacture the panels. ECM process involved two operations extrusion and compression

molding. In the first operation, the pellets were fed into a single screw extruder (B-30 IMPCO Plasticator) at a rate of 0.454g/min (1lb/min). The extruder consists of four heating zones to melt the polymer which were kept at 295 °C, 300 °C, 305 °C, and the nozzle temperature at 310 °C. The hot, molten charge 38 cm x 7.6 cm approximately (15" x 3") obtained from the plasticator was transferred to the fast-acting Wabash (Model DA150-36-BCX) hydraulic compression press. A 280 mm × 280 mm x 3.2 mm (11" x 11" x 0.125") consolidated panel was fabricated under 2.89 MPa (420 psi) pressure with 60-second dwell time as shown Figure 2.2.

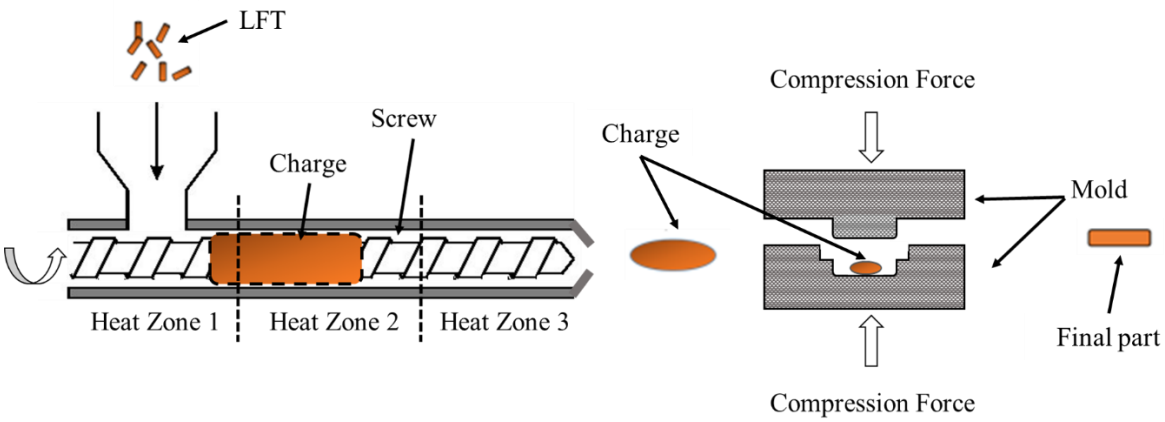


Figure 2.2 Schematic of the extrusion compression molding process for LFT composites. G-LFT are melted and conveyed through a screw extruder to form a charge, which is then transferred into a mold cavity and compressed into the final part shape.

(b) The second step involved the manufacturing of an overmolding panel using the ATP process. The G-LFT panel was mounted on an aluminum flat mandrel as shown in Figure *2.3*(a). An ATP system includes a coordinated spindle, a stainless-steel compaction roller (placement head), a tape dispensing system, and hot gas torch (HGT) as a heat source. The tape was fed into the roller and heated using HGT. The temperature for HGT was kept at 840 °C (temperature of the torch and not at the contact place with the mandrel). The nip temperature was noted to be approximately 290°C at the contact point between the tape and G-LFT panel substrate. The temperature was monitored using a Teledyne FLIR A700-EST IR

camera. The tape was laid down on the substrate as shown in Figure *2.3* (b) and bonded with the combination of heat and pressure 63.5 Kg (140 lb) applied through a compaction roller of 12.7 mm (½- inch) diameter.

No visible warpage or residual deformation was observed in the overmolded parts after ATP processing. The parts remained flat after cooling and maintained dimensional stability. Visual inspection confirmed that the flatness of the specimens was within the tolerances specified in ASTM D790 and ASTM D3039, ensuring their suitability for subsequent mechanical testing. During the overmolding process, the asperities of the substrate and the tape were flattened during consolidation due to the pressure applied by the compaction roller and the temperature generated by the HGT, leading to “intimate contact”. Once this phenomenon occurs, the presence of interlaminar voids diminishes, facilitating molecular chain interdiffusion between G-LFT and CF-Tape, thereby establishing a robust bond at the interface [65, 66].

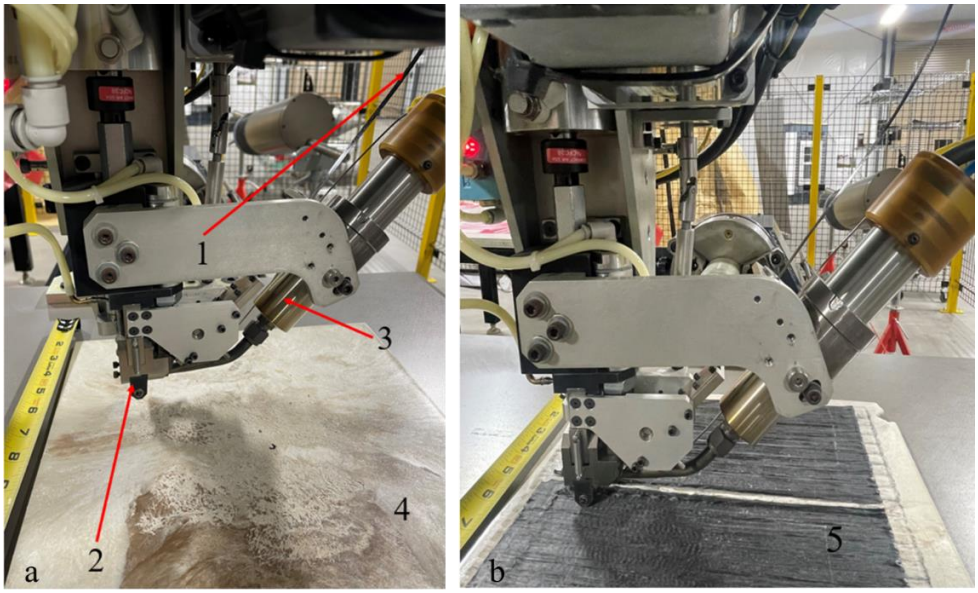


Figure 2.3. Illustration of the ATP robot: 1) CF-Tape 12.7mm (½- inch), 2) The compaction roller, 3) The HGT, 4) The G-LFT substrate 5) The overmolded part. (a) The G-LFT substrate before overmolding. (b) The CF-Tape will pass through a guide slot, the tape will be heated with the HGT, and in-situ consolidated on the substrate with a load of 64.5 Kg (140 lb). applied by the compaction roller.

2.2.3 Testing and Analysis

2.2.3.1 Three-point bending or flexural test

Flexural specimens were cut from the overmolded plaques using an OMAX Waterjet 2026 system to ensure precision and prevent edge defects or thermal damage. Samples were extracted along the longitudinal direction of the CF-Tape to align with the fiber orientation. Testing was performed using a universal testing machine (Test Resources, Model 313 series, Minneapolis, MN) equipped with a 50 kN load cell, in accordance with ASTM D790. The three-point bending configuration was arranged such the CF-Tape side was under tensile loading, as CF performed better in tensile than compression [67, 68] while G-LFT section was under compression loading as shown in Figure *2.4* Five specimens from each plaque (i.e., LFT and overmolded) were tested at 1.59 mm/min loading rate and average flexural properties were reported.

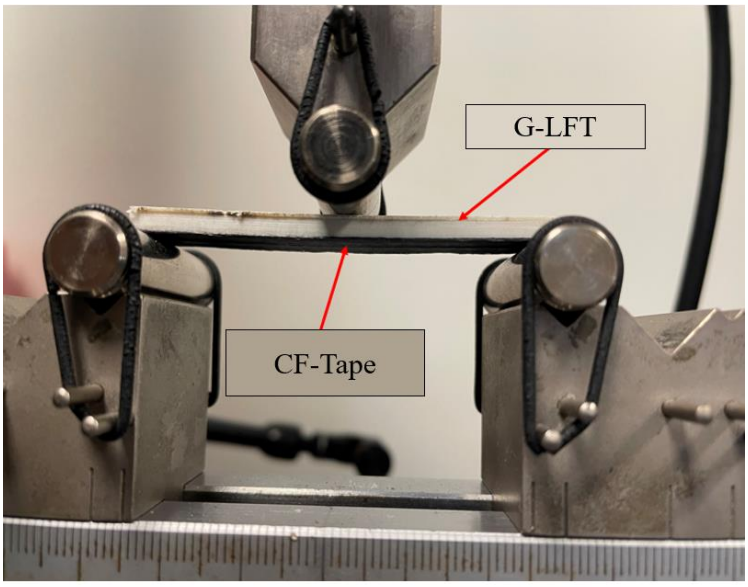


Figure 2.4. Flexural setup for the overmolded specimen, the tape was from the bottom side, as CF performed in Tensile better than compression.

The fractured surface of the flexural test specimen and the morphology of the delamination between CF-Tape and G-LFT was examined using a Zeiss EVO 25 scanning electron microscopy (SEM).

2.2.3.2 Thermal analysis

Thermogravimetric analysis (TGA) was conducted under a nitrogen atmosphere to prevent oxidative effects and to accurately evaluate the thermal stability and degradation behavior, of both G-LFT and G-LFT/CF-Tape composites. TGA Q50 was used at a heating rate of 15°C/min starting from room temperature to 800°C. Differential scanning calorimetry (DSC) utilized to portray the melting behavior of the G-LFT substrate and the overmolded samples. DSC sample was sectioned through the thickness to include the interface region, comprising both the CF-Tape and a portion of the underlying G-LFT substrate. DSC was performed using DSC Q2000 setup by applying heating and cooling. Samples were dried 24 hours at 80°C prior testing, then heated from room temperature to 400°C and cooled down to 20° in presence of liquid nitrogen (50.0L/min) with a rate of 20°C/min.

2.2.3.3 Flatwise (through-thickness) tensile strength

A flatwise tensile test was performed to understand the bonding characteristic of the overmolded tape on the G-LFT panel. According to ASTM D7291 standard, through-thickness testing specimens were prepared with an average diameter of 25.4 mm and 4 mm thickness. Two aluminum cylinders were attached to the specimen using J-B WeldTM epoxy. A square mesh pattern was created on the aluminum surface Figure *2.5* to increase the surface area for proper bonding. Prior to the testing, the specimen was kept under pressure (50 psi) for 24 hours for the complete curing of epoxy. Test resources frame (50 kN load cell) was used to pull the samples at 0.1mm/min loading rate.

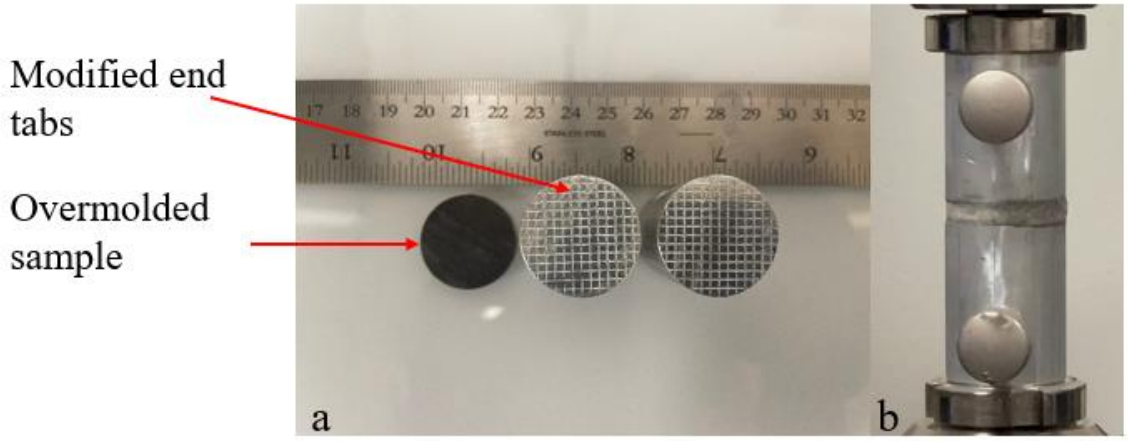


Figure 2.5 (a) Sample preparation of the overmolded part and surface modification of the aluminum end tabs. Aluminum tabs were modified to achieve failure on the interface and not in the glue part. (b) Glue placed on the end tabs and specimens were mounted for out of plane tension test.

2.2.3.4 Tensile (In-plane) test

A set of five (5) specimens was prepared for tensile testing according to ASTM D3039. The average width and thickness of the overmolded sample was 254 mm x 25.4 mm (Length x Width). All specimens were tapped using GEEX 1871224N glass epoxy (Accurate PLASTICS) and superglue (Gorilla). The test was performed on the 50 kN load cell test resource frame and samples were pulled at 2 mm/ min loading rate. Strain was monitored using an axial extensometer, Model 3542 Technology Corp, Jackson WY 83001 USA.

2.2.3.5 Drop-tower (low velocity) impact test

The low velocity impact (LVI) tests were conducted using the Instron CEAST 9340 drop tower. A set of 5 specimens with 101.6mm x 152.4mm (4x6 in) dimensions were prepared according to ASTM D7136. In this test, a hemispherical tup of 16 mm (0.63in) diameter and 3.22 kg (7lbs) weight was used. A tup was dropped on a specimen from 1080 mm (42.5in) height with 4.6 m/s velocity, generating 34 J kinetic energy.

2.3 Materials and Methods

2.3.1 Interface Bonding

Figure *2.6* (a) shows the optical microscopy (OM) image of the overmolded sample. OM image analysis was conducted to evaluate the weld line behavior and the effect of ATP overmolding on the G-LFT surface. Figure *2.6*b reveals no porosity or defects in the substrate G-LFT surface or at the interface. However, matrix deformation has been noticed at the interface, attributed to the heat applied by the HGT during the ATP overmolding. This deformation suggests localized melting, which promotes molecular interdiffusion between the G-LFT and CF-Tape, enhancing interfacial bonding. To further understand the bond characteristics, interlaminar shear strength (ILSS) testing was conducted in accordance with ASTM D2344. The ILSS specimens were tested at a constant rate of 1 mm/min. *Figure 2.6 (b)* shows the OM image of the failed sample. A strong bond at the interface was indicated by the limited delamination between the two surfaces and the presence of G-LFT matrix residue on the CF-Tape surface, suggesting cohesive failure. Additionally, embedded resin and fiber imprints were observed, pointing to the development of mechanical interlocking. The ILSS increased from 18 MPa for the G-LFT to 24 MPa after ATP overmolding, representing a 33% improvement, supporting the effectiveness of the bond formed at the interface.

2.3.2 Thermal Analysis

Figure 2.7 shows the DSC and TGA results of G-LFT and G-LFT/CF-Tape, respectively. The twenty (20) samples were dried at 80°C for 8 hours in the oven to avoid moisture effect. The heat-cool cycle was applied for the DSC. It can be noticed from the heating cycle that G-LFT and G-LFT/CF-Tape had a similar glass transition T_g and melting point in the range of 125 - 130°C and 280-285°C respectively. Melting point determines the lower limit for processing temperature. It could be observed from the cooling cycle that the recrystallization of the G-LFT and the overmolded sample started at 245°C. The degree of crystallinity χ_c of G-LFT

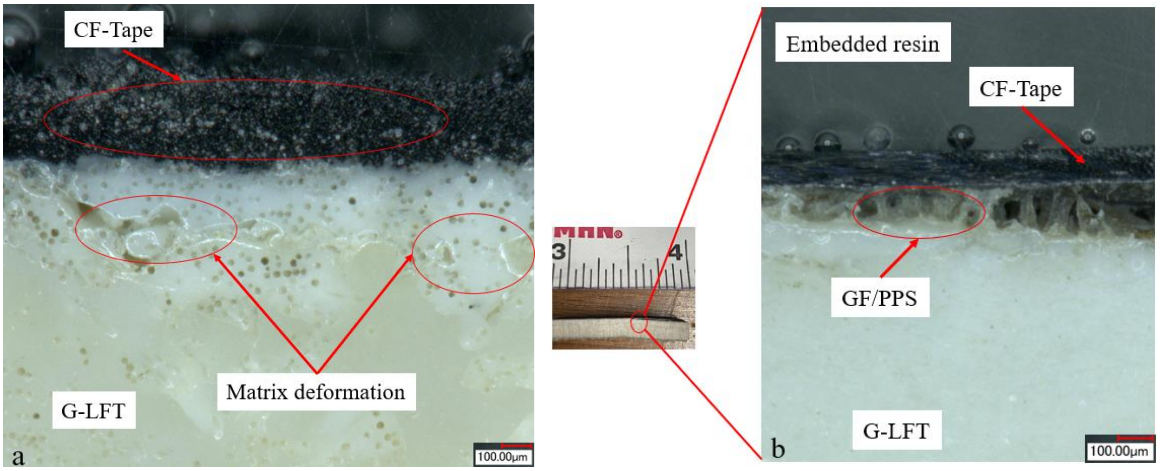


Figure 2.6. (a) OM image showing the bonding adhesion on the interface after the overmolding process between the G-LFT and the CF-Tape. (b) A slight delamination has been noticed on the interface of an ILSS tested sample, the GF/PPS attached on the failed tape evidence the strong bonding on the interface.

and G-LFT/CF-Tape was calculated using eq 2.1:

$$\chi_c = \frac{\Delta H_m - \Delta H_c}{\Delta H_{lit}\, x\, W_p} x\ 100$$

where, $\Delta H_m (20.21\ J/g)$ and $\Delta H_c (15.1\ J/g)$ are the enthalpy at melting and cooling (crystallization), respectively, extracted based on the DSC data plot Figure *2.7* (a). ΔH_{lit} is adapted from the literature, in case of PPS is 76.4 J/g [69]. ΔH_{lit} is adapted from the literature, in case of PPS is 76.4 J/g [69]. W_p is the weight fraction of PPS in the composite sample which is 40% in the G-LFT based and 37% in the overmolded part based on TGA plot shown in Figure *2.7* (a). It was found that χ_c of G-LFT was 33.4% ± 0.6% and around 33.5% ± 0.7% for G-LFT/CF-Tape. The small difference in crystallinity is within the measurement variability and is not considered statistically significant. Knowing that the crystallinity of the materials is directly affected by the cooling rate of the manufacturing process. Noting that during ATP overmolding the CF-Tape was exposed to a cooling rate of 1000K.min^{-1}. Since the surface of the G-LFT part is exposed to the heat of the HGT during the overmolding process, maintaining the same degree of crystallinity was critical to achieve a good bonding

on the interface [70, 71]. This result can be attributed to the combined effects of localized heating and geometry. The thin tape thickness (0.15–0.16 mm) may have led to a rapid initial surface cooling, while the internal region of the tape, in contact with the heated G-LFT substrate, cooled more slowly. Additionally, temperature gradients across the tape thickness and the measurement location could have masked local variations in crystallization. Similar observations have been reported in the literature for PPS composites processed with rapid cooling but subject to non-uniform thermal conditions [72].

TGA was conducted to evaluate the degradation behavior of G-LFT and G-LFT/CF-Tape. It can be observed from Figure *2.7* (b) that less than 1% weight loss was reported up to 425°C in both samples, indicating PPS stability and the upper processing temperature limit. Figure 2.6b shows the degradation behavior of G-LFT and overmolded samples in air. The complete degradation of G-LFT and G-LFT/CF-Tape was observed at 650°C and 575°C respectively. At 650°C, G-LFT maintained 62% residue which was very close to the initial content of glass fiber (60%). G-LFT/CF-Tape sample showed a total of 66% residue. G-LFT pellets contain 60% glass while CF-Tape contain 66% of CF. Therefore, the average fiber content is close to 63-64%. However, the higher residue may be due to the overmolding process as the effect of pressure and heat of the compaction roller applied by the ATP on the G-LFT substrate would peel off a small amount of the polymer.

2.3.3 Flexural testing and morphology

A three-point bending test was conducted to assess the performance of continuous CF-tape on the G-LFT plaque. Figure *2.8* (a) presents the properties derived from the flexure test results. Figure 6a displays the flexural strength and modulus, while Figure *2.8* (b) illustrates the load vs displacement curve. Notably, a single layer of 0.15mm unidirectional CF-tape was overmolded onto the G-LFT surface.

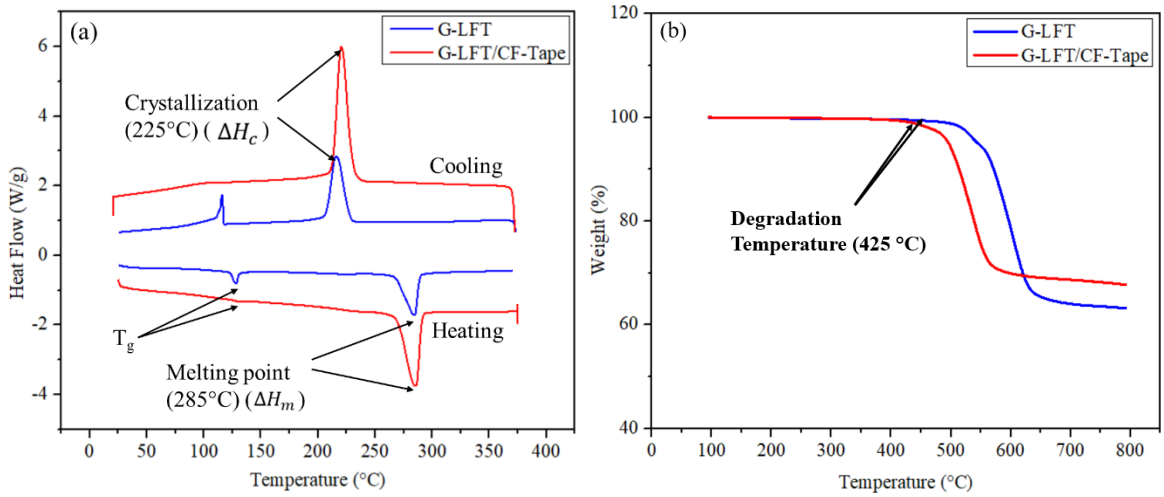


Figure 2.7 (a) DSC of G-LFT and G-LFT/CF-Tape, showing the melting point (285°C) and the crystallization point (225°C), (b) TGA analysis of G-LFT and G-LFT/CF-Tape showing that the degradation temperature of the composites started at 425°C.

The flexural strength and modulus of the overmolded G-LFT increased from 99 MPa to 290 MPa (a 192% increase) and from 5.09 GPa to 11.04 GPa (a 120% increase), respectively. These results demonstrate that the addition of CF-Tape to the G-LFT plaque enhances its bending resistance. Additionally, both samples exhibited a brittle type of failure, as observed in Figure *2.8* (b). The reduced deformability observed in the composite is primarily attributed to the high glass fiber content (>60 wt%), which significantly increases stiffness and introduces stress concentrations at the fiber–matrix interface. While the semi-crystalline nature of PPS contributes to the overall rigidity of the matrix, its effect is secondary compared to the dominant influence of the reinforcing fibers on limiting the material's ability to deform under load. This leads to brittle failure, as the material fractures rather than plastically deforming [73].

The G-LFT exhibited a single-step brittle failure, while the G-LFT/CF-Tape failed in two stages. To comprehend the two-step failure mechanism, SEM analysis was conducted on the failed specimen, as depicted in Figure *2.9* In the first stage, a crack was initiated in the G-LFT section and propagated towards the interface, resulting in delamination. The initiation of

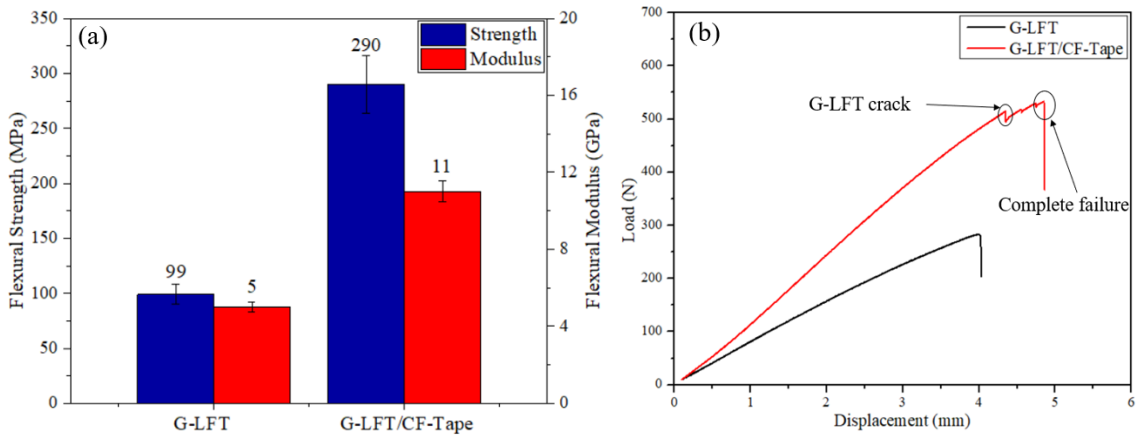


Figure 2.8 (a) The average flexural properties of the manufactured composites with and without tape. An increment of 192% in flexural strength and 120% in modulus has been noticed along the fiber direction of the tape. (b) Load versus displacement for the three-point bending testing illustrating a brittle failure in the G-LFT and the overmolded samples.

the crack in the G-LFT region indicates good bonding between the two surfaces. As shown in Figure *2.9* fiber breakage was observed within the G-LFT layer and slight delamination occurred at the CF-Tape interface. The fiber fracture ahead of the delamination zone suggests that the interfacial strength was sufficient to transfer the load before local failure occurred. These features point to a mixed failure mode involving both cohesive fracture in the G-LFT and interfacial separation. It is noteworthy that both samples were consolidated without any surface treatment. Literature suggests that the interfacial bonding can be improved by mechanical (grid blasting) [74], non-mechanical (plasma) [75] or chemical [65, 76] treatments. Surface treatment analysis was out-of-scope for this work and will be evaluated elsewhere.

2.3.4 (Through-Thickness) Tensile Strength

Through-the-thickness (flatwise) tests were conducted to determine the out-of-plane tensile strength of the overmolded part. A total of five specimens were tested, and the load-displacement curves are depicted in Figure *2.10*. While all samples exhibited similar brittle failure, there was significant variation noted in the peak load. Table 1 provides the

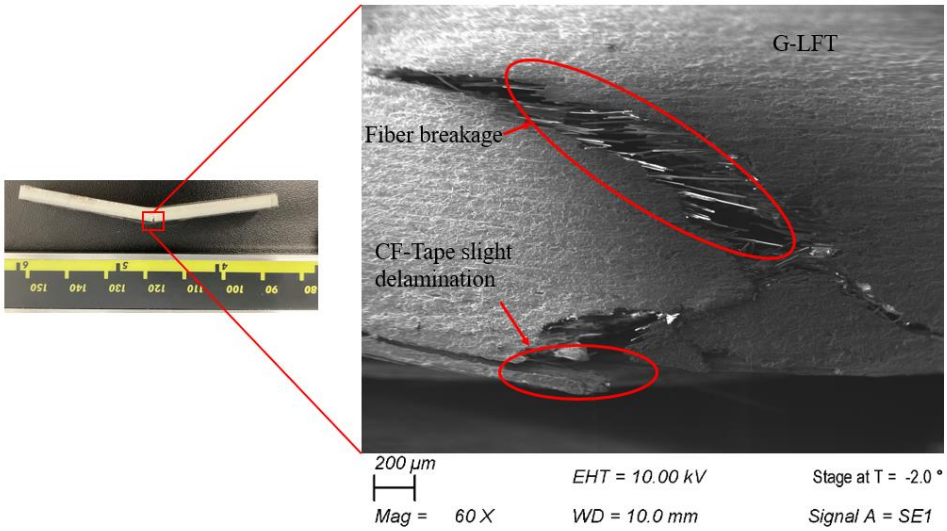


Figure 2.9. SEM image of the fractured overmolded G-LFT/CF-Tape sample after flexural testing. The image shows crack initiation in the G-LFT region and slight delamination at the interface, indicating good bonding. Fiber breakage within the G-LFT and matrix remnants on the CF-Tape surface suggest a mixed cohesive-interfacial failure mode.

dimensions and peak load of each specimen. The failure strength was calculated by dividing the peak load by the bonded area of each specimen. Although slight thickness variations were present, they did not affect the calculated strength since the failure load was normalized by the bonded cross-sectional area. The variation in peak load primarily reflected dimensional differences, but these were accounted for in the strength calculation, resulting in a consistent average value with less than 5% standard deviation.

It can be concluded that the peak load values were directly correlated with the thickness of the specimen. Thickness variation in the samples was observed during the manufacturing of substrate G-LFT. During ECM process, the hot charge (270°C) was placed on the relatively colder mold (at 65°C), resulting in uneven material flow and thickness variation. However, this variation was limited to the peak load only, and the average failure strength was 7.5 MPa with less than a 5% standard deviation, as illustrated in Figure *2.10*

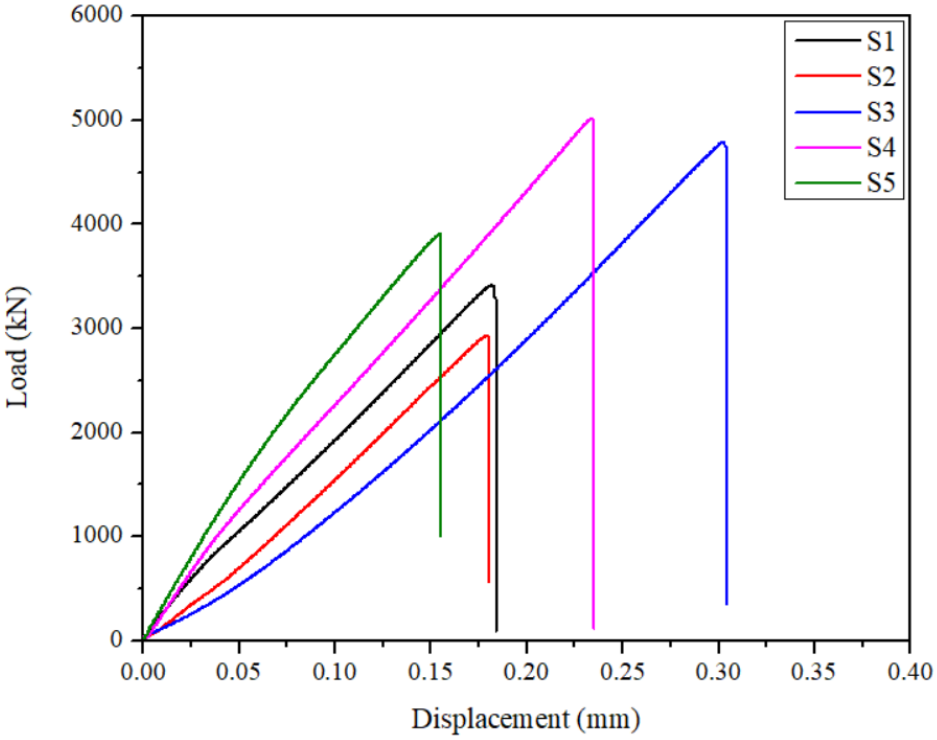


Figure 2.10 Load-displacement curves from flatwise tensile tests of G-LFT/CF-Tape overmolded specimens. The sudden load drops indicate brittle failure behavior. Variations in peak load are attributed to differences in sample thickness, while all specimens showed similar failure mechanisms.

Quan et al [37] showed that the flatwise tensile strength of the PEEK joints bonded by the carbon fibre prepreg attained an average of 7.6 MPa before attaining complete failure. Saeed et al [38] achieved an out-of plane tensile strength of 7 MPa for a continuous carbon fibre reinforced 3D printed polymer Composites.

2.3.5 Tensile (in-plane) test

The tensile strength of the overmolded part indicates an increase from 51 MPa to 117 MPa (~129%) in strength, and from 8MPa to 13 GPa (~62%) in modulus as shown in Figure *2.12*. All specimens failed according to ASTM D3039, in the gauge length area.

Table 2.1.Dimensions and peak load of the overmolded samples tested under flatwise tension. While thickness normalization was applied in the stress calculations, variability in peak load remained due to factors such as interfacial bonding quality and adhesive layer consistency.

Specimen	Thickness (mm)	Diameter (mm)	Flatwise Strength (MPa)	Average and Std Deviation
S1	4.65	25.51	6.46	
S2	4.55	25.26	6.20	
S3	4.75	25.34	6.78	7.52 ± 0.34
S4	4.81	25.46	9.31	
S5	4.70	25.31	7.63	

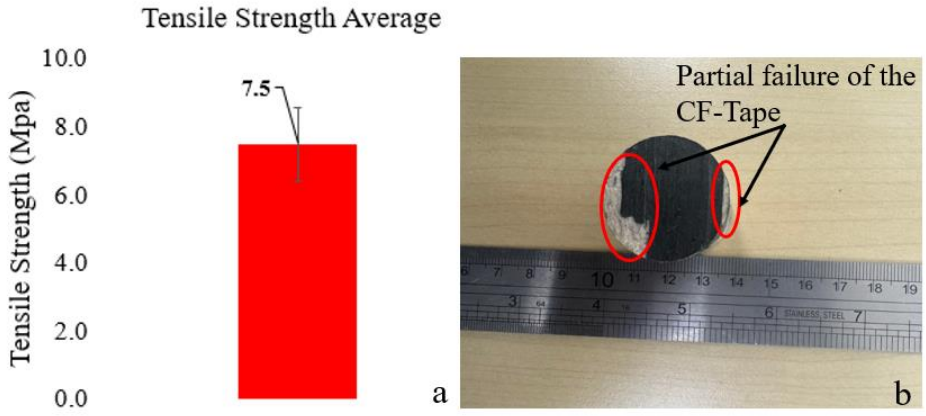


Figure 2.11 Flatwise tensile strength of the G-LFT/CF-Tape overmolded part. (b) A partial failure of the CF-Tape on the interface between the G-LFT and each patch of the tape processed on the ATP.

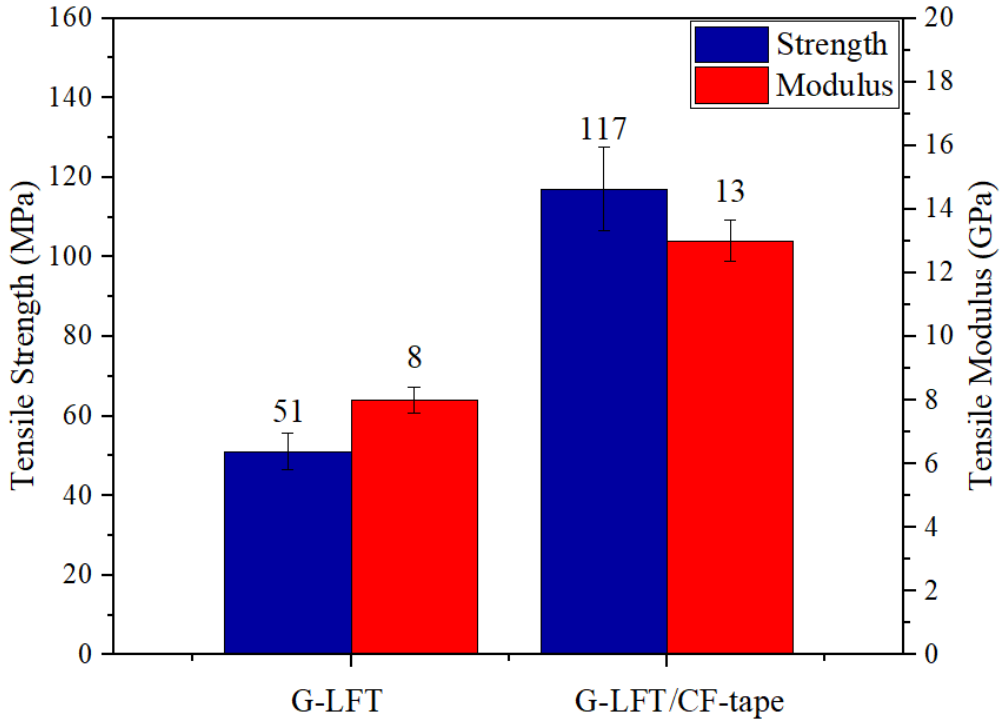


Figure 2.12 Tensile properties of the G-LFT and G-LFT/CF-Tape. An improvement of 128% and 62% in tensile strength and modulus, respectively, were achieved in the G-LFT/CF-Tape compared to G-LFT.

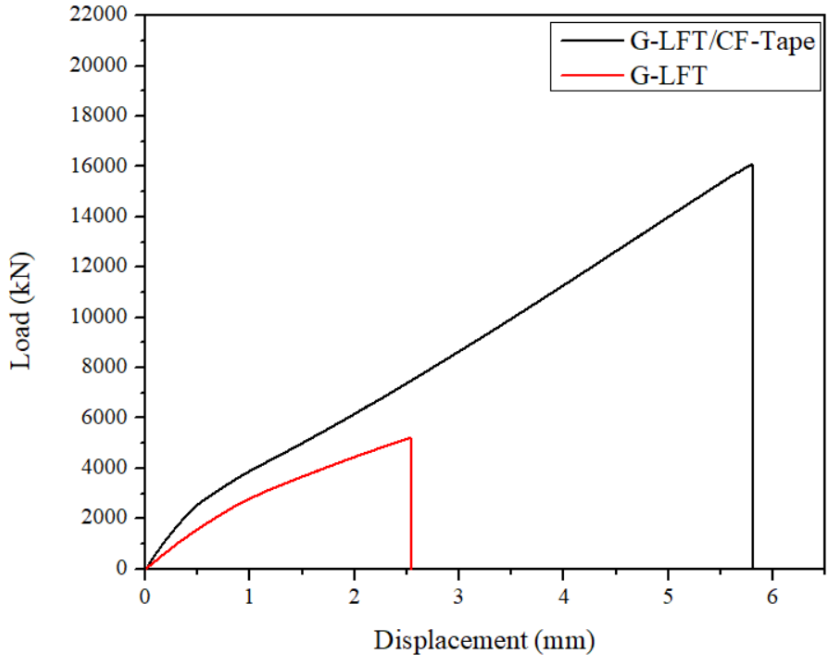


Figure 2.13 Load versus displacement for the tensile test showed the failure behavior for the G-LFT and the G-LFT/CF-Tape, demonstrating a strong in-plane bonding on the interface.

Figure 2.13 illustrate the load versus displacement for the tensile tested coupons. The linear response for the in-plane tensile test and the brittle failure (sudden drop) at the ultimate strength showed a good bonding between the fiber and the matrix (G-LFT) as well as on the interface between the overmolded CF-tape and the substrate G-LFT. SEM investigations of the overmolded G-LFT/CF-Tape samples showed that macroscopically visible inter-bundle fractures were accompanied by interfibre fractures of the CF-Tape. Matrix cracks, which grew parallel to the tensile direction were present as shown in Figure 2.14 Failure between fibers and the matrix and the breakage of individual carbon fibers (CF) caused the discontinuous phase to fail in the transition zone [77]. The discontinuous G-LFT mainly failed due to layers separating. Although fibers broke at a microscopic level, it became visible when whole fiber bundles failed together. As shown in Figure 2.13 both samples (G-LFT and G-LFT/CF-Tape) showed brittle failure at maximum load, highlighting a bond strength of 117 MPa.

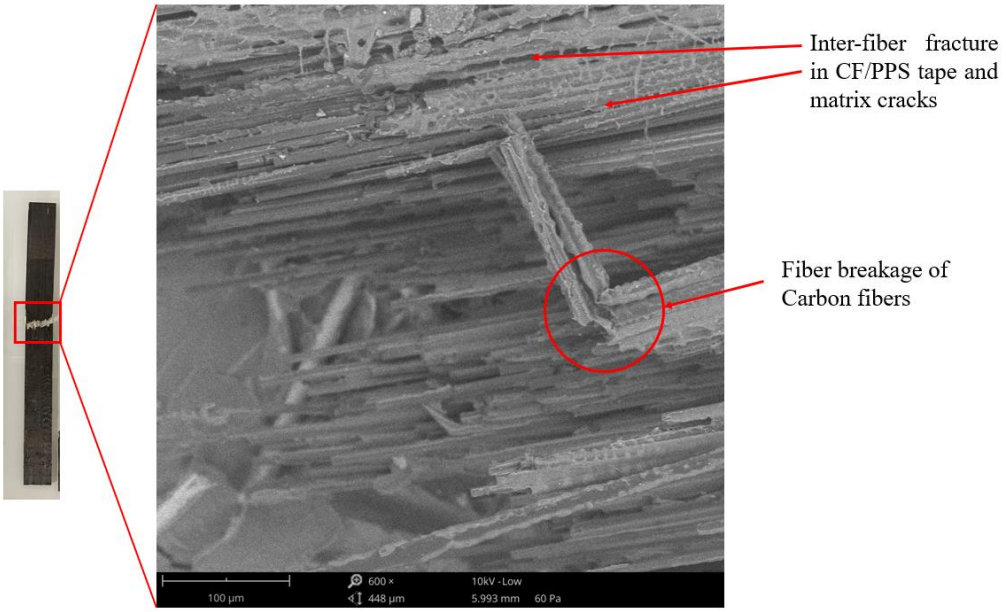


Figure 2.14. SEM image of the fractured G-LFT/CF-Tape interface after tensile testing. Matrix cracking and carbon fiber breakage are observed due to strong interfacial bonding, which enabled effective load transfer into the CF-PPS layer. The resulting fiber and matrix

failure confirms good adhesion at the interface and the activation of composite action rather than premature delamination.

2.3.6 Drop-Tower (low-Velocity) Impact Test

The LVI Test was performed on both samples G-LFT and G-LFT/CF-Tape to understand the impact behavior. Table *2.2* summarizes the LVI results as the initial impact energy, energy absorption concerning maximum force, and deformation.

Table 2.2. Results summary of the tested specimens.

Specimen ID	Input Energy (J)	Average Contact Force (N)	Average Deformation (mm)
G-LFT	34.02	3010.12 ± 284.30	16.96 ± 2.34
G-LFT/CF-Tape	34.02	2886.09 ± 287.30	19.56 ± 1.87

The impact energies were 20J, 25J, 30J, and 34J respectively. No visible damage was observed on the samples before 34J energy. Therefore, only 34J impact energy results are explained in this work. The damage to the back surface of both samples is shown in Figure 2.15. The G-LFT specimen showed a hemispherical-shaped crack, the same as the dimensions of the impactor. Whereas a vertical crack along the direction of the CF orientation was observed in the overmolded sample. The crack orientation was observed due to the delamination of CF tape and energy was released along the easy path as the direction of fibers.

Figure 2.16 shows the force versus displacement behavior of both samples. It can be observed that both samples exhibited continuous loading and unloading forces. In hybrid samples, the impact energy is dissipated in various ways fiber/ matrix failure, delamination, friction, etc. [40]. Notably, both samples were impacted such that the G-LFT surface was struck (top surface). The G-LFT sample contains several chopped fibers, which led to

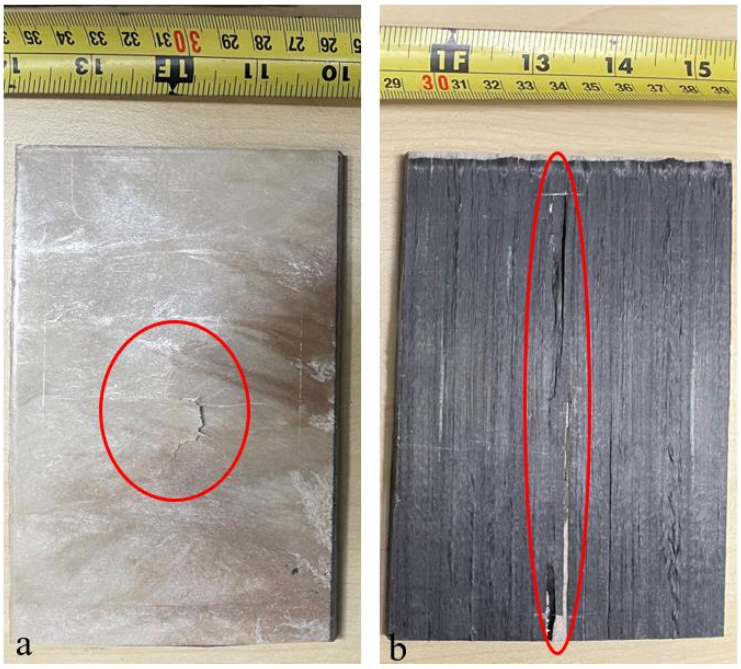


Figure 2.15 10.16 x 15.24 cm (4x6 in) G-LFT tested composite panels. (b) 10.16 x 15.24 cm (4x6 in) G-LFT/CF-Tape tested panel. A vertical crack along the direction of the CF orientation was observed in the overmolded sample. The crack orientation was observed due to the delamination of CF tape.

microcracking and resulted in a loading and unloading type of failure. The G-LFT/CF-Tape sample exhibited a maximal force response that was 10% lower than the G-LFT force response while showing a 15% increase in displacement at the time of failure. Ideally, the hybrid sample should have a higher load and lower displacement since CF has greater strength and glass fiber has a higher elongation [41]. In this study, only one layer of CF (0.16mm thick) was added, while the G-LFT was ~3.2mm thick. Therefore, further evaluation is needed to understand the exact failure mechanism, which was beyond the scope of this work.

Figure *2.17* compares the force/energy versus time curves for both samples to indicate the perforation energy (total energy absorption) behavior. Perforation energy is the sum of damage initiation energy (Ei) and damage propagation energy. The damage initiation energy for G-LFT was 12.5 J, while for G-LFT/CF-Tape, it was 15 J. This increase in Ei was due

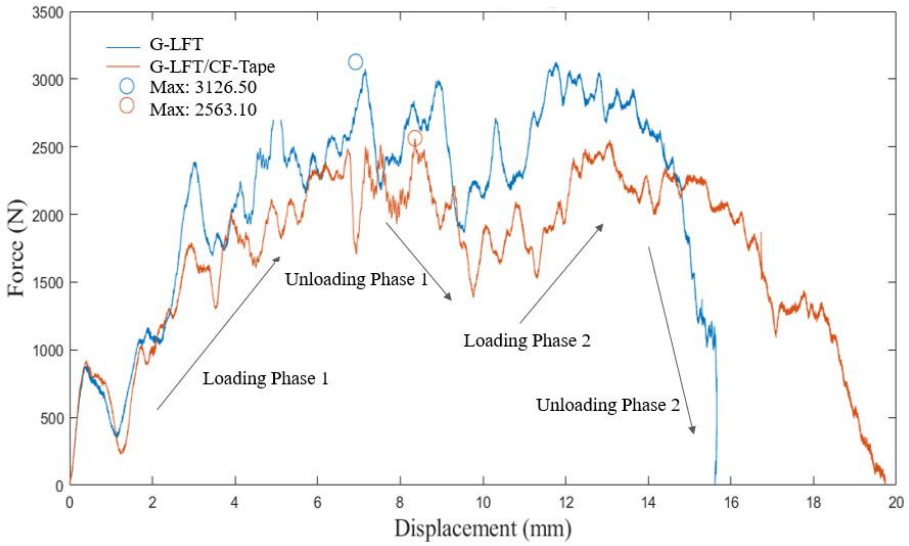


Figure 2.16. Force-displacement curves from low-velocity impact (LVI) testing of G-LFT and G-LFT/CF-Tape specimens. Both samples show a loading-unloading response typical of hybrid composites. The overmolded sample exhibits greater deformation and slightly lower peak force, attributed to energy dissipation through interfacial delamination and fiber-matrix failure mechanisms. Blue G-LFT/CF-Tape specimens, orange G-LFT specimens.

to the addition of a well-bonded CF layer, which improves the sample's ability to absorb more energy. However, both samples absorbed the same total perforation energy of 34 J, as shown in Figure 2.17. The energy required to fracture the carbon fibers in tension is approximately equal to that needed to break the glass fibers in tension (due to the higher strength of the carbon fibers, but the larger strain to failure of the glass fibers) [78]. Additionally, localized delamination and early-stage debonding at the interface may have redirected damage propagation and allowed for more extensive deformation under impact. Similar observations have been reported by Cantwell and Morton[79], who noted that delamination in hybrid composite structures can promote energy dissipation while increasing compliance, leading to greater deformation without a corresponding rise in absorbed energy. The presence of slight interfacial delamination and matrix cracking, as observed in the post-impact inspection, supports this mechanism.

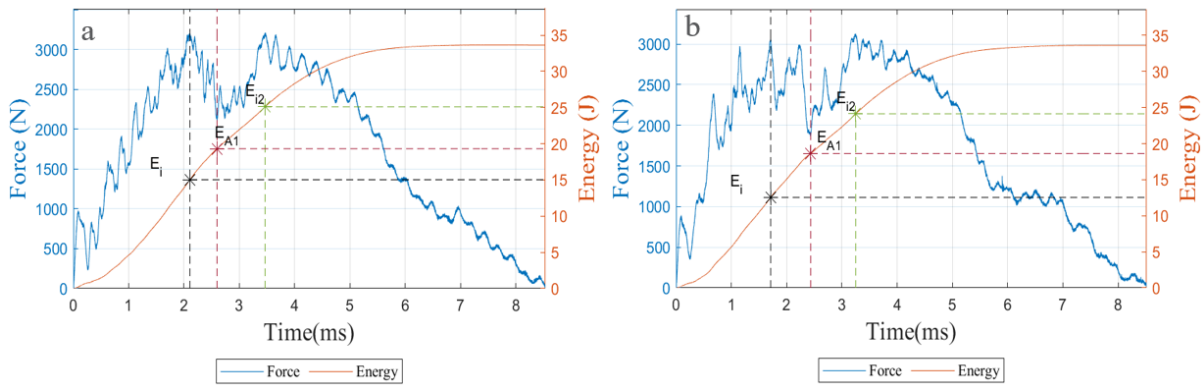


Figure 2.17 LVI Force/Energy-time response depicting the damage initiation energy "E_i" at both peaks and the damage propagation energy "E_A" at the two minimal values during unloading phases. (a) G-LFT/CF-Tape specimens (b) G-LFT specimens.

2.3.7 Finite Element Analysis

A numerical model was used to reduce the number of experimental iterations, as testing multiple parameter combinations experimentally is time-consuming and logistically challenging. The flexural test was conducted numerically with a representative boundary condition similar to the experiment. The model simulates micromechanics behavior using the commercial software Ansys Academic 2023-R2.

Table *2.3* shows the measured material properties from experiments. The LFT layer was considered as a pseudo-isotropy property. However, the CF-Tape was utilized as an orthotropic material, which has an orientation of [0°] along its length. The testing parameters were used same as the experiment, i.e., the span length (54.5mm), and control rate (1.59 mm/min) to apply the desired force.

A mesh sensitivity analysis was carried out to evaluate the proper mesh sizing for both the G-LFT and the CF-Tape layers. For the CF-Tape layer, the fiber orientation was mapped on the solid elements. The CF-Tape layer has four layers of solid hexagonal elements through the thickness of the layer, which was specified based on the sensitivity analysis. The G-LFT part has eight layers of elements through the part thickness. Both the G-LFT part and the CF-Tape

Table 2.3. Materials properties for the finite element model collected from the experimental measurement and from the Material Data Sheet (MDS) of the material provided by the manufacturer[80].

Material	Density [kg/m^3]	Isotropic elasticity				
		Young's modulus [GPa]	Poisson's ratio [-]	Bulk modulus [GPa]	Shear modulus [GPa]	Tensile ultimate strength [MPa]
G-LFT	1.62	6.25	0.37	10.26	2.92	55.0
Material	Density [kg/m^3]	Orthotropic elasticity				
		Young's modulus (x-, y-, z-directions) [GPa]	Poisson's ratio (xy, yz, xz) [-]	Shear modulus (xy, yz, xz) [GPa]	Tensile ultimate strength [MPa]	Compressive ultimate strength [MPa]
CF-Tape	1.59	134.0 9.25 1.0	0.37 0.37 0.37	3.50 3.50 0.10	2020.0	1100.0

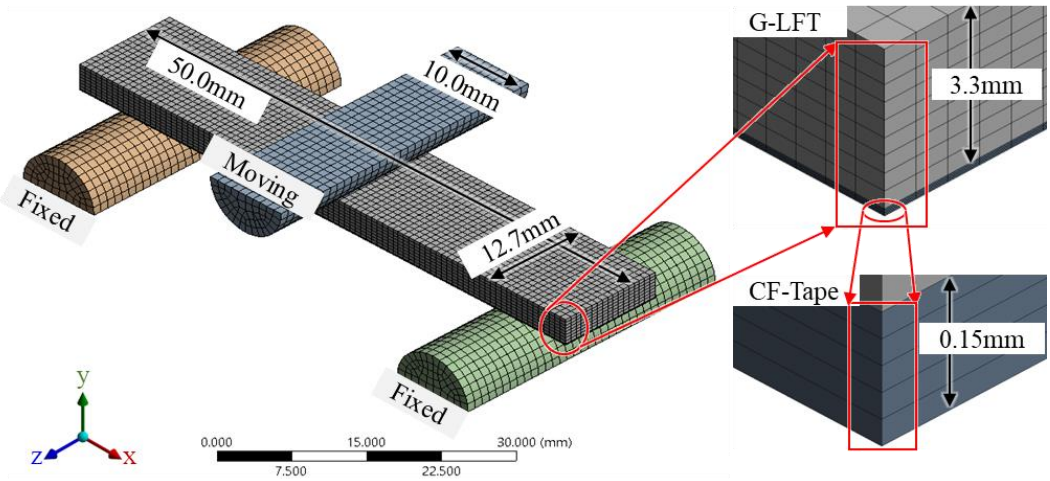


Figure 2.18 Mesh distributions for G-LFT substrate and CF-Tape layer. The figure illustrates the mesh for the tested parts and the three-point bending mechanism as rigid bodies.

layer have 17 elements and 90 elements along the x- and y-directions respectively, as shown Figure 2.18. A total number of 18,360 elements was found to be an optimal mesh number. The contact between the G-LFT part and the CF-Tape layers was assigned as a bond, and the contacts for the supports were assigned frictional contact. The model is validated against the experimental data. Numerical stresses to strain curves of the G-LFT part and the overmolded CF-Tape layer with the G-LFT part were compared to the experimental data. Both curves had the same trend as the experimental curves, as shown in Figure *2.19*. However, some discrepancies were observed, as the hybrid part exhibited slight non-linear behavior not captured by the numerical model, which assumed defect-free materials and ideal contact conditions. To simplify the analysis, the material was defined with linear properties-an assumption generally consistent with experimental trends, especially after CF-Tape reinforcement. For G-LFT, the model slightly overpredicted strength due to its limitations in capturing nonlinear effects such as fiber pull-out, matrix yielding, and progressive damage, along with assumptions of perfect bonding and uniform fiber orientation. In contrast, the G-LFT/CF-Tape configuration showed smaller deviations, indicating better model accuracy, though idealized interface conditions and lack of damage modeling still contributed to some

overprediction. Additional differences may also stem from strain rate sensitivity and testing conditions not reflected in the simulation.

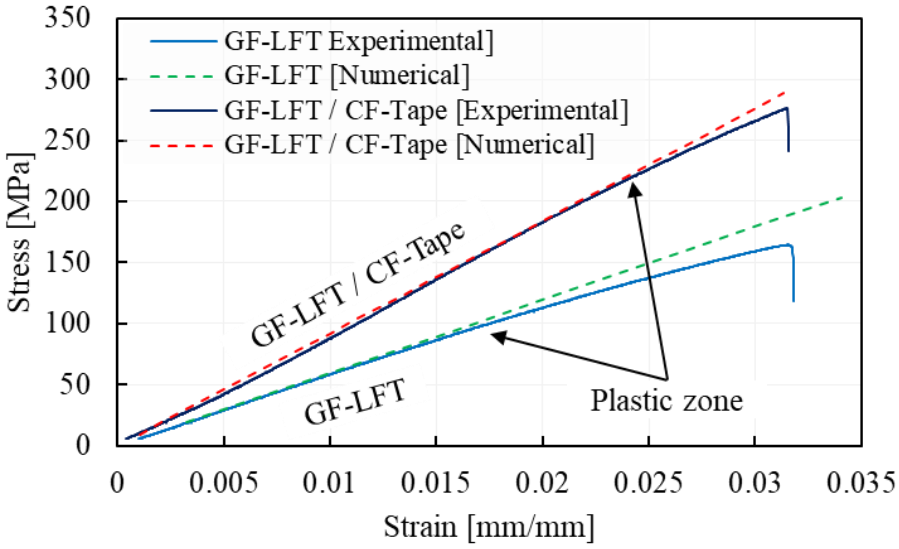


Figure 2.19 Comparison between experimental and numerical stress-strain curves for flexural testing of G-LFT and G-LFT/CF-Tape, demonstrating good agreement and validating the simulation model.

Figure 2.20 (A) and (B) shows the numerical stress of the G-LFT/CF-Tape, the numerical results behavior was similar to the experimental results. The same deflection behavior was replicated, as the force applied was controlled by the control rate. The failure criteria were used to evaluate the failure of the CF-Tape layer, as shown in Figure 2.20 (C) and (D). The model predicted the failure of the CF-Tape in the same manner as the experimental test. The ultimate strength of the CF-Tape was recorded in Table *2.3*.

The model was used to stress, deflection, and failure. A parametric analysis investigated the optimal number of CF-Tape layers that need to be overmolded. A total number of five layers of CF-Tape (5 x 0.15mm) was considered in the model. The aim was to optimize the required number of layers to provide sufficient strength to the material. The layers were added sequentially one-by-one to capture the effect of overmolding the CF-Tape. All the layers had the same material properties, as used in

Table 2.4, and all the layers were defined using [0°] fiber orientation. The parametric analysis uses six cases, Case A to Case F, whereas each case has an added extra layer of CF-Tape. Starting with no CF-Tape layer in Case A, Case B use one layer, then Cases C uses two CF-Tape layers, etc. The structural analyses of the added layers show that the added layers distributed the load evenly in the whole part, as shown in Figure 2.21. The stress was not concentrated at the center of the beam, as observed for the one-layer case. In Figure 2.21, failure criteria show the behavior of the overmolded CF-Tape layers, by order.

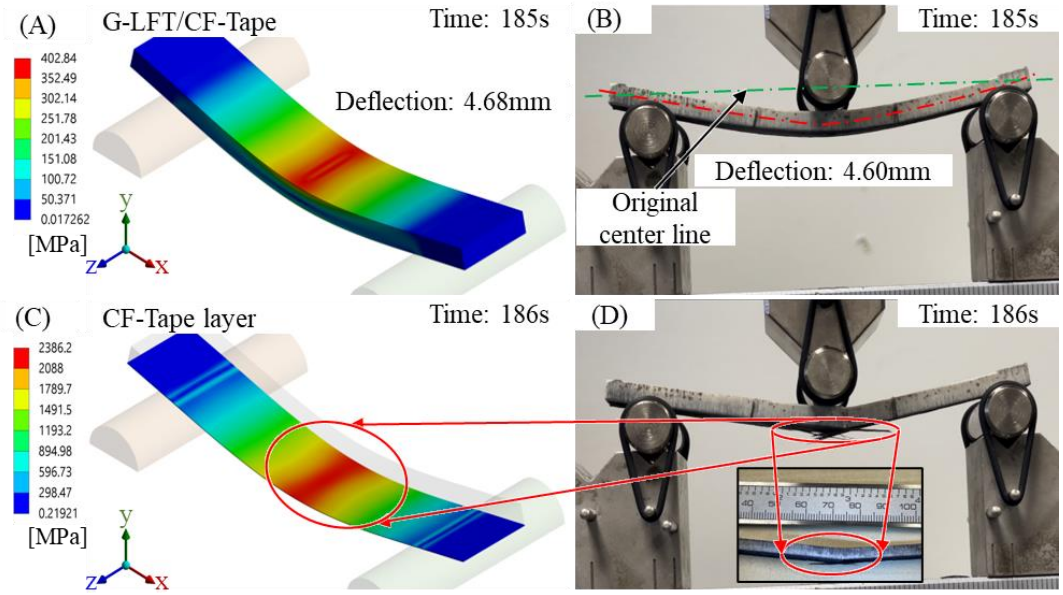


Figure 2.20 (A) Von Mises stress of the applied load, (B) deflection of the part. (C) and (D) failure monography of the CF-Tape layer numerically and experimentally respectively.

Table 2.4. Failure limits of the CF-Tape.

Material	Orthotropic stress limits	
	Tensile [GPa]	Shear [MPa]
CF-Tape	x- 2.02	xy-80.0
	y- 2.02	yz-80.0
	z- 2.02	xz-80.0

The first layer of CF-Tape experiences the initial failure. Subsequent layers don't utilize the same level of stress concentration as the first layer. When the first layer fails, the load is then transferred to the subsequent layer, leading to a gradual failure. The addition of CF-Tape layers enhances stress distribution in the G-LFT component, resulting in increased stress tolerance before failure.

The CF-Tape layers add a significant value to strengthen the G-LFT part. In Figure 2.22 the exerted forces to displacement were recorded to all cases, and describe the forces increase as the number of CF-Tape layers increase. A gain of 10.0% in strength was achieved by overmolding a single CF-Tape layer. The stress increased tremendously by 60.0%, by adding five CF-Tape layers, as shown in Figure 2.23.

Summary

The aim of this work was to manufacture and characterize an overmolded part using two different techniques. The ECM has been selected as an industry scale manufacturing technique, with a rate of 1 part/min (discontinuous part) to produce the G-LFT substrate, while the ATP was selected among the traditional technique of laying down UD-tape. The ATP has been conducted in the study to enhance the local strength of the part, with high speed, efficiency, and automation. The final overmolded composite showed an enhancement of ~190% in flexural strength and ~110% in modulus. The tensile strength and modulus increased by 128% and 62 % respectively. The interface bonding was investigated using SEM and OM before and after testing, the captured image showed a good bonding on the interface between the G-LFT and the CF-Tape. A slight delamination was noticed after the mechanical testing. However, the mechanical property of the whole part was not affected. For that purpose, the effect of mechanical and non-mechanical treatment(s) would be studied in the future to improve the interface bonding between the CF-Tape with the substrate. An Ansys

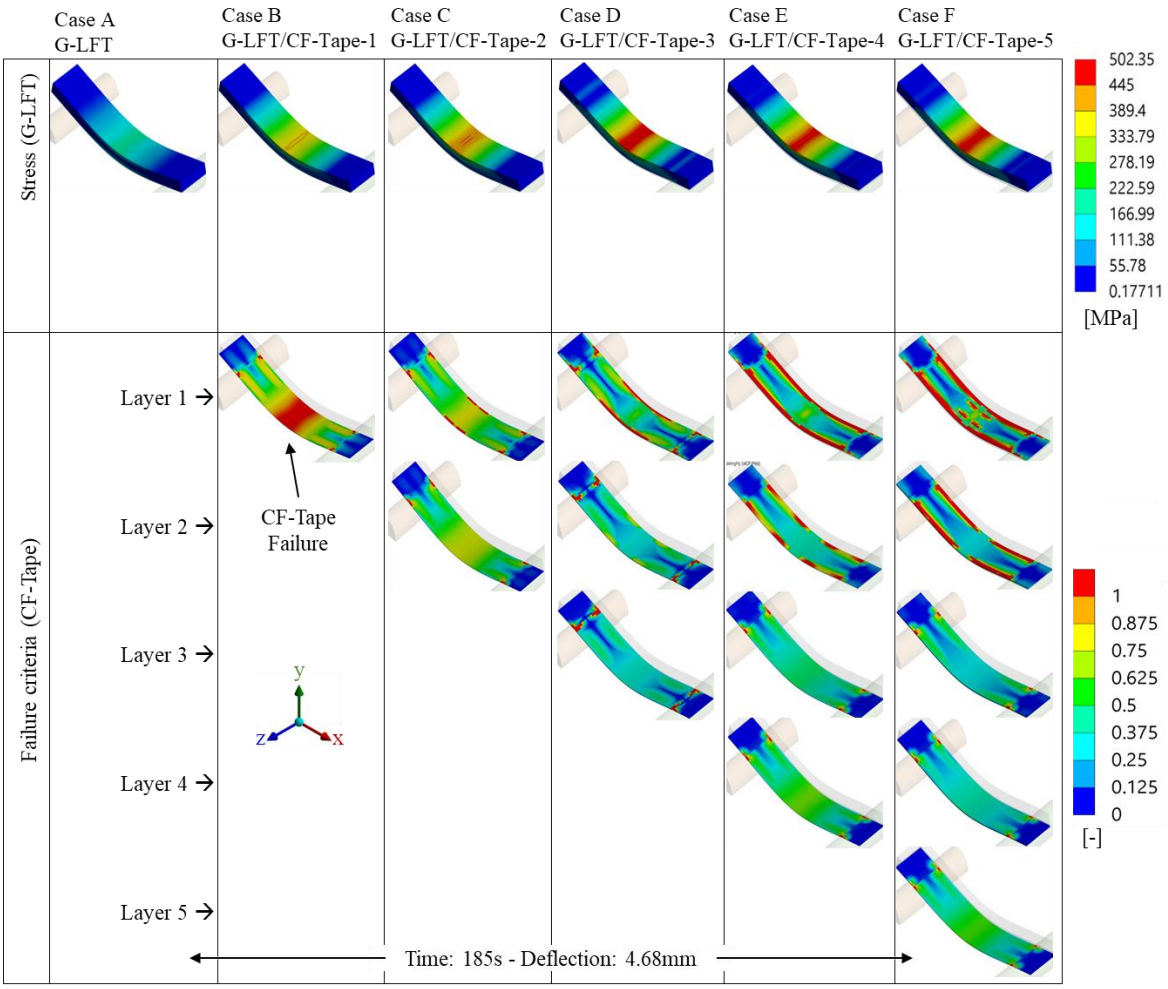


Figure 2.21. On top, Von Mises Stresses for the overmolded part with different number of CF-Tape layers. The stress range shows the ability of the overmolded parts of supporting more load by adding additional layers of tapes. On bottom, the corresponding failure response of each layer individually. From the left side, the single layer of tape failed quickly, however adding more layers distributed the load evenly through thickness and prevented progressive failure.

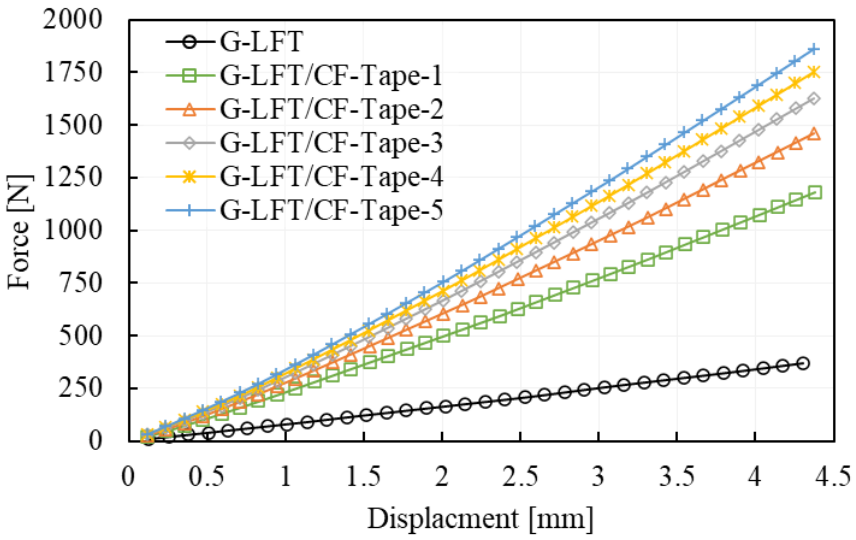


Figure 2.22. Numerical prediction of stress–strain behavior for G-LFT with increasing numbers of overmolded CF-Tape layers. The results show that adding CF-Tape layers progressively enhances the composite's stiffness and ultimate strength, indicating improved load-bearing capacity and more efficient stress distribution.

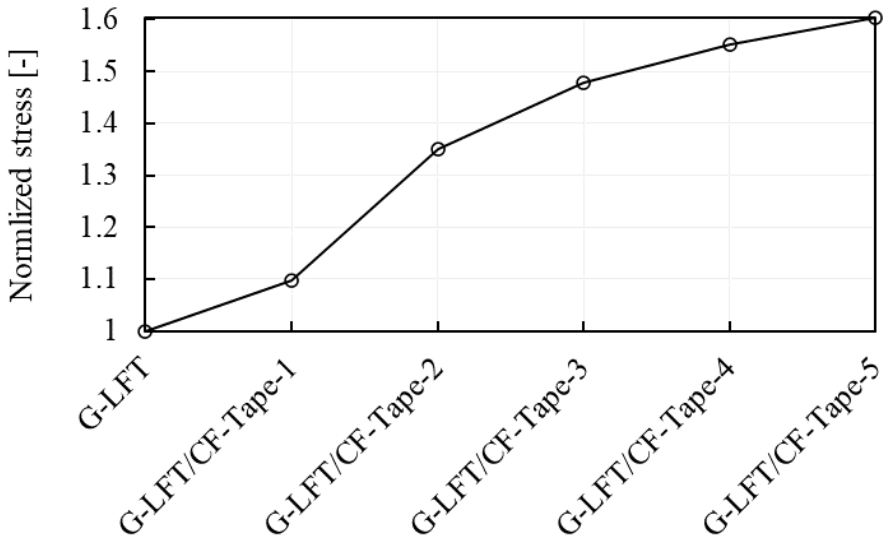


Figure 2.23. Normalized stress predictions showing the strengthening effect of multiple CF-Tape layers overmolded onto G-LFT, with up to 60% improvement after five layers.

based FEA model was used to study the effect of overmolding CF-Tape layers on strengthening the long glass fiber thermoplastic. The addition of CF-Tape layers enhances ultimate strength and stress distribution in the long glass fiber thermoplastic part. The [45]model showed the gradual increase in strength of maximum 60% by adding five layers of CF-Tape. The model also allows for simulation of CF-Tape layers with varying fiber orientations, providing flexibility to assess different reinforcement strategies and their impact on localized strength.

3. CHAPTER 3

Effect of plasma treatment on LMPAEK/CF tape and composites manufactured by ATP

Abstract

ATP process is widely used in aerospace for its advanced process control and multi-axis capabilities but faces issues like limited choice of materials and suboptimal tape consolidation. This study investigates air plasma treatment on ATP carbon fiber thermoplastic feedstock tape to address these challenges. The effects on low melt Polyaryletherketone/carbon fiber unidirectional tape (LMPAEK/CF UD tape) were analyzed. Treated and untreated tapes were used to fabricate composites and evaluated for physical, thermal, mechanical, and interfacial properties. AFM, X-ray photoelectron spectroscopy (XPS) and FTIR analyses revealed surface roughness changes (on LMPAEK), extent of oxidation, and the presence of hydroxyl/carboxyl groups. Composites from plasma-treated tapes showed a 7.6% increase in tensile strength, 8% in tensile modulus, 18% in flexural strength, and 8.3% in flexural modulus. The interlaminar shear strength improved by 18.7%. Failure analysis showed untreated composites failed via inter-ply and fiber-matrix delamination, while treated composites experienced matrix cracking and fiber breakage. This study highlights atmospheric plasma treatment as a solution to ATP's limitations, significantly enhancing LMPAEK/CF UD tape composites' properties.

3.1 Introduction

Composite materials are essential in engineering applications across industries such as aerospace, automotive, wind energy, and sports. The performance of composites relies on the interaction between three critical components: the matrix, reinforcement, and the interface. The matrix, which can be either metal or polymer (thermoset or thermoplastic), binds the reinforcement (particulate or fiber) and enhances the resulting mechanical properties like strength and stiffness. The interface between matrix and reinforcement is crucial for stress transfer and influences durability and mechanical performance [1-7]. Prior research emphasizes that the interfacial quality is affected by factors such as the reinforcement's size,

surface chemistry, and physical features, including surface roughness. The performance properties of composite can be tailored for typical applications by leveraging surface modification treatments [8-14].

Surface modifications, particularly plasma treatments, have demonstrated the potential to improve interfacial bonding. For instance, Sharma et al. [15] showed that plasma treatments introducing hydroxyl groups on carbon fibers (CF) can enhance interfacial shear strength by 90%, significantly improving the stress transfer between fibers and the matrix. Further studies on surface treatments, including oxidation, nanoparticle deposition, and irradiation, corroborate the benefits of modifying carbon fiber surfaces to improve composite performance [16-18].

ATP is a cutting-edge composite manufacturing technique employed to fabricate advanced aerospace components. ATP uses heat and pressure to lay pre-impregnated unidirectional (UD) tapes onto a mandrel, consolidating them in-situ. However, challenges remain in mitigating porosity and enhancing interfacial bonding, often necessitating secondary processes like compression molding [19-23].

Several studies have examined plasma treatment's effect on enhancing composite bonding in different polymers. For instance, Li et al. [24] demonstrated a 138% increase in shear bond strength in 3D-printed PEEK/CF after atmospheric plasma treatment. Yildirim et al. [25] observed up to an 84-fold improvement in fracture toughness in CF/PEKK composites after plasma treatment. Jyongsik et al. [26] reported a 52% increase in flexural strength in plasma-treated CF/PEEK composites. Zhang et al. [27] demonstrated that oxygen plasma treatment of carbon fiber-reinforced epoxy composites reduced the water contact angle from ≈75° to 0°, leading to a 30% improvement in lap shear strength. Similarly, Lu et al. [28] investigated air and argon plasma treatments on CF/PEEK composites, showing a 12.4% increase in interfacial shear strength (IFSS) after 1 minute of air treatment and a 41% increase with argon

plasma. These studies underscore the potential of plasma treatments to improve interfacial bonding in high-performance composites.

While prior research has focused on high-melting polymers like PEEK and PEKK, limited studies have investigated plasma treatments on low-melting polyaryletherketone (LMPAEK), especially in the context of ATP manufacturing. No published work, to our knowledge, addresses the air plasma treatment of LMPAEK with carbon fiber in an integrated ATP process, which forms a critical gap in understanding how to optimize in-situ consolidation without secondary processes.

This study aims to bridge that gap by exploring the use of plasma treatment to enhance the interfacial bonding of LMPAEK/CF tapes during in-situ consolidation in ATP manufacturing. Specifically, the objective is to eliminate the need for secondary processes, such as compression molding, by applying plasma treatment directly to LMPAEK/CF UD tapes, which are then processed via ATP. The effectiveness of the plasma treatment is evaluated through various characterization techniques (contact angle, scanning electron microscopy (SEM), X-ray photoelectron spectroscopy (XPS), AFM) and performance metrics, including physical, thermal, mechanical, and interfacial properties of the resulting composites.

3.2 Experimental

3.2.1 Materials

LMPAEK based UD tape was used to fabricate composites using the ATP system. The ATP hot gas torch head designed and developed by Automated dynamics in 2013 was attached to a Kawasaki ZZX130L 6-axis robot owned by Trelleborg Group, Sweden. The tape comprises a LMPAEK with a melting temperature of 304° C, and a processing temperature of 340° C. The 6.35 mm wide UD tapes were purchased under the trade name of TC1225 LM PAEK/AS4D (34% resin content by weight) (thickness of tape: 0.15 mm), supplied by Toray Advanced Composites, Morgan Hill, CA, USA.

3.2.2 Plasma Treatment of the UD tape

Plasma treatment is a clean surface treatment, configured using parameters such as treatment time, power, pressure, working gas or carrier gas (depending on its function) - its composition, flow rate, and treatment distance. On the other hand, ATP is a process that lays tape at a specific speed, temperature, and pressure. On the other hand, ATP is a process that lays tape at a certain speed, temperature, and pressure. It was essential to optimize treatment time/speed by keeping the rest of the parameters constant. The air plasma treatment was conducted using Plasma jet (RD1004 Rotary Jet) and generator (FG5001 Openair-Plasma® Generator) supplied by Plasma treat GmbH, Steinhagen, Germany. The plasma jet was kept static with respect to the horizontal plane with a flow rate of 20L/min. The 6.35 mm wide UD tape was passed under the generated plasma, keeping a 12.7 mm distance between the nozzle and tape, as shown in Figure 3.1.

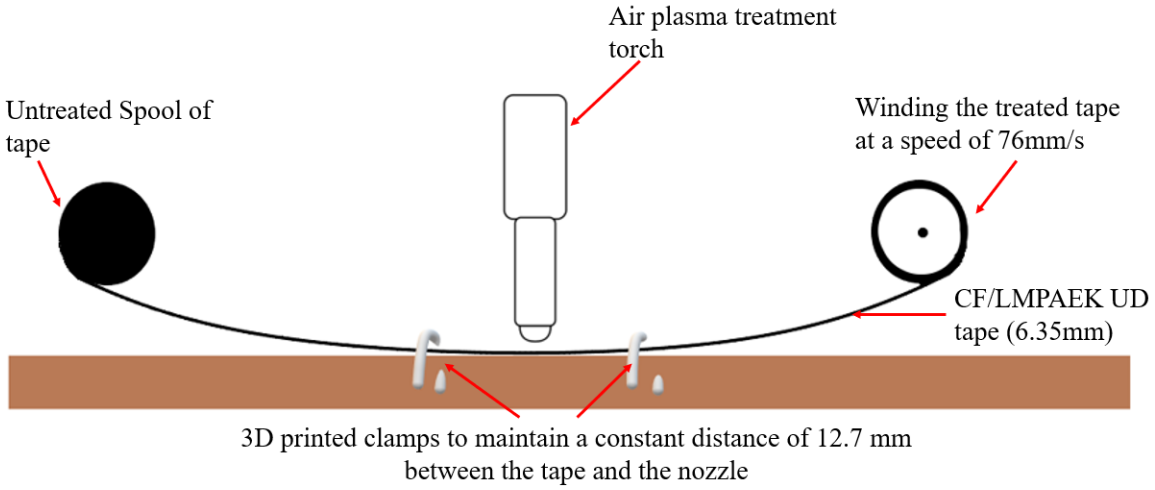


Figure 3.1. Illustration of the treatment setup used to treat the LMPAEK/CF UD tape. The tape was treated at the same speed as the deposition rate of the ATP (76 mm/s).

3.2.3 Development of ATP-based composite laminate

The composites were developed using the ATP system as shown in Figure *3.2*. The hot gas torch (HGT) was heated to 840° C (torch temperature) to achieve the nip point temperature of ~ 330° C; a 6.35 mm steel compaction roller with a pressure of 140 N was used, followed by

laying 18 layers of UD tape in one direction (0°) over an aluminum flat mandrel of 1.2 m x 1 m size. The speed of ATP was maintained at 76 mm/s, which was in sync with the speed of the plasma treatment. The composites developed with treated and untreated tape are referred to as CT and CU, respectively.

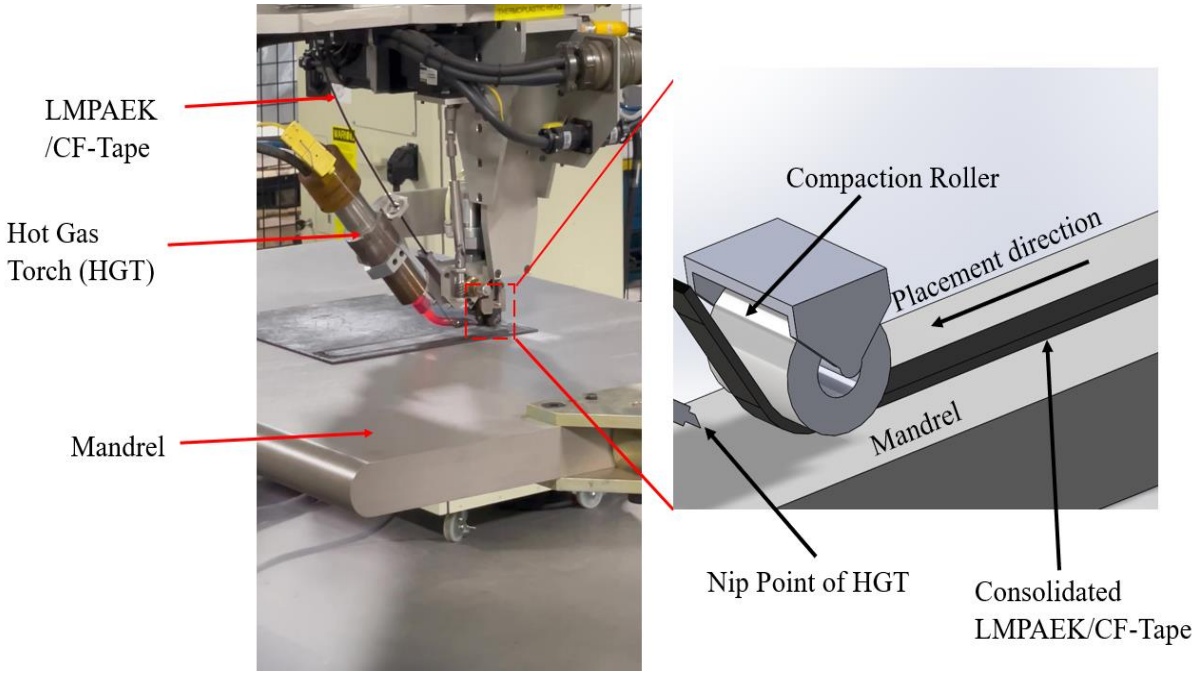


Figure 3.2.Schematic depicting the ATP working principle. The LMPAEL CF- tape originates from the feedstock, is subsequently heated by the HGT, and undergoes in-situ consolidation as a specific load is applied through the compaction roller.

3.2.4 Characterization of LMPAEK/UD tape

3.2.4.1 Contact angle study

Contact angle studies were performed on treated and untreated tapes using Kruss Goniometer with deionized (DI) water. A drop of 2 µL of DI water (rate of 0.5 µL/s) was placed on the tape sample (6.35 mm x 50.8 mm), 10 samples from different zones of the tape were tested to ensure consistency. Stabilized angles were measured using the ellipse fitting method [29]. Each sample was repeated 8-10 times, and the average values were reported.

3.2.4.2 Electron microscopy of LMPAEK/CF UD tape

Apart from functional groups, surface treatment (oxidation, plasma, nanoparticle-based treatments) can result in the etching of the carbon fiber surface, thus improving surface roughness [30]. In this study, SEM (Phenom XL G2) was employed to observe the physical changes imparted by plasma treatment to the treated tape. The gold coating was employed to avoid excessive charging and facilitate smoother raster scans.

3.2.4.3 Fourier Transform infrared of LMPAEK/CF UD tape

FTIR spectrophotometer Vertex-70v was employed for the study. The tape was cut into 6.35 x 6.35 mm and used to collect the FTIR spectra in Transmittance mode. For each sample, 100 scans were recorded in transmittance from 500 to 3500 cm−1 wavenumber.

3.2.4.4 X-ray photoelectron spectroscopy (XPS) surface studies of LMPAEK/CF UD tape

X-ray Photoelectron Spectroscopy (XPS) was utilized to examine the surface of LMPAEK/CF UD tape using a Thermo Scientific K-Alpha X-ray photoelectron spectrometer. This instrument operated in Fixed Transmission Mode with a pass energy set at 200 eV for survey spectra and 50 eV for core-level spectra. It utilized a monochromatic Al Kα radiation source (1486.6 eV) operating at 420 W (14 kV; 30 mA) for incident radiation. Emitted Electrons were collected at a 90° angle from the sample, while maintaining a pressure of around 10^-9 mbar (10^-7 Pa). Six LMPAEK/CF UD tape T and U samples were analyzed. One U sample while the other five were T for 5 sec, 10 sec, 15 sec, 30 sec, and 60 sec (named accordingly – T5, T10, T15, T30, and T60). T and U tape samples were attached directly to the XPS sample holder with metal clips followed by spectra acquisition. Shirley background was used for elemental quantification. All measurements were done on the top-middle of tape surface.

3.2.4.5 Atomic force microscopy of LMPAEK/CF UD tape

Cypher AFM (Asylum Research an Oxford Instruments company, Santa Barbara), tabletop system was used in this study. Silicon probes (AC160, OLYMPUS) (tip radius: 7 nm) with an approximate spring constant of 26 N/m and a resonance frequency of around 300 kHz were employed for all AFM measurements. The imaging was conducted in tapping mode within the attractive regime. For processing purposes, all topography images underwent 0th order flattening. The treated and untreated samples were carefully prepared followed by mounting them on carbon tape and subsequently on the AFM stage. 3 samples (6.35 x 6.35 mm) were prepared, and multiple iterations of areal scans were conducted to understand physical, mechanical changes caused by air plasma treatment.

3.2.5 Characterization of the treated and untreated composites

3.2.5.1 Atomic force microscopy of LMPAEK/CF UD tape

XRD studies on the treated and untreated composites were evaluated using Empyrean X-ray setup, with a Kα radiation at 30mA and 40kV passing through a ½° divergence slit before interaction with the sample. A set of 5 square samples (20 x 20 mm) were cut off from the laminated composites using a water jet system. The test was conducted at a scan rate of 5°/min for 2Θ varying from 5° to 90°. The XRD data were plotted to find the percentage crystallinity of the tested samples. XRD analysis was performed on LMPAEK/CF UD tape before and after plasma treatment. The crystallinity was calculated with the help of the following equation:

$$\chi_c = \frac{Area\ of\ the\ crystlline\ peaks}{Area\ of\ the\ crystlline\ peaks + Area\ of\ the\ amorphous\ peaks}\ x\ 100 \qquad \text{(Eq 3.1)}$$

3.2.5.2 Thermogravimetric analysis

Thermogravimetric analysis (TGA) was performed using a TA instrument. Samples of ~50 mg were placed in a small lead pan while heating was generated with a rate of 10° C/min

from 0° to 800°C in the presence of air. Purge gas flow rate to TGA chamber was maintained around ~50 mL/min with nitrogen.

3.2.5.3 Dynamic mechanical analysis (DMA)

Dynamic mechanical analysis was conducted using TA instruments' QS500. The experiments were conducted from 50°C to 350°C at a ramp rate of 5° C/min at 1 Hz frequency. 2-3 samples with dimensions of 56 x 12 x 2.7 mm (Length x width x thickness) were prepared from each laminated composite in accordance with ASTM D7028 standards. Tests were conducted in three-point bending mode. Storage moduli, loss moduli, and tan delta were recorded as a function of temperature during the experiment.

3.2.5.4 Interlaminar shear strength (ILSS) study

ILSS tests were conducted in accordance with ASTM D2344. To minimize edge roughness, the specimens were cut using a water jet cutting machine (OMAX 2626, Jet machining center). The tests were conducted in a 3-point bending configuration with a 1.0 mm/min crosshead speed. At least 5 specimens/samples 27 x 5.4 x 2.7 mm (length x width x thickness) were tested to ensure repeatability and statistical relevance.

3.2.5.5 Flexural strength and modulus study

Test Resources (Model 313 series), Minneapolis, MN, universal testing machine (UTM) with 50 kN load cell was used to perform a three-point bend test of the composites in accordance with ASTM D790. A set of 10 specimens with dimensions of 54 x 12.7 x 2.7 mm (length x width x thickness) of each was produced using the waterjet cutting machine. The control rate (0.75mm/min), stress, and strain were calculated based on the test standard.

3.2.5.6 Tensile strength and modulus study

A set of five specimens was prepared for tensile testing according to ASTM D3039. The average width and length of the tensile coupon were 15 mm and 254 mm, with a thickness of 1.7mm. The test was performed on the 50 kN load cell test resource frame, and samples were

pulled at 2 mm/min loading rate. The tensile strain was monitored using an axial extensometer Model 3542, Epsilon Technology Corp, Jackson, WY, USA.

3.2.5.7 Fractography

The failed tensile and ILSS samples were analyzed to understand the failure mechanisms. The samples were observed with SEM, QUANT FEG 650.

3.3 Results

3.3.1 Characterization of the LMPAEK/CF UD tape

3.3.1.1 Contact angle study of LMPAEK/CF UD tape

Figure 3.3 illustrates the changes in water contact angle with varying plasma treatment durations. The untreated LMPAEK/CF UD tape initially exhibited a contact angle of 87°, which decreased to 79° after a 5-second plasma treatment. The reduction in contact angle, corresponding to the highest oxygen content (~28%), can be attributed to the saturation of surface functional groups. Once the surface reaches this saturation point, further oxidation has a diminished impact on wettability. Additionally, increased oxygen concentration may alter surface morphology, such as introducing micro-roughness, which limits further reductions in the contact angle. This behavior is consistent with prior studies showing that beyond a certain threshold, further oxidation yields diminishing returns in wettability improvements [31].

As the treatment time extended to 10, 15, 30, and 60 seconds, the contact angle further dropped to 24° and 22°, then increased to 36° and 37°, respectively. The rise in contact angle after extended plasma exposure is likely due to increased nano-scale surface roughness, which is known to affect wetting behavior [32]. The overall decrease in contact angle reflects an increase in surface free energy and the development of hydrophilic functional groups on the tape's surface, indicative of oxidation.

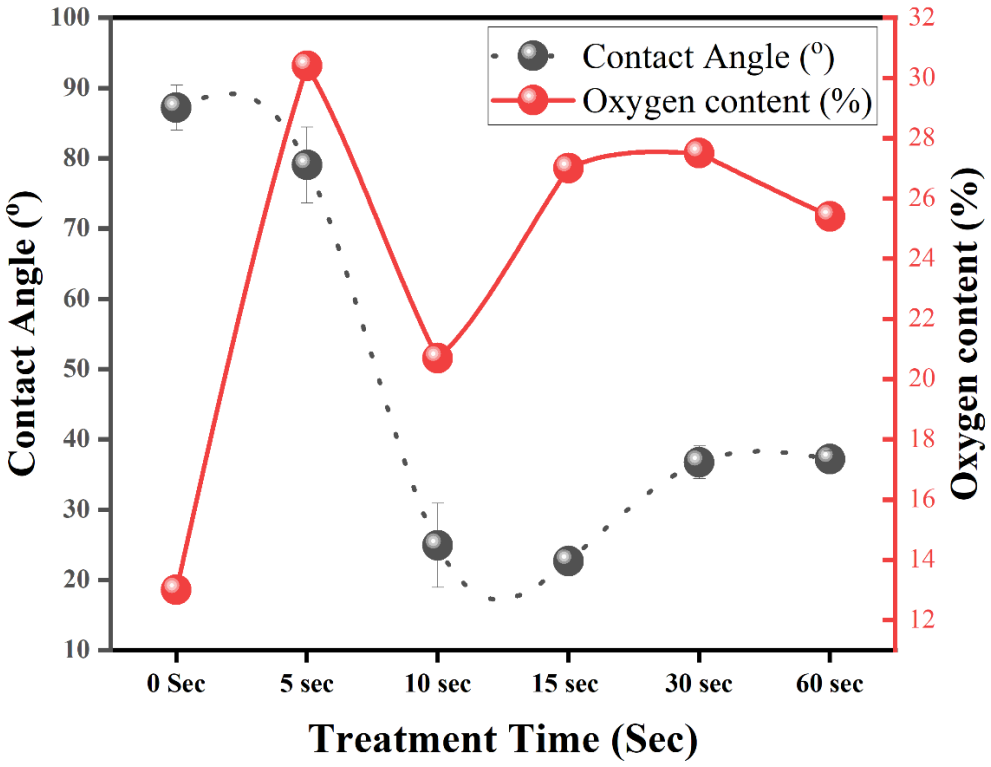


Figure 3.3. The contact angle for the treated tape as a function of treatment time:

With the increase in plasma treatment time, the contact angle reduced drastically. Additionally, with the increase in contact angle after 15 sec treatment time, it increases again due to an excessive increase in surface roughness [81]. The right Y axis shows the increase in oxygen content on the surface (analyzed from XPS spectra), i.e., polarity with treatment time. An increase in oxygen content on the treated tape surface was found to be nonlinear with treatment time, however, demonstrates the effectiveness of treatment.

Figure 3.4 depicts the contact angle photographs for treated and untreated samples. In the case of Figure 3.4a (untreated sample), the contact angle was 87° due to borderline hydrophobicity on CM/LMPAEK tape caused by the lack of hydrophilic moieties on LM-PAEK. With treatment, the contact angle was reduced to 22°, as seen in Figure 3.4b. The fall in contact angle for treated tape is supported by XPS and FTIR data. Increase in concentration of hydrophilic moieties and oxygen content demonstrated by FTIR and change in % oxygen content through XPS in subsequent sections.

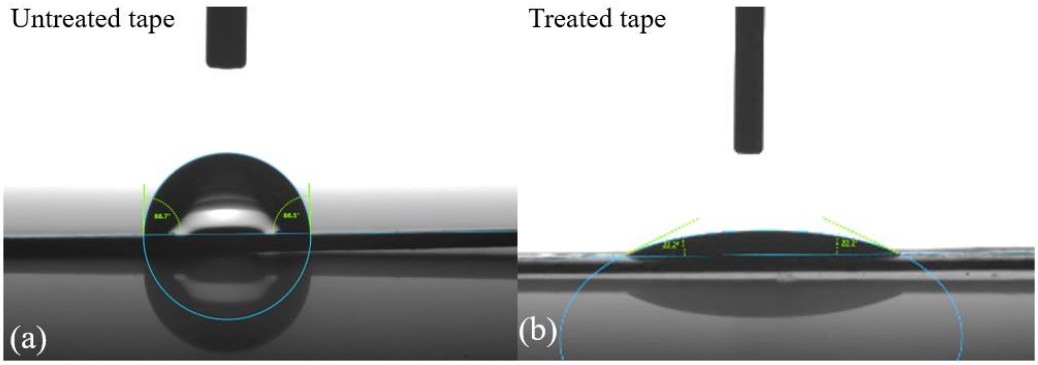


Figure 3.4. Contact angle measurement optical image plasma untreated tape (a) and the treated tape (b). Reduced contact angle post plasma treatment is effect of formation of hydrophilic moieties on the surface of ATP tape, cleaner surface.

3.3.1.2 FTIR analyses on the LMPAEK/CF UD tape

LMPAEK is a semicrystalline thermoplastic polymer characterized by the Phenylene rings (R-rings) attached to ether, carbonyl and ketone via oxygen bridges (O) as shown in Figure 3.5. During air plasma treatment, oxygen and nitrogen-based reactive species activates the surface of the media [34].

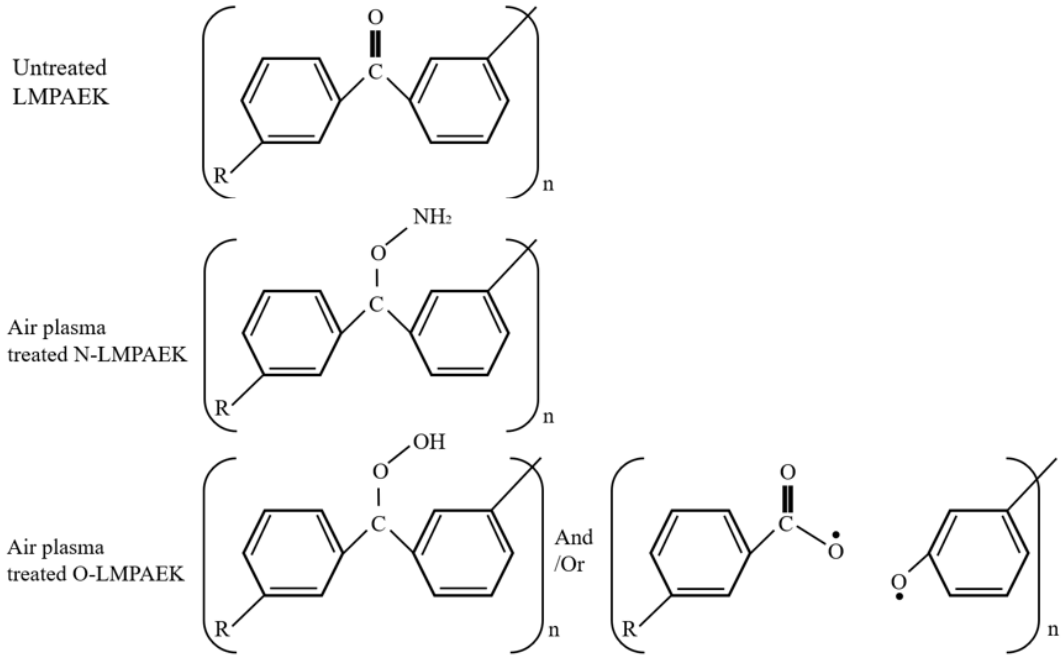


Figure 3.5. Possible chemical changes of LMPAEK/CF UD tape due to air plasma treatment[82, 83].

Fu et al [35] reported the possible chemical groups occurred during H-plasma and O-plasma treatment of PEEK, same family as LMPAEK. Based on their study and on the literature, it could be assumed that during the air plasma treatment the C=O bond may have been converted into C-O-OH, O-C=O in case of Oxygen and/or C-O-NH2 by plasma-reactions from Oxygen and Nitrogen plasma-species as shown in Figure 3.6. FTIR studies were conducted on the treated (T) and untreated (U) LMPAEK/CF UD tape to understand the chemical functional group variation of the tape. The peaks observed in the range from 3000 cm-1 to 3150 cm-1 in the T tape were assigned to O-H functional group due to plasma treatment in comparison with the U tape. The peaks ranging from 2650 cm-1 to 2750 cm-1 shows the presence of the C-H and C-O stretch and it can be noticed that the intensity of the peaks in the T tape is higher than the U one. The existence of the C-H/O stretch with low intensity in the U tape could be related to the presence of phenyl group (C6H5-). (Carboxyl group (C-O stretched) could be observed as well in the range between 1450 cm-1 and 1750 cm-1 with stronger peaks intensity in the T tape compared to U. An intense peak was observed between 2160 and 2250 cm-1 in the absorbance sector that could be referred C≡C or C≡N. The increased intensity of the polar functional groups, in the plasma treated samples can enhance the bonding interactions with the adjacent tape through mechanisms such as covalent and hydrogen bonding, resulting in improved adhesion and mechanical properties [37, 38].

3.3.1.3 XPS surface studies of LMPAEK/CF UD tape

A wide binding energy range survey spectrum was acquired on each sample to identify all elements present. A set of narrow energy range core level spectra were acquired for each identified element. A second set of data (survey and core level spectra) were acquired at a different area of each sample to gain some insight into the surface uniformity. Figure *3.7* shows the overall surface composition of each sample. High resolution spectra result further

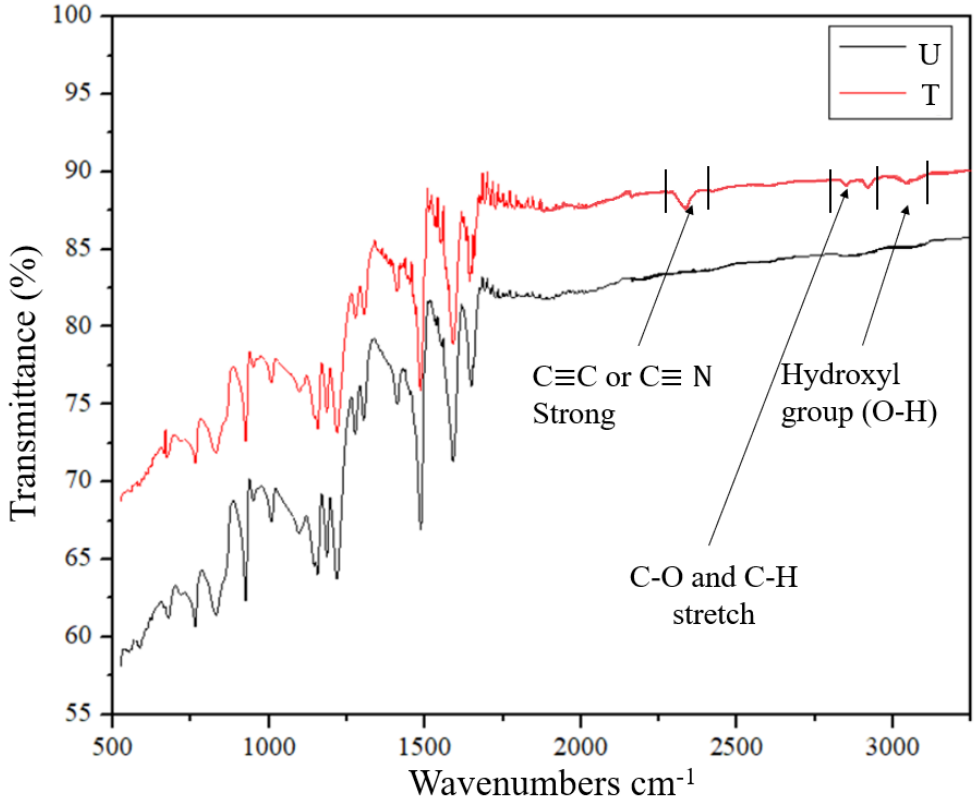


Figure 3.6. FTIR spectrum of the LMPAEK/CF UD treated and untreated tape.

Appearance of a new peak between 2160 and 2250 Cm^{-1}. The intensity of the hydroxylic group and C-O stretch and C-H stretch are higher in the T tape compared to U.

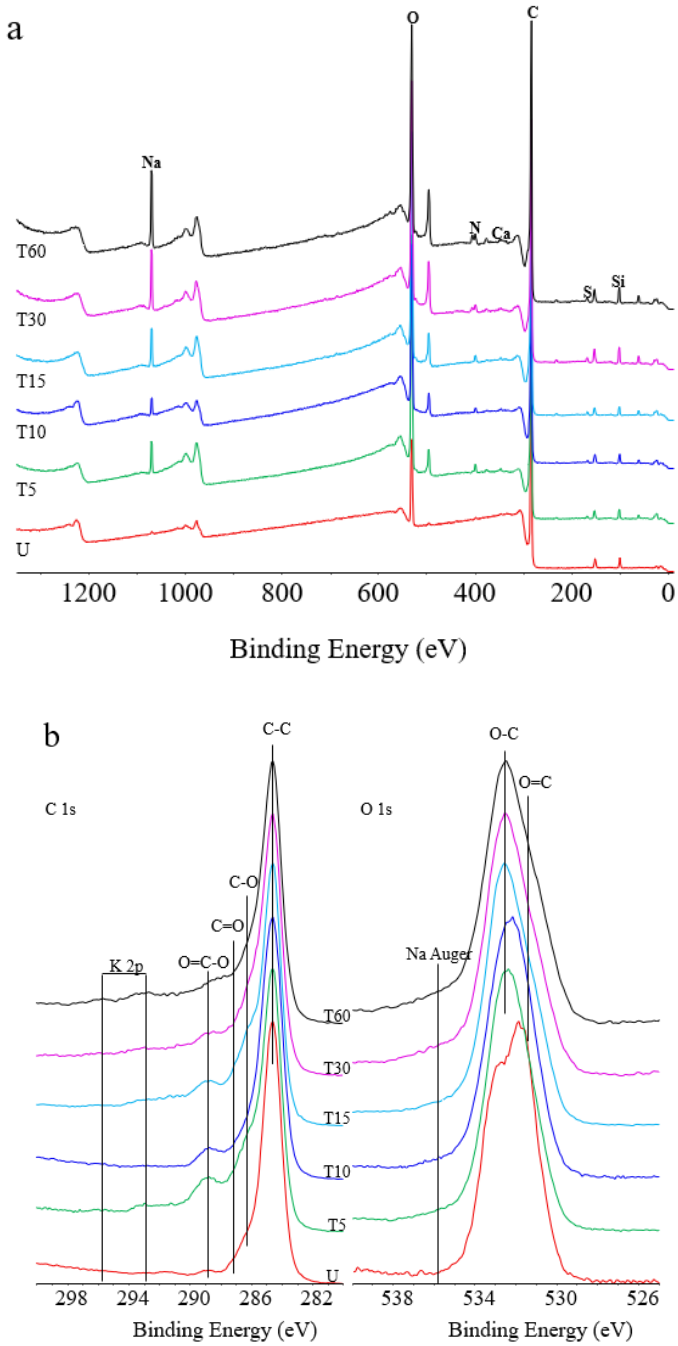


Figure 3.7 XPS survey spectrum (a) for the U and T LMPAEK/CF UD tape.

The peaks intensity of Oxygen (O) and Nitrogen (N) are higher in the T samples compared to the U emphasizing the effect of plasma treatment on the surface. (b) deconvoluted XPS spectra for C 1s and O 1s.

corroborated the data from FTIR and contact angle wettability studies, indicating more oxygen bonded carbons (C-O and O-C=O) on the surface than C-C bonds due to air plasma processing.

The amount of carbon (C) for the sample U i.e. untreated tape was highest. With treatment, the C content decreased, and oxygen (O) content improved. The increase in O content depicts the oxidation imparted by the plasma on the tape surface. The O increased from 13 at. % for the tape U to above 25 at. % for the tape T sample (Tape T-5sec) showed highest oxygen content of 30 at. %, the 5 sec treatment equivalents to with typical ATP layup speed (76mm/sec), N also increased for each of the T samples (~1-3 at. %) as compared to the U sample as shown Table *3.1*.

Table 3.1 Surface Composition (at. %) for the U and T LMPAEK/CF UD tape for element C, O and N.

	C	**O**	**N**
U	82.8	13.0	0.6
T5	62.1	30.4	1.7
T10	73.9	20.7	0.9
T15	66.1	27.0	1.4
T30	61.3	27.5	2.3
T60	62.7	25.4	2.9

3.3.1.4 Microscopy studies of LMPAEK/CF UD tape

Surface treatment oxidizes the carbon fiber surface through different oxidation mechanisms, introducing a range of functionalities, both chemical and physical, on the surface of carbon fibers [15]. Physical functionalities may include creating a rougher surface and increasing the surface area, which can improve mechanical interlocking between the fiber and matrix and remove weaker regions from the fiber surface [15]. In the current study, the change in surface

was qualitatively studied using SEM. Figure 3.8 depicts the SEM micrographs for untreated (a) and plasma-treated (b) tape.

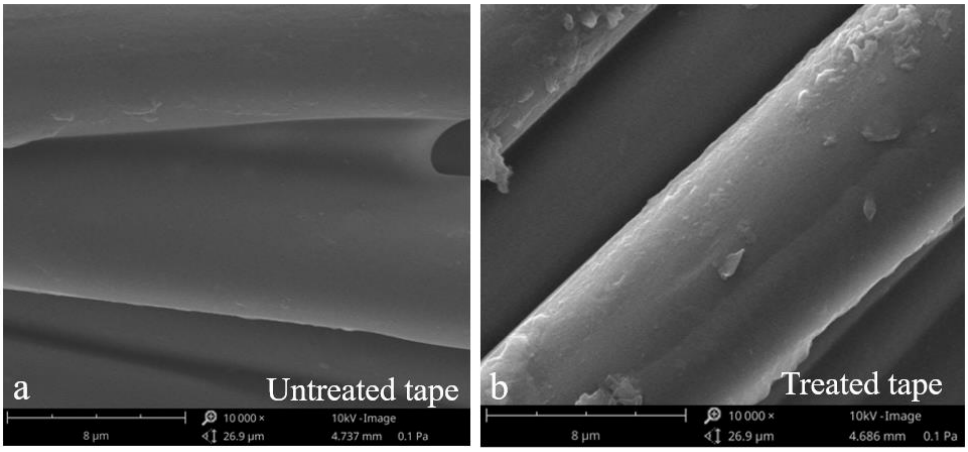


Figure 3.8. SEM micrographs for U (a) and T (b) LMPAEK/CF UD tape: SEM micrographs depict nature of attack of plasma species.

U (untreated tape) tape depicts uniform and coherent surface with no surface damage, whereas the plasma treated tape shows vivid feature i.e., increased surface roughness, deeper crevices, and blistering of LMPAEK in the T (treated tape) tape.

It is evident from Figure 3.8 (a) that untreated tape possesses a smooth surface and no defect or physical etching. In the case of Figure 3.8 (b) i.e., for treated tape, surface roughness was observed, resulting from the interaction of polymeric surface of tape with ionic species and free radicals during plasma treatment.

3.3.1.5 AFM of LMPAEK/CF UD tape

Figure 3.9 presents surface topology images obtained via AFM, comparing the surface topography of plasma-treated and untreated samples within both fiber-rich and polymer-rich regions. Observations from fiber-rich regions, Figure 3.9 (a, b), highlight inter-fiber crevices, appearing as deep valleys. Substantial variation in inter-fiber crevices has been observed across the entirety of both samples which hampered direct quantitate evaluation of surface roughness in these regions. However, simple qualitative analysis reveals that the fiber surfaces are smoother in untreated samples, a finding corroborated by SEM observations.

However, as mentioned the significant height disparities and curved surface across fibrous areas hindered accurate quantitative assessment of surface roughness. Further measurements in the flat areas have been conducted, polymer-rich regions situated between the fibrous areas. Figure 3.9 (c, d) presents 2D height images for untreated and treated samples, specifically targeting these polymer-rich regions. Utilizing a grayscale across all images facilitates an immediate and clear comparison, illustrating a noticeable increase in surface roughness following plasma treatment. Quantitative analysis of the root means square roughness indicated a more than twofold increase, from 320 pm to 820 pm standard deviation, between untreated to treated samples respectively. The relatively smoother surfaces of these polymer-rich regions enabled the determination that the treated samples exhibit distinct surface features, a direct result of the interaction between mixed ionic species and the LMPAEK surface. Surface roughening increases the effective bonding area, improves the surface area for convective heat transfer between heated N2 gas and LMPAEK/CF tape, improving mechanical interlocking between the tape and substrate. This enhanced interaction leads to better consolidation during the ATP process.

Interaction of plasma species with polymer could result in change in chemical, physical and mechanical properties of surface through different mechanisms such as micro-etching, cleaning of organic contamination and chain scission vis-a-vis polymer degradation [84]. The AFM profile obtained in this study suggests micro-etching and chain scission as active mechanism. The dominant effect usually depends upon operating parameters of plasma treatment and determines extent of surface functionalization, crosslinking and degradation [85, 86]. For treated sample, it was observed that there was change in the surface roughness, and it was effect of surface cleaning i.e. removal of surface adsorbed contamination, degradation of low molecular weight moieties and polymer chain scission on carbon fiber rich and polymer rich area, which could create further low molecular weight polymer surface

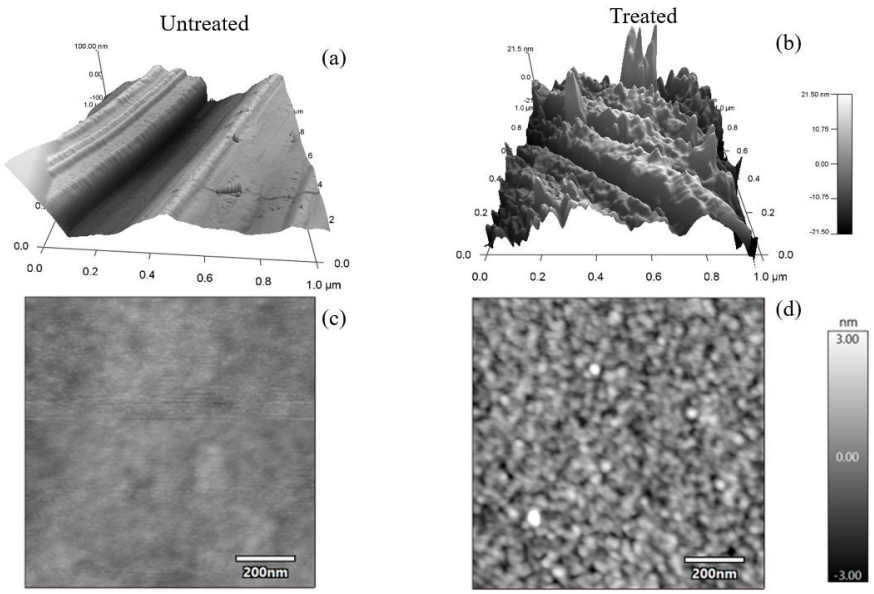


Figure 3.9. Comparative AFM topography imaging of LMPAEK/CF UD tape for both untreated (a, c) vs. treated (b, d) samples. Panels (a) and (b) depict 3D topography focusing on fiber-rich regions. Panels (c) and (d) are 2d images for polymer rich regions, illustrating changes in surface structure post-treatment.

layer [87]. Figure 3.10 (a) shows untreated tape's polymer rich region depicts relatively uniform surface and change in roughness over the region, whereas Figure 3.10 (b) illustrates wide variation in roughness across the region depicting the polymer surface etching achieved by plasma treatment. The Grayscale on the right of 2D profiles portrays the extent of difference in the Z axis variation.

3.3.2 Characterization of the treated and untreated composites

3.3.2.1 Thermogravimetric analysis

Figure 3.11 illustrates the results of thermogravimetric analysis for both treated and untreated tapes, revealing only a slight modification in thermal degradation behavior. Table 3.2 presents the temperatures at which 5% (T5) and 10% (T10) weight losses occur for the developed composites. The untreated composite labelled C_U exhibits marginally lower T5 and T10 temperatures in comparison to its counterpart, C_T. This increased weight loss observed in both composites can likely be ascribed to enhanced oxidation, a consequence of exposure to

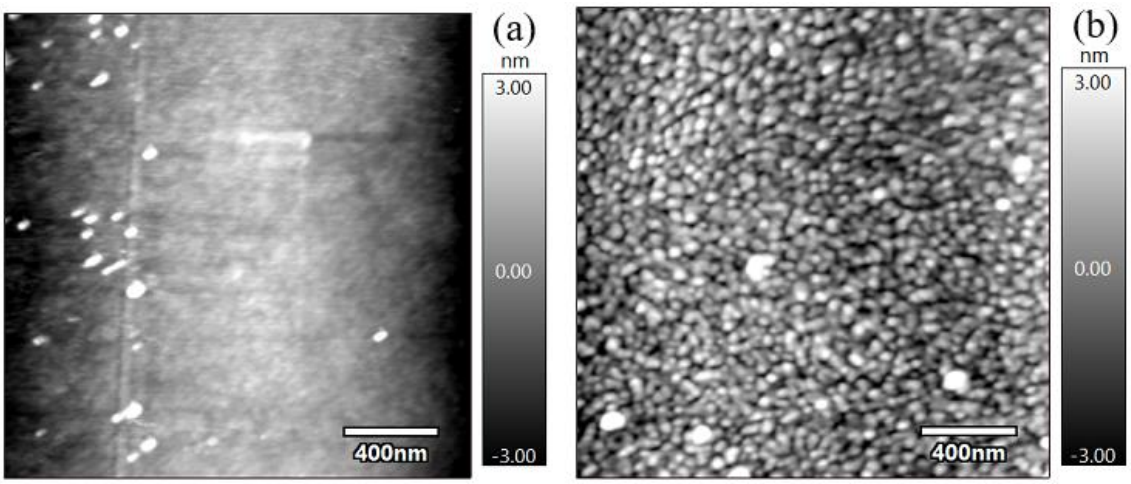


Figure 3.10. 2D profile of polymer rich region of untreated (a) and treated (b) LMPAEK/CF UD Tape by AFM.

Table 3.2 T5 and T10 temperatures for composite C_U and C_T

Composites	T5 (° C)	T10 (° C)
C_U	583.79	598.62
C_T	586.33	609.18

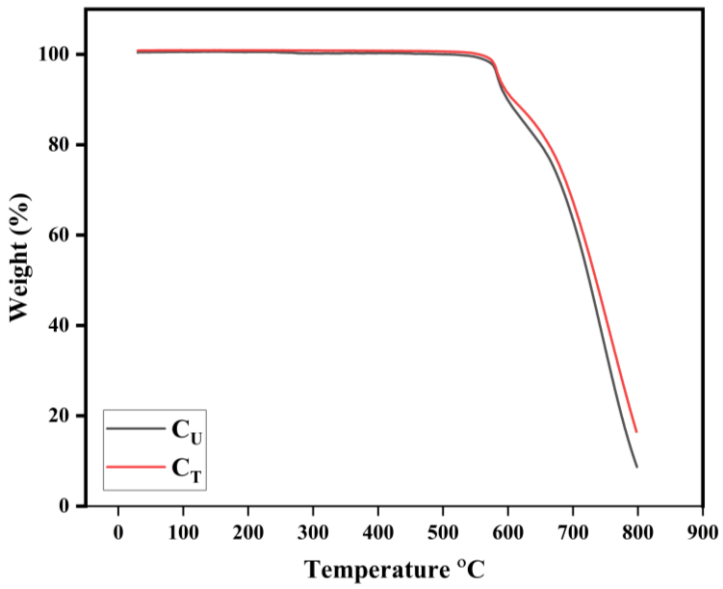


Figure 3.11. Thermogravimetric analysis for composite C_U and C_T.

an air environment. The residue percentage has been considered at 800°C, the residue percentage of C_U (8.79%) was lower than C_T (16.40%). Similar thermograms Figure 3.11 for developed composites shows that plasma treatment did not lead LMPAEK/CF tape to thermal mass degradation.

3.3.2.2 Dynamic mechanical analysis (DMA)

Figure 3.12 illustrates the variations in (a) the storage modulus (E') across a specified temperature spectrum (50-275° C), and (b) presents the tan δ values. Concurrently, Table 3 shows the storage modulus metrics at 50° C alongside the glass transition temperatures for C_U and C_T. Figure *3.12* in conjunction with Table *3.3* elucidates that the composite material C_T exhibits a superior storage modulus at 50° C when compared with C_U. This improvement in storage modulus is attributable to the enhanced interlaminar adhesion facilitated by the synergistic effect induced by chemical and physical modifications achieved through the plasma treatment employed on the LMPAEK/CF UD tape before layup using ATP system. Chemical and physical modification observed due to plasma treatment corroborates with the mechanical response of composite C_T under tensile stress, where composite C_T demonstrates a failure mode characterized by singular point fracture as opposed to the multi-layered delamination observed in C_U load-displacement behavior. Furthermore, C_T shows an elevated glass transition temperature relative to C_U indicating a marginal increment, which is an indicator of the enhanced inter-ply and interfacial interactions within C_T composites at molecules scale. Added chemical functionality (hydroxyl and carboxyl groups) by plasma treatment on LMPAEK/CF tape results in covalent and/or secondary bonding between treated LMPAEK/CF tape and substrate tape (exposing untreated side) [42]. The chemical interaction was found to be at the polymer-polymer (of two adjacent tapes) interface and not at the polymer-fiber interface. This improved molecular interaction (which is lacking in the

conventional ATP process) results in improved yet comparable mechanical performance (tensile and flexural strength and their failure modes).

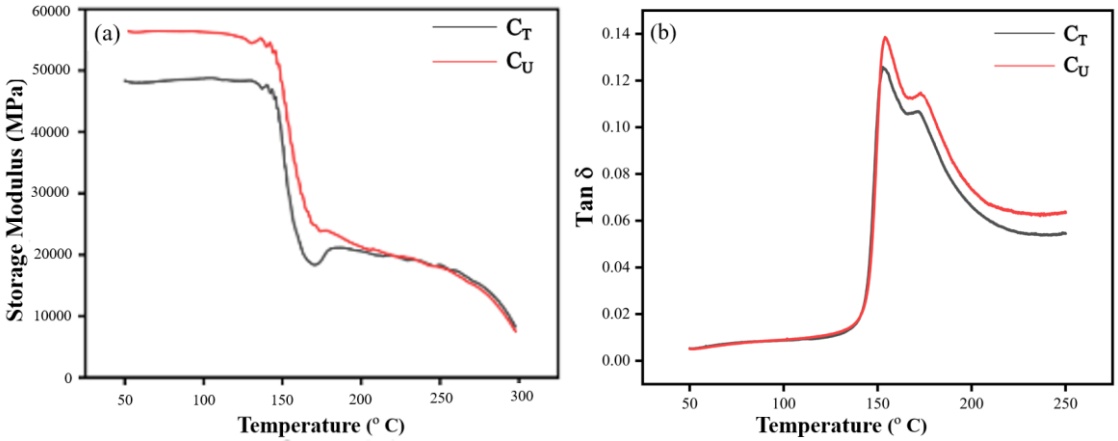


Figure 3.12 Visco-elastic performance of developed composites (a) storage modulus and (b) tan δ.

Table 3.3. Storage moduli and glass transition temperature by dynamic mechanical analysis.

Properties	**C_U**	**C_T**
E' at 50° C (GPa)	48.33	56.71
T_g (° C)	152.75	154.90

3.3.2.3 Crystallinity measurement of C_T and C_U.

The crystallinity values for C_U and C_T were 29.4 and 33.2 %. The crystallinity is directly affected by the cooling rate applied on the tape during manufacturing [88] .However, in this study both C_U and C_T were processed with identical parameters. The findings that the crystallinity of C_T was higher than C_U could be due to the effect of air plasma treatment on the LMPAEK/CF UD tape. Korycki et al [89] mentioned in their studies that the crystallinity of the materials would be affected by plasma treatment. However, achieving a higher crystallinity would increase the shear strength, tensile strength and modulus of the composites [88, 90].

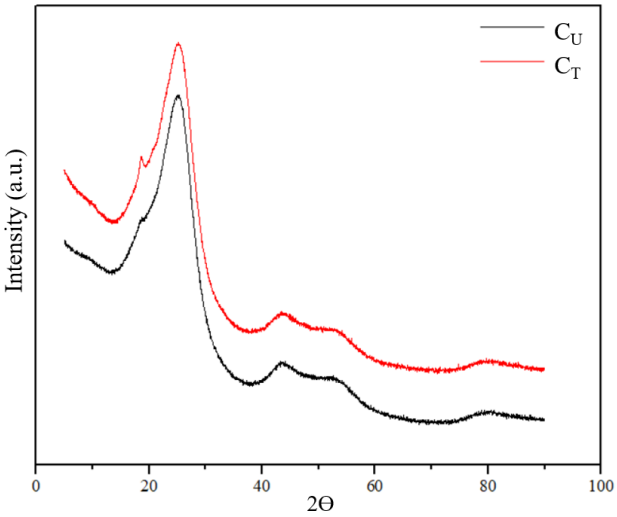


Figure 3.13. X-ray diffractogram for the developed composites C_T and C_U.

3.3.2.4 Interlaminar shear strength (ILSS)

Figure 3.14 (a) shows the ILSS behavior of the C_U and C_T. ILSS of C_T improved by ~ 18% compared to C_U. The improvement in ILSS samples can be attributed to the effect of air plasma treatment on the LMPAEK/CF UD tape. The increase of surface energy witnessed by contact angle (87° to 22°) and the increase of the surface roughness monitored by AFM, alongside the formation of hydroxyl/carboxyl group reported by FTIR, led to a higher ILSS in C_T than C_U. The air plasma treatment influenced the failure mechanism of C_T as well. Fig. 15 shows the failure analysis of the C_U and C_T tested samples. It was observed that delamination occurred in both ILSS tested samples (C_U and C_T). Figure *3.15* (a) showed that the samples extracted from the C_T exhibited a single time failure. However, the samples tested by C_U displayed a multiple crack in the sample before attaining the complete failure as shown in Figure *3.15* (a). This behavior is also reflected in Figure 3.14 (b) where C_U demonstrates non-linear behavior, with progressive failure and delamination, while C_T exhibits a single failure after reaching maximum load, characterized by a more linear response prior to attaining the maximum.

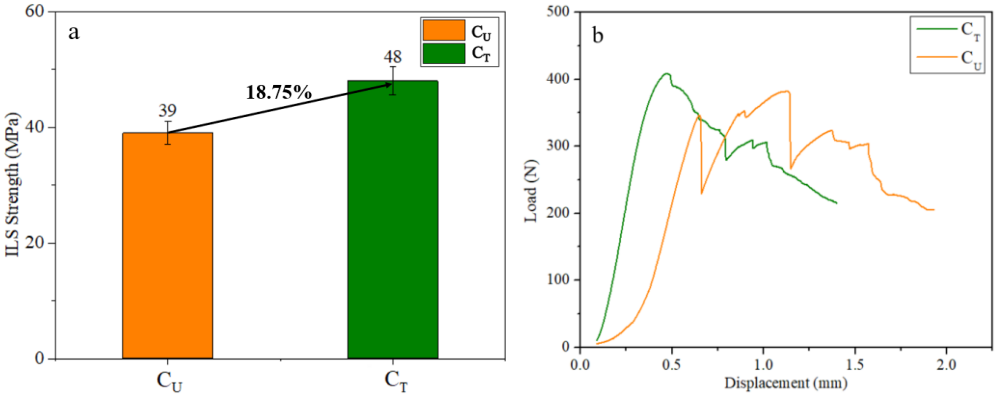


Figure 3.14 (a, b). Average interlaminar shear strength of the C_T and C_U. An improvement of 18.75% has been noticed in the C_T compared to C_U. Load vs displacement depicting the failure behavior of the ILSS samples.

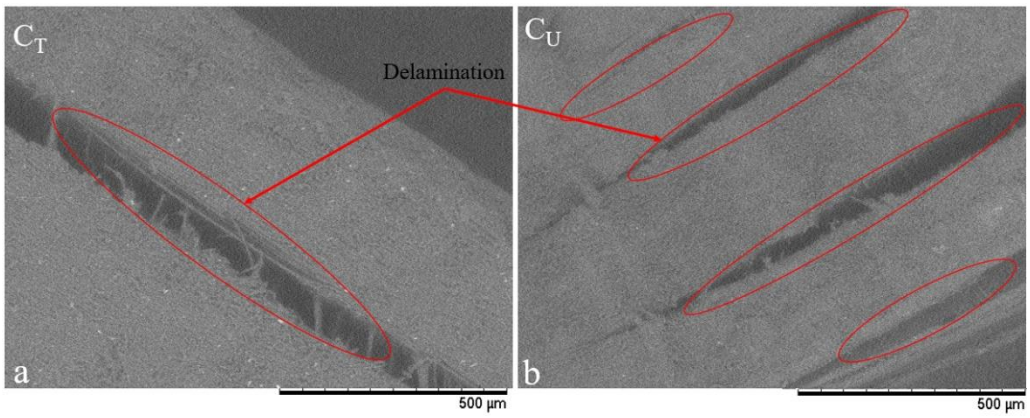


Figure 3.15 (a, b). SEM images of failed ILSS samples of C_T and C_U respectively. Delamination was observed almost between each laminate in the C_U, and just in one spot for the C_T.

3.3.2.5 Flexural Strength and Modulus

Air plasma treatment of the LMPAEK/CF UD tape affected the flexural behavior of C_T and C_U. It was noticed that the flexural strength and modulus of C_T were approximately 18% and 8.3% higher than the C_U, respectively, as shown in Figure *3.16* (a). Along with the flexural properties' enhancement, a different failure behavior between C_U and C_T samples was observed. Figure *3.17* (a, b) illustrate low-magnification optical microscopy (OM) images for the tested flexural specimens. It was perceived that the coupons extracted from the C_T

exhibited a failure in tension according with ASTM D790. The flexural tested samples of C_U displayed a delamination along the length coupons. In the case of composite C_U, the major failure mechanism includes inter-laminar delamination caused by weak inter-tape adhesion. On the other hand, post treatment-composite C_T, the dominating failure mechanism shifts to fiber breakage, matrix cracking on (tension dominated) bottom side of flexural specimen. This behavior is also evident in Figure *3.16* (b) where C_U exhibits progressive failure and delamination, while C_T demonstrates a typical failure pattern characterized by an initial linear response up to the ultimate strength, followed by a transition into a plastic deformation zone and final failure in tension. Figure *3.17* (a, b) demonstrates that plasma treatment reduces the inter-tape delamination (inferior performance) and increased interlaminar adhesion. The matrix failure and fiber breakage were observed as the dominating failure mechanism for composite C_T.

3.3.2.6 Tensile Strength and Modulus

Air plasma treatment had a positive impact on the tensile behavior of C_T. Figure 3.18 (a) shows the average tensile strength and modulus of the C_T and the C_U. An improvement of 7.6% has been noticed in the tensile strength, with 8% in the tensile modulus, as shown in

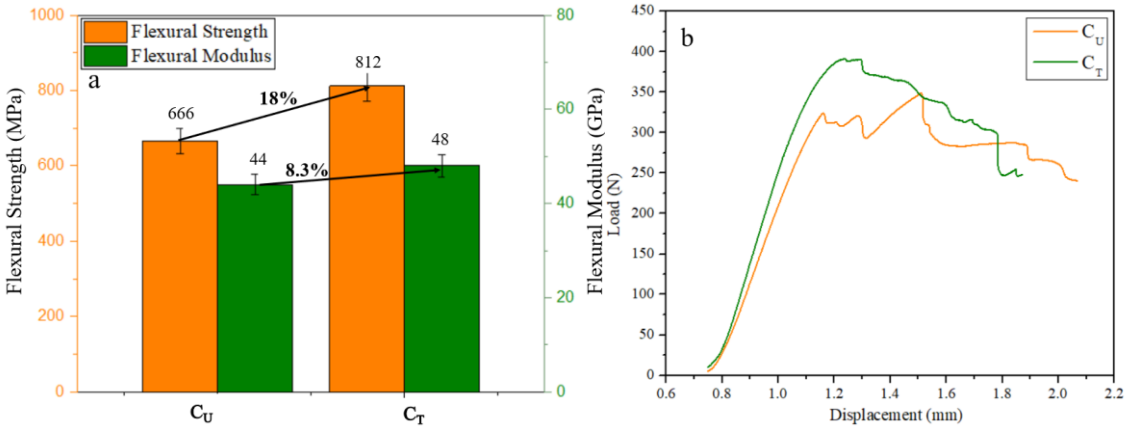


Figure 3.16 (a, b). Average flexural strength and modulus of C_T and C_U in accordance with ASTM D790. The flexural strength and modulus of C_T is 18% and 8.3% higher than C_U. Load vs displacement depicting the failure behavior of the flexural samples.

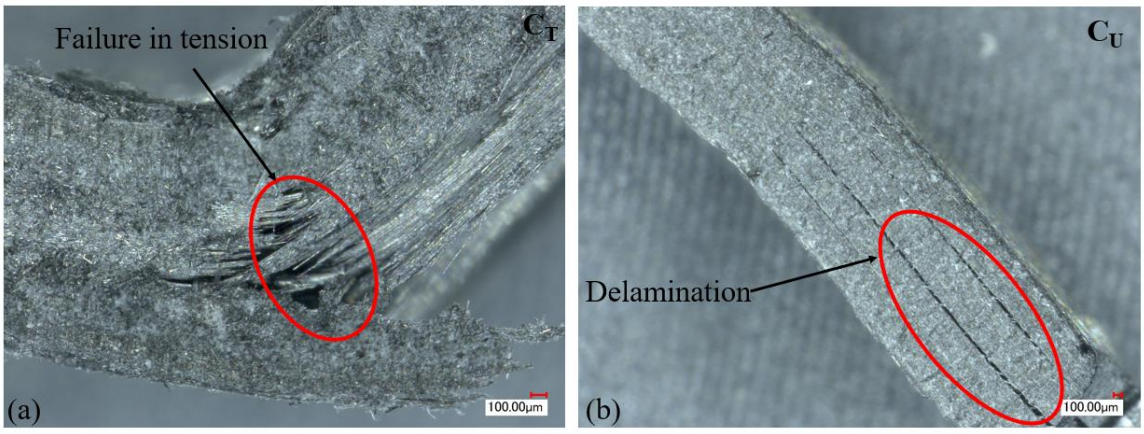


Figure 3.17 (a, b). Optical microscopy (OM) images show ASTM D790 acceptable failure behavior for the C_T, brittle failure mode in tension, and interlaminar failure mode in the C_U specimens, illustrating delamination in the samples.

Figure 3.18 (a). The load versus displacement behavior of two C_U and C_T samples have been reported as seen in Figure 3.18 (b); The failure mechanism showed that the C_U samples attained several cycles of maximum/minimum load before approaching a complete failure at ~25kN with a displacement of 18.5 mm, elucidating delamination, and fiber debonding behavior. The outcome of plasma treatment was noticed in the failure behavior of the C_T samples, the linearity, and the brittle failure, as shown in Figure 3.18 (b).

3.3.2.7 Fractography

Figure 3.19 shows the SEM micrographs for the failed samples under tensile loading. Fiber matrix debonding was the primary failure mechanism for the C_U variant. Deboned fibers and cavities of carbon fibers are marked in Figure 3.19 (a). The failure of carbon fiber was brittle in nature for both composites, which is consistent with the literature [91-93]. In the case of C_T, the absence of fiber matrix debonding, as shown in Figure 3.19 (a), depicts that the plasma treatment activates the surface by imparting chemical and physical attributes to the ATP feedstock tape, resulting in stronger bonding between CF and LMPAEK, which is reflected in mechanical properties evaluation and interlaminar shear strength performance (Figure 3.16Figure 3.17 Figure 3.18).

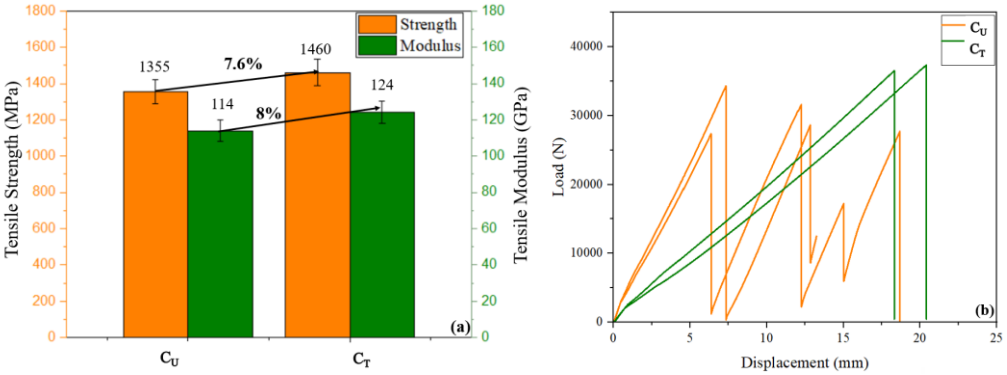


Figure 3.18 (a, b). (a) Average tensile strength and modulus for C_T and C_U. An increase of 7.6% in strength and 8% in modulus has been noticed in the C_T. (b) Shows load versus displacement, illustrating the failure behavior of the tensile samples.

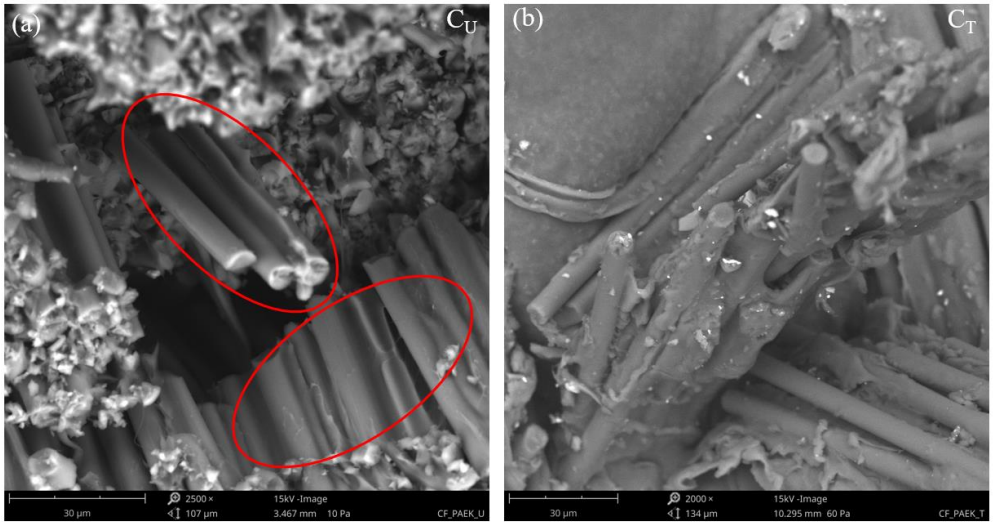


Figure 3.19 (a, b). SEM micrographs depicting failed samples during tensile test (a) CU and (b) CT.

Discussion

Different characterizations, such as contact angle measurements, FTIR, and AFM, were conducted to investigate the effect of plasma treatment on the surface of LMPAEK/CF UD tape. In the case of water contact angle measurement, it was observed that the contact angle decreased to 22° from 87°. The decrease in the contact angle indirectly suggests that the surface was more receptive to polar interactions due to the formation of chemical functional groups. The increased presence of functional groups was confirmed by FTIR spectra. These

polar groups were introduced through the reactive species (from plasma treatment) with the polymer chain, resulting in the formation of ketone group, peroxide-carbonyl, and hydroxyl groups on the PAEK, the functional groups interact with each other covalently (forming strong interaction between hydroxyl and carboxyl groups) or through Van der Waal forces such as hydrogen bonding (especially in the case of amine functional groups). These chemical interactions result in strong LMPAEK – LMPAEK interactions. Alongside chemical modification, plasma treatment imparts a certain roughness to the CF/LMPAEK surface. AFM measurements demonstrate the change in surface roughness/topology for plasma-treated LMPAEK/CF UD tape. Polymer chain scission (potential) and etching (proved through AFM experiments are the foremost mechanisms that contribute to increased surface roughness, as supported by current study and prior research. Applying controlled roughness through surface treatment can enhance the mechanical bonding between substrates (in the current study CF/LMPAEK UD tape). However, excessive roughness of both the polymer and reinforcement could lead to a decline in composite properties due to defects introduced during the surface treatment process [84, 94].

The effect of plasma treatment increased surface roughness vis-à-vis surface area for plasma treated LMPAEK/CF UD tape results in more efficient melting/softening (efficient heat transfer due to enhanced surface area) of the ATP tape compared to untreated tape. Furthermore, the chain scission, degradation of low molecular weight chains, and physical surface defects (such as surface damage at (nanoscopic/microscopic level) and contamination on LM-PAEK/CF ATP tape - majorly originated from handling of tapes) due to plasma treatment, can result in relatively low defect, improving interaction between two adjacent tapes. Beyond better homogeneity, the functional groups extend covalent bonding between tapes. These chemical and physical interactions were evident in the improvements in ILSS (18.75%), flexural strength and modulus (18% and 8.3%), and tensile strength and modulus

(7.6% and 8%) properties in C_T compared to C_U, respectively. The absence of delamination during mechanical testing captured by OM and SEM (in failed samples) demonstrated the interlaminar homogeneity for C_T.

Summary

The study investigates the integration of continuous plasma treatment in the ATP process to enhance the production of ATP-based composites with superior properties. Air plasma treatment was shown to be an effective way to enhance the in-situ consolidation of LMPAEK/CF UD tape processed through HGT on the ATP. It involves the treatment of LMPAEK/CF UD tape at a specific ATP feed rate. Key findings include:

- The air plasma treatment not only enhanced the surface characteristics of the LMPAEK/CF UD tape, leading to improved adhesion and interfacial bonding, but also demonstrated compatibility with the ATP process without introducing any defects.
- The treated tape showed a fall in water contact angle by ~65°, which corresponds to the formation of hydrophilic chemical functional groups. The change in the roughness of LMPAEK/CF UD tape corroborates to physical changes caused by plasma treatment.
- The composite C_T (developed from treated tape) shows improved tensile strength and modulus, flexural strength and modulus, and ILSS by 18.75%, 18% and 8.3% and 7.6% and 8%, respectively.
- The primary mechanisms behind these enhancements include the development of chemical functionality and subsequent covalent bonding and hydrogen bonding to the overlapping tape while processing, improved surface roughness due to plasma treatment, and the removal or degradation of surface imperfections from the LMPAEK/CF UD tape surface.

- The failure mechanism for the short beam test for ILSS was changed from inter-ply delamination to matrix cracking, fiber pull out, fiber pull out and matrix cracking.

4. CHAPTER 4

Semi-Empirical Modeling of Plasma-Induced Surface Roughness and Wettability Evolution in LM-PAEK/CF Tape

Abstract

Plasma surface modification has emerged as an effective technique to enhance adhesive performance of thermoplastic composites; However, its effects remain inadequately quantified for high-performance polymers such as LMPAEK. This study integrates experimental analysis and predictive numerical modeling to characterize the evolution of surface roughness and wettability in LMPAEK/carbon fiber (CF) composites subjected to atmospheric plasma treatment. Surface topography was quantified using AFM, and wettability changes were measured via static contact angle assessments. Results indicated a rapid initial increase in surface roughness from approximately 0.2 nm to 1.6 nm, and a significant reduction in contact angle from approximately 90° to 24° (~73% decrease), both achieving stable values within 25–30 seconds of plasma exposure. Numerical predictions demonstrated excellent agreement with experimental measurements, achieving root-mean-square errors below 5% and coefficients of determination (R^2) greater than 0.95. The developed numerical model, grounded in plasma-material interaction principles, offers predictive capabilities for optimizing plasma treatment parameters, and can be generalized to other high-performance thermoplastics. These findings provide essential quantitative insights for tailoring surface characteristics to improve adhesion in advanced composite manufacturing.

Keywords

Plasma Treatments, Surface Modifications, Atomic Force Microscopy, Contact Angle, Numerical Models

4.1 Introduction

Composite materials have become integral to aerospace and aviation industries due to their superior strength-to-weight ratios, corrosion resistance, and fatigue performance. Aerospace structures demand materials capable of enduring harsh environmental conditions, minimizing maintenance, and extending service life. These rigorous requirements drive continual advancement in composite materials. The aerospace industry's reliance on composites is reflected by the aviation composites market projection, which anticipates growth from $14.66 billion in 2018 to $29.69 billion by 2026 [95, 96]. This significant expansion underscores the critical role of advanced materials research to enhance performance and reliability.

Among composite materials, thermoplastic polymer matrix composites (PMCs) offer substantial advantages specifically beneficial for aerospace applications. Compared to traditional thermoset composites, thermoplastics demonstrate enhanced toughness, improved recyclability, shorter processing cycles, and greater compatibility with automated manufacturing methods, all of which are essential for scaling production and ensuring economic viability in aerospace applications [2, 97, 98]. In particular, LMPAEK is emerging as a leading thermoplastic due to its relatively low processing temperatures, excellent mechanical properties including high strength and stiffness, and exceptional chemical resistance. These attributes uniquely position LMPAEK as an attractive candidate for advanced aerospace components that must perform reliably under severe operational conditions Despite these advantages, a critical challenge in adopting thermoplastics like LMPAEK lies in their intrinsically low surface energy, which significantly impairs adhesion with coatings or other materials used in composite structures. Therefore, effective surface treatments are vital to enhancing bonding capabilities through increased surface roughness and improved chemical compatibility. Plasma treatment has gained prominence as an efficient, solvent-free surface modification technique, offering precise control over nanoscale

surface roughening and the introduction of polar functional groups. This method enhances surface wettability and adhesion without compromising the bulk properties of the material, making it highly suitable for aerospace composites [99-101].

Previous studies have shown that atmospheric plasma significantly improves surface energy and adhesion across various polymers [102, 103]. Noeske et al. [104] demonstrated that atmospheric plasma treatment significantly improved the adhesive bonding properties of five different polymers. Similarly, Thurston et al. [105] observed increased surface energy and wettability in polyethylene (PE) and polystyrene (PS) following atmospheric plasma treatment. Further investigations by Iqbal et al. [106] explored the effects of plasma treatment on polyetheretherketone (PEEK), carbon fiber (CF), and glass fiber (GF)-reinforced polyphenylene sulfide (PPS), revealing that surface energy increases with the introduction of polar functional groups. Their findings also indicated that atmospheric pressure plasma treatment yielded superior results compared to low-pressure plasma treatment. Moreover, recent quantitative studies by our research group revealed a rapid initial increase in surface roughness for LMPAEK/carbon fiber (CF) composites upon plasma treatment, followed by a saturation point where additional exposure yields diminishing returns and potential surface degradation risks [107].

However, a critical research gap persists regarding accurately predicting plasma-induced surface modifications specifically in high-performance thermoplastics such as LMPAEK. To address this, the current study develops an integrated analytical and numerical model that quantitatively correlates plasma treatment parameters-including duration and intensity-with resulting surface roughness and wettability changes. The developed model incorporates experimental validation through AFM and contact angle measurements, providing a rigorous predictive framework grounded in empirical data. Further advancing previous research, this study integrates material-specific parameters such as surface energy, thermal conductivity,

and density into the model formulation. This innovation enhances the model's versatility, enabling optimization of plasma processing conditions not only for LMPAEK but also for other high-performance thermoplastics, such as PPS and PEEK. As a result, the model significantly contributes to the composites manufacturing sector by enabling targeted, efficient surface treatments tailored for specific aerospace application needs.

4.2 Experimental Section

4.2.1 Material

LMPAEK/CF unidirectional (UD) tape (TC1225 LMPAEK/AS4D) was utilized of 34% resin content by weight, supplied by Toray Advanced Composites, Morgan Hill. Table 4.1shows the material properties of the LMPAEK/CF tape as received from the data sheet [108]. The density (ρ), thermal conductivity (K_{th}), and specific heat (C_p) are essential for characterizing the thermal response of the polymer during plasma exposure, which directly affects the rate and uniformity of surface activation [109]. The glass transition (T_g) and melting temperature (T_m) define the thermal limits within which structural integrity is maintained, ensuring that surface alterations remain confined to the topography without compromising bulk stability. The initial surface energy (γ_0) provides a baseline for quantifying changes in wettability, while the initial surface roughness (Ra_0) establishes a reference state against which plasma-induced morphological evolution can be assessed. Incorporating these parameters allows the model to move beyond empirical fits and toward a physics-based framework, enabling predictive accuracy across different exposure regimes and extending applicability to other high-performance thermoplastics. These specific parameters were selected based on their direct influence on thermal response, structural integrity, and surface energy dynamics during plasma treatment. Density and thermal conductivity significantly affect the uniformity of surface activation, while specific heat and glass transition temperature ensure material stability during processing.

Table 4.1.Material properties of LMPAEK/CF.

Property	Symbol	Value	Unit
Density	ρ	1.3	g/cm^3
Glass transition temperature	T_g	147	°C
Melting temperature	T_m	305	°C
Thermal conductivity	K_{th}	0.26	W/mK
Specific heat	C_p	1.1	J/gK
Initial surface energy	γ_0	14-18	mJ/m^2
Initial surface roughness	Ra_0	0.2	nm

4.2.2 Plasma Treatment Mechanism

Atmospheric plasma treatment alters the surface roughness of polymers by introducing micro and nanoscale topographical modifications. The process involves a combination of etching, oxidation, and localized energy deposition, which lead to polymer chain scission and surface restructuring as shown in Figure 4.1.

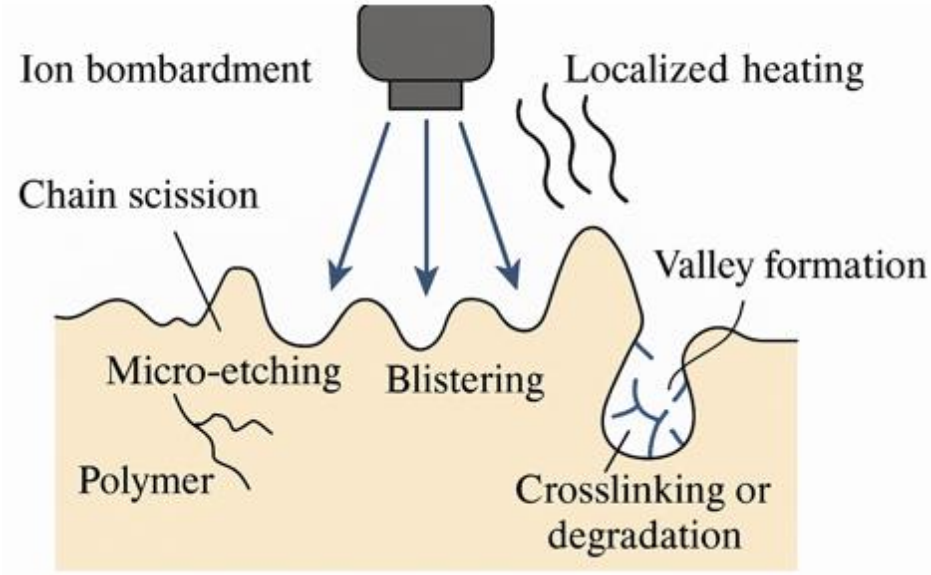


Figure 4.1.Mechanism of Surface Roughness Induced by Plasma Treatment.

Atmospheric plasma treatment was carried out using a Plasma Jet (RD1004 Rotary Jet) and a generator (FG5001 Openair-Plasma® Generator), both provided by Plasmatreat GmbH, Steinhagen, Germany. The jet was maintained in a fixed position relative to the horizontal plane, with an air flow rate of 20 L/min. The specific treatment parameters are detailed in Table *4.2*. The plasma power (P) and frequency (f) govern the energy input and excitation conditions of the plasma, directly influencing the ionization level and reactivity of the discharge. The plasma temperature (T_p), though relatively low in atmospheric systems, affects the thermal budget delivered to the surface, enabling functionalization without damaging the polymer. Electron density (N_e) and ion energy (E_i) are key indicators of plasma intensity, dictating the degree of surface activation, etching, and the introduction of functional groups. The gas composition, a mixture of 21% O_2 and 78% N_2, provides a reactive environment conducive to forming polar surface groups, while the gas flow rate (Q) ensures plasma stability and uniform treatment. Maintaining ambient pressure (F) simplifies system integration and scalability. The plasma exposure time (t) and etching rate (E_{etch}) control the kinetics of surface modification, influencing the evolution of surface roughness and wettability. Together, these parameters define the interaction regime between the plasma and polymer surface, making them essential for developing predictive models and optimizing treatment protocols for advanced thermoplastic composites. These specific plasma parameters (power, frequency, temperature, and gas flow rate) were chosen based on preliminary optimization experiments and literature benchmarks for effective surface modification without thermal degradation.

Table 4.2. A summary of Atmospheric plasma treatment parameters.

Parameter	Symbol	Value	Unit
Plasma power	P	220	W
Plasma frequency	f	50	kHz
Plasma temperature	T_p	60	°C
Electron Density	N_e	10^{14}-10^{16}	m^{-3}
Ion Energy	E_i	1-10	eV
Gas consumption	-	21% O_2, 78%N_2 (Air)	-
Gas flow rate	Q	20	L/min
Plasma pressure	F	101	kPa
Plasma exposure time	t	0-60	s
Plasma etching rate	E_{etch}	1-50	nm/min

4.2.3 Contact Angle and Atomic Force Microscopy Measurements

Contact angle measurements were performed on LM-PAEK/CF tape to evaluate its initial surface energy using a Kruss Goniometer and deionized (DI) water as the test liquid. A 2.0 µL droplet of DI water was dispensed at a controlled rate of 0.5 µL/s onto tape specimens measuring 6.35 mm by 50.8 mm. Each measurement was repeated ten times to ensure repeatability, reproducibility, and consistency. This approach enhances measurement accuracy, validates reliability, and minimizes experimental errors, thereby increasing confidence in the reported results. The initial surface energy γ_s was calculated using the Fowkes expression as shown in Eq 4.1:

$$(1 + Cos\ \theta_Y)\gamma_l = 2\sqrt{\gamma_l^d \gamma_s^d} + \sqrt{\gamma_l^p \gamma_s^p},\ \gamma_s(t) = \gamma_s^d(t) + \gamma_s^d(t) \quad \text{(Eq 4.1)}$$

where, γ_L is the surface tension of the liquid, γ_s is the surface energy of the tape, θ is the contact angle of the liquid on the solid, and $\sqrt{\gamma_s \gamma_L}$ accounts for dispersive interactions between the solid and the liquid [110].

AFM was used to quantify the surface roughness of the samples. All measurements were performed using a Cypher AFM system (Asylum Research, Oxford Instruments, Santa Barbara, USA). Silicon probes (model AC160, OLYMPUS) with a nominal tip radius of 7 nm, a spring constant of approximately 26 N/m, and a resonance frequency near 300 kHz were utilized throughout the study. Scanning was conducted in tapping mode, operating within the attractive regime to preserve surface integrity while capturing fine surface features. To prepare the data for analysis, each topography scan was processed using a 0^{th} flattening method, which removes the mean height from each individual scan line. This correction helps eliminate background tilt and enables more accurate characterization of nanoscale roughness. Imaging parameters were chosen to ensure high-resolution topographical data suitable for detailed surface evaluation.

4.3 Numerical Methodology

4.3.1 Overview

A semi-empirical plasma–surface interaction model was developed to quantify the evolution of surface roughness and contact angle in response to atmospheric plasma treatment on polymer substrates. The model integrates a semi-empirical formulation that relates treatment time, plasma power, and material-specific parameters i.e. surface energy, thermal conductivity, and glass transition behavior, to changes in surface morphology and wettability. Surface roughness is described using a logarithmic growth function corrected by a thermal-diffusion-related decay term, while contact angle is modeled through an empirical correlation with surface energy. Calibration and validation were performed using experimental data from AFM and static contact angle measurements on LM-PAEK substrates. The model accurately

captured the initial increase and subsequent saturation of surface modifications observed experimentally. While developed for LM-PAEK, the inclusion of generalized material inputs enables extension to other high-performance thermoplastics such as PPS and PEEK, facilitating optimization of plasma treatment protocols for improved interfacial bonding in advanced manufacturing techniques.

4.3.2 Surface Roughness Model

A numerical model has been developed that predicts the time-dependent roughness evolution of LMPAEK under plasma exposure. The formulation is based on empirical observations and theoretical principles that govern plasma-material interactions. To describe the roughness evolution of LMPAEK during plasma treatment, the following generalized model was proposed:

$$Ra(t) = Ra_0 + A\, log(1 + Bt) + C\, x\, \frac{\gamma_s(t)}{K_{th}.f(T_g, T_{pl})} \qquad \text{(Eq 4.2)}$$

where, Ra_0 is the initial surface roughness before plasma exposure. Parameter *A* governs the amplitude of the logarithmic roughness-growth term. It represents the contribution of early-time activation processes, including ion bombardment and radical functionalization, which drive the initial rapid increase in roughness before saturation. A higher *A* reflects a stronger effective etch/activation yield and is typically associated with higher plasma power or energy flux. *A* carries the units of roughness (nm), ensuring that the product $A\ log(1 + Bt)$ has consistent dimensionality with Ra. The parameter *B* defines the characteristic time scaling in the logarithmic roughness-growth term. Physically, it captures the rate at which surface activation saturates. Larger *B* values indicate a faster approach to the saturation regime, consistent with conditions of high plasma flux or limited thermal dissipation. Conversely, smaller *B* values represent slower kinetics due to lower flux, higher heat conduction, or increased material resistance to restructuring. *B* is dimensionless, ensuring that *Bt* is unitless inside the logarithm. The parameter *C* scales the coupling between surface energy and

roughness evolution. Unlike the previous constant form, this contribution varies in time through $\gamma_s(t)$ which is obtained from Owens-Wendt analysis. The term weighted by *C* accounts for the tendency of higher surface energy to increase restructuring under plasma bombardment, while higher thermal conductivity K_{th} and reduced chain mobility below the glass-transition temperature, (T_g) act to suppress this effect. *C* is a dimensioned scaling factor, chosen so that the full term contributes in nanometers, and is determined by nonlinear regression of the experimental data. T_{pl} is the plasma temperature.

$$f(T_g, T_{pl}) = 1 + e^{-\alpha(T_{pl}-T_g)} \quad \text{(Eq 4.3)}$$

The coefficient α appears in the exponential damping factor in Eq 4.3. It regulates the sensitivity of surface mobility to the difference between the near-surface plasma temperature T_{pl} and the glass-transition temperature T_g. A larger α yields a stronger dependence of roughness development on T_{pl} - T_g, whereas smaller values correspond to weaker temperature sensitivity. α\alphaα is dimensionless by construction, and its fitted value provides a material-specific measure of how thermal activation interacts with plasma exposure to stabilize or suppress roughness growth [111].

The numerical implementation of the roughness model was carried out using a time-stepping approach as shown in Figure 4.2. The roughness Ra(t) is computed iteratively over discrete time steps based on plasma exposure duration. Empirical constants (A, B, and C) were initially derived from preliminary AFM measurements and sensitivity analysis. Parameter A is primarily influenced by plasma ion energy and etching rate, B by thermal dissipation properties (thermal conductivity, specific heat), and C by surface energy and chain mobility of the polymer. The computed roughness values were then used to generate 2-D AFM-like roughness maps, allowing for direct comparison with experimentally observed surface morphology. The numerical model was implemented using Python with a discrete-time Euler

approach for iterative calculations. Model convergence was confirmed by ensuring changes between successive iterations were below 0.001 nm, typically achieved within 100 iterations.

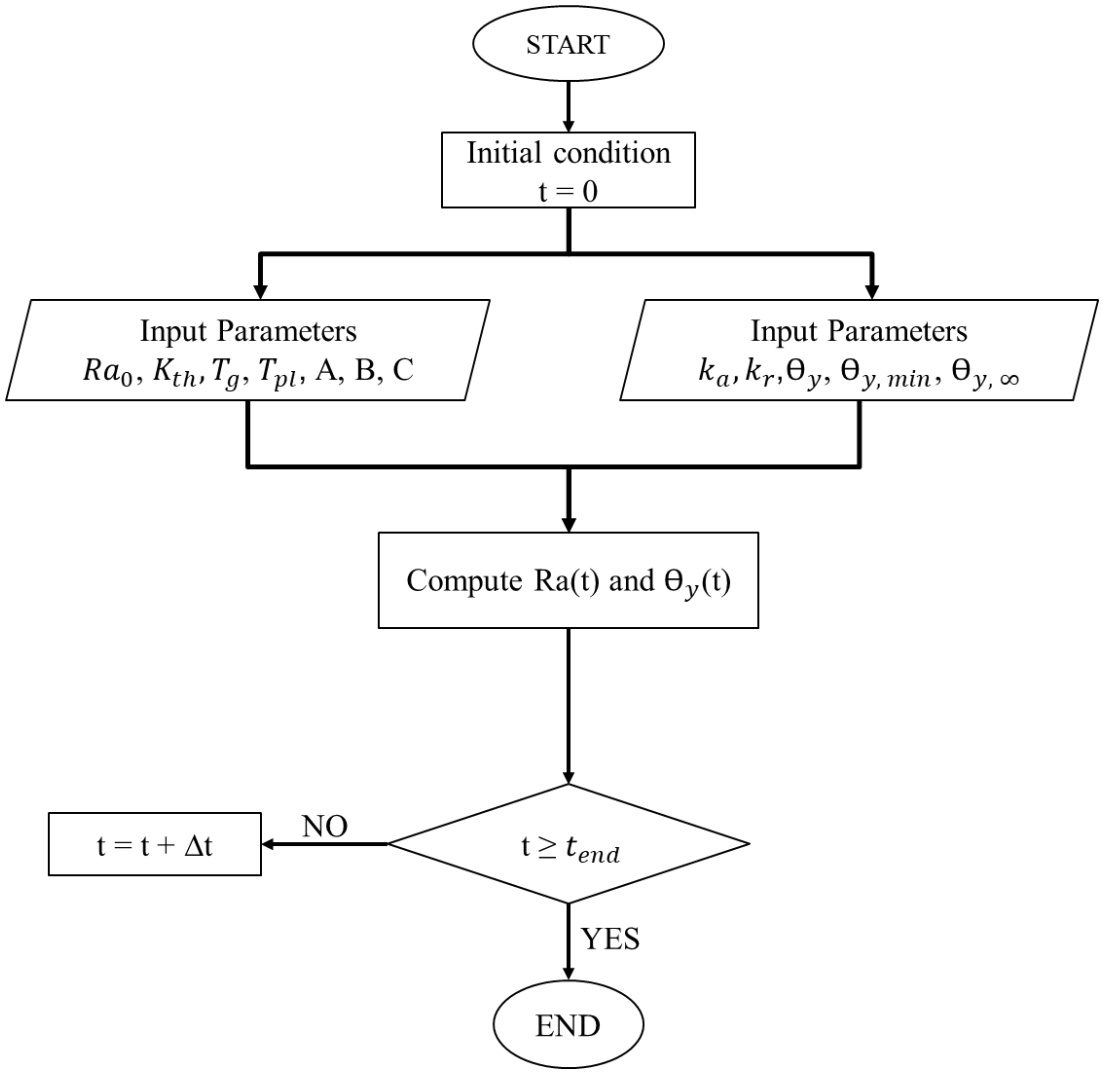


Figure 4.2. Flowchart of the numerical algorithm used to model plasma-induced surface roughness and contact evolution in LMPAEK.

The process initializes with experimental surface roughness, contact angle and iteratively computes roughness at each step using material properties and plasma exposure parameters.

4.3.3 Contact Angle Model

Surface wettability is a key factor in determining adhesion and bonding performance in plasma-treated polymers. The contact angle, which quantifies the wettability of a material, evolves dynamically during plasma exposure due to the introduction of polar functional

groups and subsequent surface reformation [112]. This section presents a numerical model that predicts the time-dependent evolution of the contact angle of LMPAEK/CF under atmospheric plasma treatment, incorporating experimentally observed trends and theoretical principles.

Several empirical and theoretical models have been proposed to describe contact angle evolution during plasma treatment [113, 114]. While simple exponential decay models capture the initial drop in contact angle, they fail to account for long-term stabilization and recovery effects. In this study, we use a dual-component model that accounts for both the rapid initial decrease and the subsequent stabilization phase, ensuring consistency with experimental observations. The evolution of the contact angle during plasma treatment is modeled as:

$$\theta_Y(t) = -k_a(\theta_Y - \theta_{Y,min}) + kr(\theta_{Y,\infty} - \theta_Y) \quad \text{(Eq 4.4)}$$

Which integrates to

$$\theta_Y(t) = \theta_Y^{ss} + [\theta_Y(0) - \theta_Y^{ss}]e^{-(k_a+k_r)t} \quad \text{(Eq 4.5)}$$

With the steady-state value

$$\theta_Y^{ss} = \frac{k_a\theta_{Y,min} + k_r\theta_{Y,\infty}}{k_a + k_r} \quad \text{(Eq 4.6)}$$

Here, k_a and $k_r$are the activation and recovery rate constants, $\theta_{Y,min}$ is the minimum angle reached during plasma activation, and $\theta_{Y,\infty}$ is the long-term asymptote representing recovery or hydrophobic relaxation. k_a (activation rate constant) governs how rapidly the contact angle decreases during plasma activation as polar groups are introduced and the surface becomes more hydrophilic. Larger $k_a$values correspond to faster activation kinetics. Units: s^{-1}. k_r (recovery rate constant) represents the rate of hydrophobic recovery, i.e., how quickly the surface relaxes toward its long-term equilibrium state through reorientation or migration

of functional groups. Larger k_r implies faster recovery. Units: s^{-1}. θ_Y^{ss} is the steady-state solution of Equation (6), balancing the competing effects of activation and recovery.

$$\cos\theta_*(t) = r(t)\cos\theta_Y(t) \quad \text{(Eq 4.7)}$$

Equation (7) shows the topography-wettability coupling. The apparent water contact angle measured on a rough surface, θ_*, is related to the intrinsic Young's angle θ_Y, through the Wenzel solution. Here, *r(t)* is the roughness ratio, defined as the ratio of actual to projected surface area. Instead of estimating the *r* from a single roughness parameter such as *Ra, r(t)* is obtained from the power spectral density (PSD) of the AFM surface, via a mapping function ϕ[PSD(t)]:

$$r(t) = 1 + \beta\phi[\mathrm{PSD(t)}] \quad \text{(Eq 4.8)}$$

where, β is a fitted scaling factor. This approach ensures that the apparent wettability is coupled directly to the evolving nanoscale topography, rather than relying on a single average roughness value.

The first term models the initial exponential drop in contact angle due to the immediate incorporation of oxygen functional groups. The second term accounts for long-term stabilization effects, including hydrophobic recovery, which is dependent on polymer chain mobility and surface restructuring. The equation has been computed as shown in Figure 4.2. This approach ensures that the predicted contact angle evolution remains consistent with the experimentally observed trends for LMPAEK. The accuracy and reliability of the model are further evaluated in Section 3, where numerical predictions are compared with experimental data.

4.4 Numerical Methodology

Figure 4.3 illustrates that the model captures a sharp increase in roughness from approximately 0.2 nm (untreated) to 0.8 - 1.0 nm at 5 seconds, based on the parameters (Table *4.1* & Table *4.2*). The developed model accurately predicts the evolution of surface

roughness and contact angle in response to plasma treatment, aligning well with the hypothesized surface behavior of LMPAEK. This initial rise corresponds to rapid surface activation caused by energetic ion bombardment, leading to chain scission, crosslinking, and micro-etching, mechanisms widely reported in plasma-treated high-performance polymers [115].

Between 5 and 10 seconds, the roughness increases further to approximately 1.3 - 1.4 nm, suggesting continued nanostructure development and enhanced surface texturing. However, beyond 20 - 25 seconds, the model shows a clear stabilization trend, with roughness approaching a saturation value near 1.6 - 1.7 nm by 55 seconds. This saturation is attributed to the re-exposure of previously treated areas due to the limited spatial penetration of atmospheric plasma and the finite diffusion depth of reactive species [116]. Such self-limiting behavior has been experimentally observed in polymer systems, where prolonged exposure leads to morphological changes (e.g., surface densification or collapse of etched features) without significant increases in mean roughness values.

This surface evolution directly impacts wettability. The model predicts a sharp drop in contact angle from ~90° to ~24° within the first 10 seconds of treatment. This is attributed to both the increased surface area and the incorporation of oxygen-containing functional groups such as hydroxyl, carbonyl, and carboxyl moieties [117, 118]. These groups enhance polar interactions and hydrogen bonding with water, significantly lowering the surface energy and thereby increasing hydrophilicity.

As the roughness plateaus beyond 20 – 25 seconds, the contact angle correspondingly rises slightly and stabilizes around ~32°, indicating a quasi-equilibrium. This is consistent with reports that prolonged plasma exposure may lead to competing effects such as polymer chain reorientation, crosslinking-induced stiffness, or partial loss of functional groups via desorption or recombination reactions [119, 120]. Thus, both roughness and wettability

models in this study are intrinsically coupled and physically grounded, reinforcing the model's predictive capability. The results not only validate the hypothesized dynamic phases-initial surface activation, morphological growth, and stabilization, but also offer a quantitative tool for tailoring plasma parameters to optimize adhesion-relevant surface characteristics in LMPAEK and other engineering-grade thermoplastics.

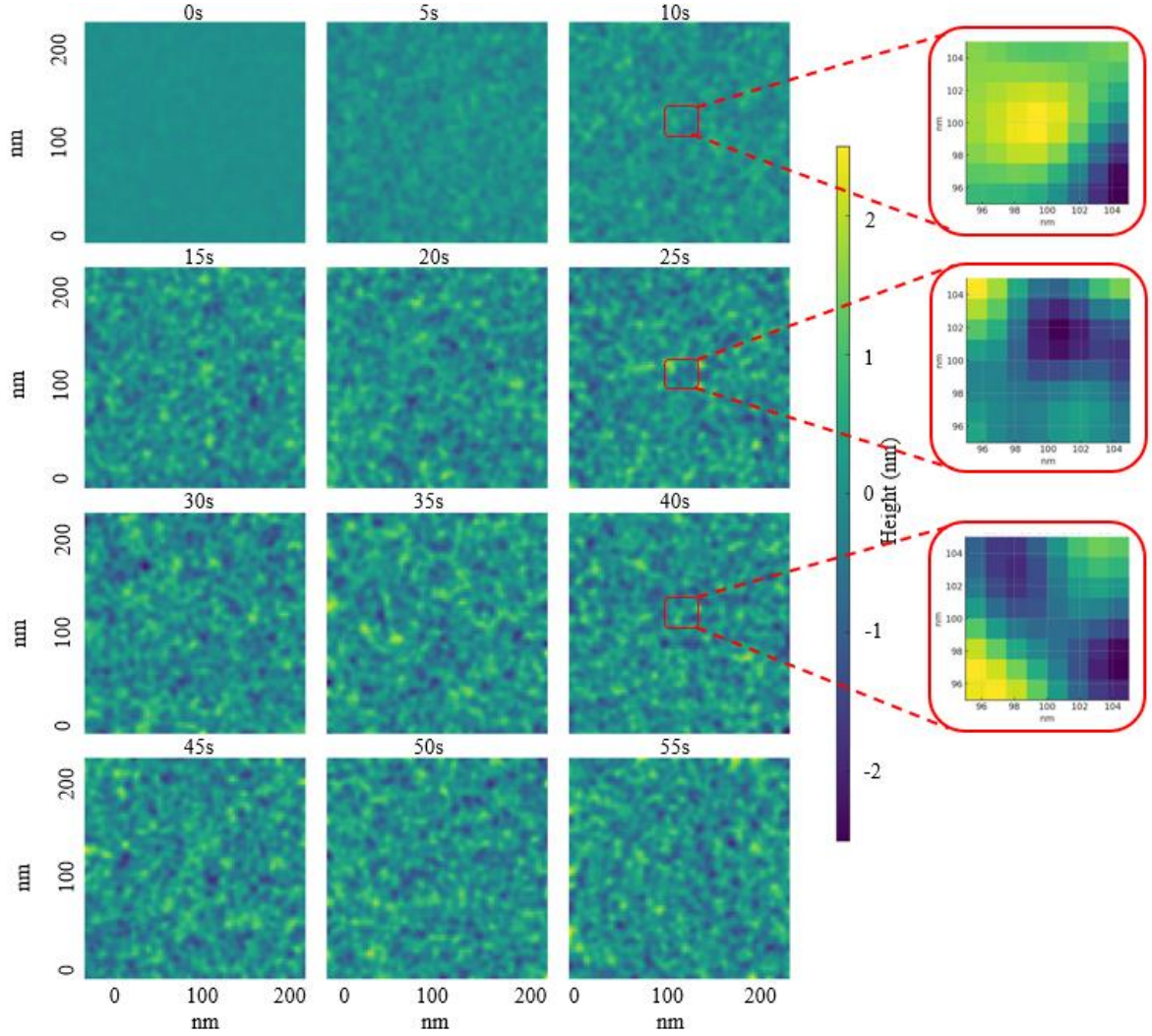


Figure 4.3. Surface roughness evolution over time under constant intensity of plasma exposure. From Top left to right, exposure time of 0s, 5s, 10s, etc.

The surface roughness apparently increases until around 20s, then it reaches to a saturation point, where the surface roughness changes but within the same roughness range.

4.4.1 Atomic Force Microscopy Model

Figure *4.4* presents the evolution of surface roughness (Ra) as a function of plasma treatment duration, highlighting both numerical predictions and experimental observations. Surface roughness outputs from the numerical model are compared with AFM measurements across varying plasma exposure times to evaluate accuracy and predictive performance. The numerical curve was generated using Eq 4.2, employing the parameters listed in *Table 4.1* and *Table 4.2* and by assuming empirical constants A=1 nm, B=3 s^{-1}, and C=0.5 $nms^{-1}k^{-1}m$. Each constant in the model has a direct physical interpretation: A reflects how fast roughness builds up based on plasma energy delivery, B reflects how quickly the material stabilizes due to thermal and mechanical properties, and C reflects the material's surface energy and mobility controlling final roughness amplification. These values were determined through a curve fitting approach designed to closely match experimental observations while preserving clear physical meaning tied to underlying plasma-material interaction parameters.

Specifically, constant A, which controls the logarithmic roughness growth rate, is proportional to the plasma-material interaction intensity and can be related to the product of ion flux, ion energy, etching yield, i.e., ($A \propto \frac{\Phi_i E_i Y}{\rho}$). Constant B, which governs the saturation speed of the response, reflects the surface's capacity to dissipate energy and stabilize thermally, and is inversely related to the product of specific heat, thermal conductivity, and glass transition temperature: $B \propto \frac{K_{th}}{C_p T_g}$. Constant C, which modulates the influence of plasma parameters on roughness evolution, incorporates the effects of surface energy and surface mobility and can be approximated as $C \propto \gamma/\mu$ where μ is the effective surface viscosity or chain mobility.

While these constants were empirically adjusted, their magnitudes are consistent with the material's known behavior under plasma exposure. The resulting numerical predictions

showed a deviation of only ~4% from the experimental AFM roughness values, further confirming the robustness and physical consistency of the model.

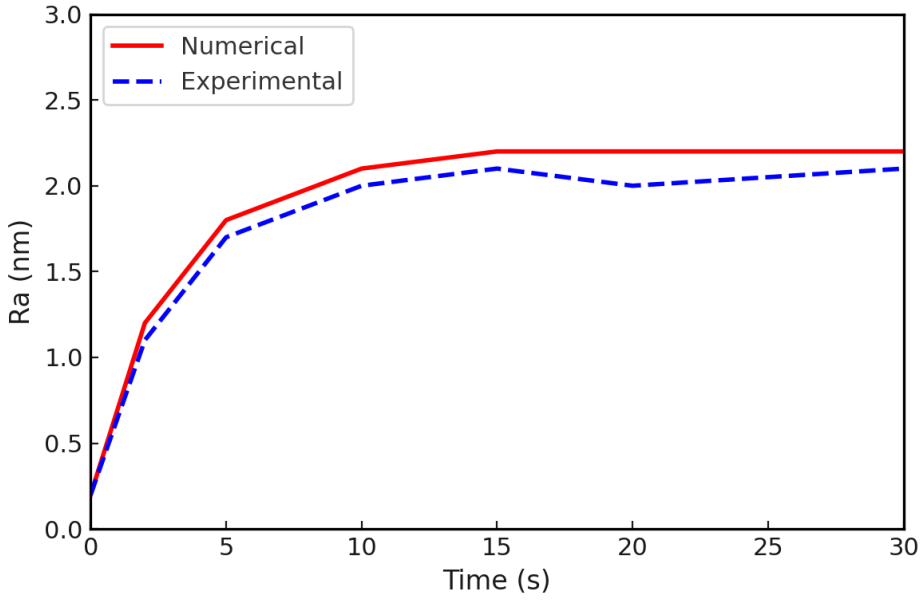


Figure 4.4. Surface roughness evolution as predicted by numerical modeling and validated by experimental AFM data, clearly illustrating rapid initial changes and subsequent stabilization phases critical for optimal plasma treatment time selection.

The numerical model captures the rapid initial increase in roughness, which is observed experimentally, followed by a stabilization phase. The logarithmic dependency of the roughness evolution equation successfully describes the saturation trend seen in AFM measurements. However, minor deviations between the model and experimental data at longer exposure times suggest that additional surface mechanisms, i.e. plasma-induced crosslinking or nanostructure collapse, may influence the final roughness state [121].

In addition to pointwise roughness measurements, numerical simulations generated 2-D roughness maps to visually compare predicted and experimental surface topographies. Figure 4.5 presents side-by-side comparisons of AFM-measured roughness distributions and simulated roughness profiles for selected plasma exposure times.

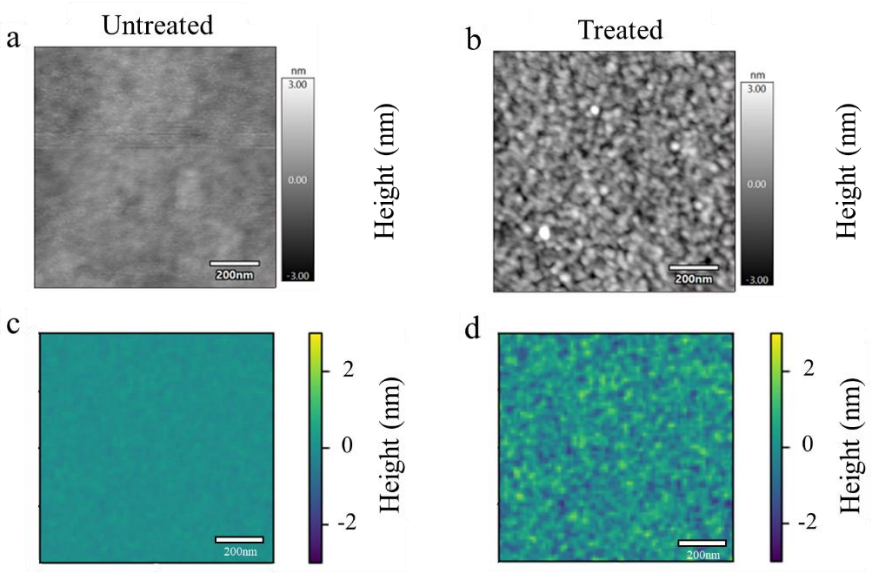


Figure 4.5. 2-D surface topography of the untreated LMPAEK/CF tape (0s) and treated (5s). Comparison between AFM-measured roughness distributions (a, b), and numerically simulated roughness profiles (c, d) for untreated (0s) and plasma-treated (5s) LMPAEK/CF surfaces. The numerical model effectively captures the increase in surface roughness observed experimentally after plasma treatment, demonstrating strong qualitative agreement. In the untreated state, both experimental and numerical roughness maps exhibit a relatively smooth surface with minimal height variations, confirming the model's ability to capture the baseline roughness. After plasma treatment, both AFM and numerical simulations show a significant increase in surface roughness, indicating that the model successfully replicates the physical modifications induced by plasma exposure.

In the experimental AFM maps, the untreated surface (0s) exhibits a relatively smooth topology with visible directional features, likely associated with the material's original surface texture as received. After 5 seconds of plasma treatment, the surface undergoes significant morphological changes, with the emergence of nanostructured features, increased peak-to-valley variations, and enhanced roughness, indicating material restructuring due to plasma exposure.

In the numerical simulations, a similar trend is observed. The untreated surface shows a controlled undulating profile with moderate roughness. After plasma treatment, the simulated roughness profile captures the transition to a more chaotic and irregular structure, mimicking the increase in peak intensity and spatial distribution observed in the experimental data as shown Figure 4.6. The numerical model effectively predicts the overall increase in roughness and the transition to a more irregular morphology, but localized variations in peak sharpness and spatial frequency may stem from differences in energy absorption, plasma exposure uniformity, or inherent surface heterogeneities.

While the overall trend aligns well between experimental and numerical data, some discrepancies may exist in localized roughness variations. These differences could stem from factors such as microscale surface heterogeneities, plasma energy distribution inconsistencies, or model assumptions that simplify complex surface interactions. Nonetheless, the close agreement between experimental measurements and numerical predictions suggests that the model provides a reliable representation of surface roughness evolution and can be used to optimize plasma treatment parameters for desired surface characteristics.

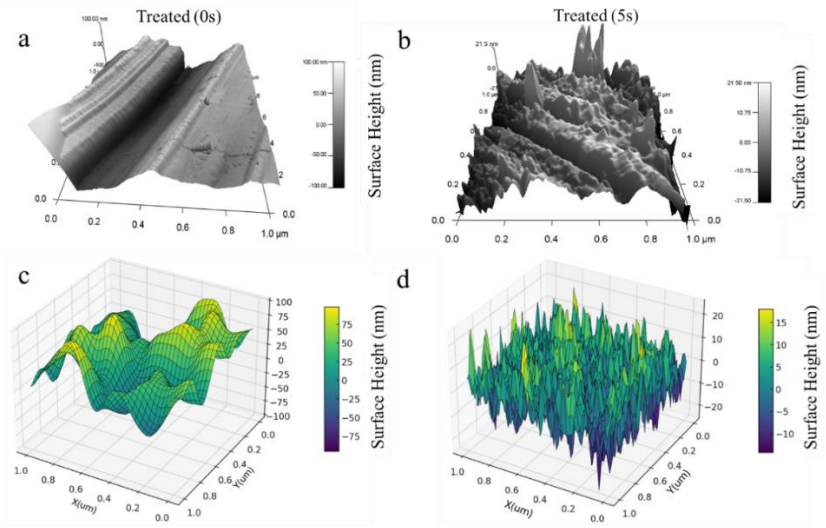


Figure 4.6.The 3-D surface roughness comparison between experimental (a, b) and numerical (c, d) models provides a more detailed insight into the spatial variations induced by plasma treatment.

The comparison between experimental and numerical surface morphologies in Figure 4.7 shows good agreement for both untreated and treated conditions. For the untreated surface Figure 4.7 (a) the mean absolute error (MAE) and mean signed error (MSE) were approximately 4.62% and 2.29%, respectively, indicating that the numerical model captures the key features of the experimental topography with relatively low deviation.

In the treated surface Figure 4.7 (b) the MAE and MSE further decreased to approximately 3.69% and 2.12%, respectively, suggesting improved predictive accuracy after treatment. This reduction in error can be attributed to the smoothing and homogenizing effects induced by the treatment process (e.g., plasma exposure or chemical modification), which reduce nanoscale surface irregularities and variations in surface energy. As a result, the treated surface exhibits less local height fluctuation and a more stable energy landscape, making the morphology both geometrically and chemically easier to replicate numerically.

From a physical standpoint, untreated surfaces often exhibit a broader distribution of asperities and higher-frequency roughness components due to intrinsic material heterogeneity and fabrication imperfections. These complex local geometries introduce noise that increases the difficulty of accurate numerical reproduction. In contrast, surface treatments suppress high-frequency features, homogenize chemical composition, and stabilize surface energy, thereby simplifying the numerical approximation process and enhancing agreement with experimental measurements.

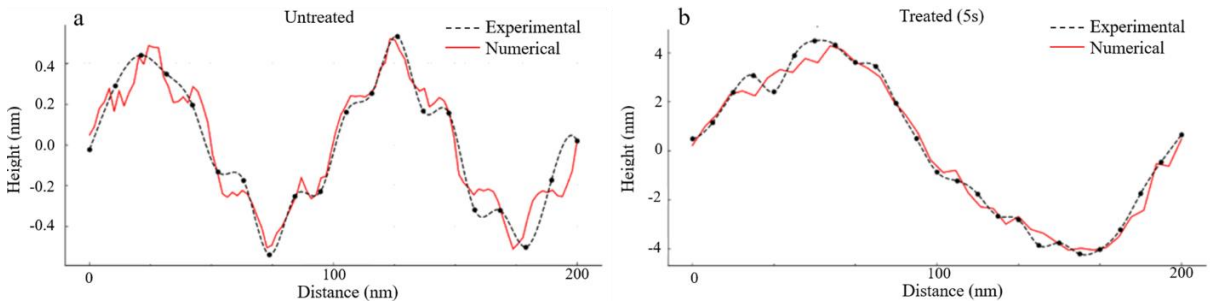


Figure 4.7.Comparison of experimental and numerical surface profiles for untreated and treated conditions.

For the untreated surface, the MAE and MSE are approximately 4.62% and 2.29%, respectively, while for the treated surface, they decrease to approximately 3.69% and 2.12%, indicating improved numerical prediction accuracy after treatment.

4.4.2 Contact Angle Model

The experimental contact angle data clearly demonstrates the time-dependent impact of plasma treatment on LMPAEK surfaces. Initially, the contact angle is high (~90°), indicating a hydrophobic surface with minimal polar functionality. Within the first 15 seconds, a sharp drop to ~22° occurs, signifying a substantial increase in wettability. Atmospheric plasma treatment enhances surface wettability by introducing oxygen-containing functional groups such as hydroxyl (-OH), carboxyl (-COOH), and carbonyl (-C=O) onto the polymer surface [27]. This process reduces the material's intrinsic hydrophobicity, leading to a sharp decrease in contact angle. However, over time, hydrophobic recovery may occur due to surface reorganization, where low-energy polymer chains migrate to the surface, partially reversing the wettability improvement. This rapid transition is attributed to the incorporation of oxygen-containing functional groups and the removal of hydrocarbon contaminants, both of which enhance surface polarity. After reaching this highly wettable state, the contact angle exhibits a mild rebound, stabilizing around 35°. This behavior is consistent with dynamic surface reorganization processes, where surface functional groups reorient or partially recover under continued plasma exposure, leading to a slight decrease in surface polarity.

This trend confirms the effectiveness of short plasma exposures (~10–20 seconds) in maximizing surface wettability for LMPAEK, while also highlighting the onset of diminishing returns or partial reversibility with prolonged treatment. The model successfully replicates the nonlinear behavior observed experimentally, capturing the steep initial decline, the overshoot near 20 seconds, and the subsequent stabilization phase as shown in Figure 4.8. Its ability to mimic the rebound effect further demonstrates sensitivity to surface kinetics,

including functional group saturation and reorganization effects. Numerical predictions show excellent agreement with experimental measurements, with a standard deviation of approximately 3% relative to experimental contact angle values across all time points. Minor deviations are attributed to experimental variability, limitations in temporal resolution, and potential surface inhomogeneities not explicitly represented in the model.

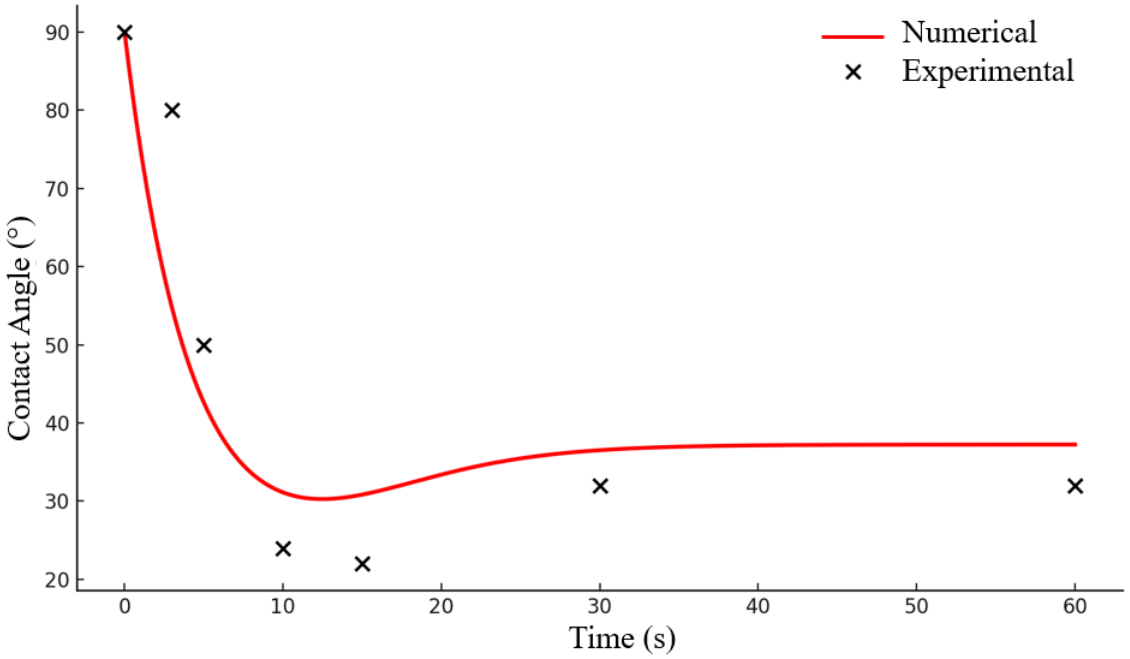


Figure 4.8 illustrates the predicted and measured contact angles over plasma exposure time. The dual-term model, incorporating both exponential decay and hyperbolic tangent stabilization, accurately describes the rapid initial decrease in contact angle due to plasma-induced functionalization, followed by a gradual stabilization phase.

To quantify model accuracy, RMSE and coefficient of determination (R^2) were computed for both roughness and contact angle predictions. The RMSE values indicate a high degree of agreement between model predictions and experimental data, with (R^2) values exceeding 0.95 for both roughness and contact angle evolution trends. However, sensitivity analysis revealed that minor variations in plasma power and temperature significantly impact the model output,

suggesting that more precise experimental control over plasma conditions may further enhance predictive accuracy.

At this stage, the model can predict the surface roughness and contact angle of polymer surfaces as functions of plasma treatment parameters. This predictive capability significantly reduces the reliance on extensive experimental campaigns, including labor-intensive and costly techniques such as AFM. Moreover, the model enables systematic evaluation of key processing variables, such as treatment duration, plasma intensity, and polymer chemistry, which are often difficult to isolate experimentally due to the need for repeated sample preparation and analysis.

By providing reliable predictions of interfacial surface properties, the model offers valuable insights into factors influencing interlaminar strength and facilitates the optimization of plasma parameters tailored to specific material systems. This predictive capability ultimately supports more efficient surface engineering and accelerates development in advanced thermoplastic manufacturing.

4.5 Discussions

This study highlights the effectiveness of atmospheric plasma treatment in modifying the surface morphology and wettability of LMPAEK/CF composites. The numerical models developed for roughness and contact angle evolution successfully capture the physical mechanisms involved in plasma–polymer interactions. The roughness model reflects the rapid formation of nanoscale features due to ion bombardment and surface etching, followed by a stabilization phase as the surface saturates. Similarly, the wettability model accurately describes the transition from hydrophobic to hydrophilic behavior, consistent with the incorporation of polar functional groups and subsequent molecular rearrangement.

The close agreement between model predictions and experimental measurements, with root mean square errors below 5% and coefficients of determination exceeding 0.95, supports the

robustness of the modeling framework. The model performs particularly well under treated conditions, where plasma exposure leads to more uniform surface characteristics. Beyond reproducing observed trends, the model offers insights into the combined morphological and chemical modifications induced by plasma treatment.

The current framework assumes spatially uniform plasma exposure and does not explicitly account for variations in local energy distribution, potential crosslinking effects, or subsurface alterations. Additionally, the wettability model includes chemical functionalization in a qualitative sense but lacks direct input from quantitative chemical data, such as X-ray photoelectron spectroscopy, which would enhance its predictive accuracy. Despite these limitations, the model substantially reduces the need for extensive experimental work and enables efficient parametric exploration of processing conditions. Its physics-based structure ensures interpretability and scientific grounding, although empirical calibration remains necessary when applying it to new materials or treatment settings.

Summary and Future Work

This study introduced and validated a predictive framework for modeling plasma-induced surface modification in LMPAEK/CF composites. The model successfully captures key aspects of surface evolution, including nanoscale roughening, saturation behavior, and dynamic wettability transitions, under varying plasma exposure conditions. Mean absolute errors remained below 5%, and contact angle predictions exhibited low variability, confirming the model's ability to replicate experimental observations.

By minimizing reliance on characterization techniques such as AFM and contact angle goniometry, the model offers a practical tool for optimizing plasma treatment parameters. Its foundation in material-specific thermal and surface properties enhances its relevance for a range of high-performance thermoplastics, including PPS and PEEK.

Future work will focus on improving the chemical specificity of the model and expanding its applicability to different plasma chemistries and treatment scenarios. Additionally, integrating machine learning techniques may enhance the model's adaptability by uncovering nonlinear relationships, automating parameter calibration, and supporting data-driven optimization. This hybrid approach, combining physics-based insight with AI-driven flexibility, holds promise for creating scalable and intelligent tools for surface engineering across diverse polymer systems.

References

1. Reis, J.P., M. de Moura, and S. Samborski, *Thermoplastic composites and their promising applications in joining and repair composites structures: A review.* Materials, 2020. **13**(24): p. 5832.
2. Ozturk, F., M. Cobanoglu, and R.E. Ece, *Recent advancements in thermoplastic composite materials in aerospace industry.* Journal of Thermoplastic Composite Materials, 2024. **37**(9): p. 3084-3116.
3. Ning, H., et al., *A review of long fibre thermoplastic (LFT) composites [A review of long fibre-reinforced thermoplastic of long fibre thermoplastic (LFT) composites].* International Materials Reviews, 2019. **64**(1).
4. Mohammadkhani, P., *Anisotropic mechanical material investigation on moisture and strain rate sensitivity of direct compounded compression moulded Glass/PA6 LFTs*. 2023, University of Windsor (Canada).
5. Thomason, J. and M. Vlug, *Influence of fibre length and concentration on the properties of glass fibre-reinforced polypropylene: 4. Impact properties.* Composites Part A: Applied Science and Manufacturing, 1997. **28**(3): p. 277-288.
6. Ning, H., et al., *A review of Long fibre thermoplastic (LFT) composites.* International Materials Reviews, 2020. **65**(3): p. 164-188.
7. Hao, X., et al., *Effects of fiber geometry and orientation distribution on the anisotropy of mechanical properties, creep behavior, and thermal expansion of natural fiber/HDPE composites.* Composites Part B: Engineering, 2020. **185**: p. 107778.
8. Carosella, S., et al., *A short review on recent advances in automated fiber placement and filament winding technologies.* Composites Part B: Engineering, 2024: p. 111843.
9. Alramsi, R.M.A.A., *Optimization of Automated Fiber/Tape Placement technology for high-performance thermoplastic composites*. 2024, Khalifa University of Science.

10. Domm, M., J. Schlimbach, and P. Mitschang, *Characterization method for continuous fiber reinforced thermoplastic strands.* Journal of Thermoplastic Composite Materials, 2021. **34**(3): p. 328-352.
11. Alwekar, S., et al., *Melt extruded versus extrusion compression molded glass-polypropylene long fiber thermoplastic composites.* Composites Part A: Applied Science and Manufacturing, 2021. **144**: p. 106349.
12. Weber, C., et al., *A novel, new direct injection technology for in-line compounding and molding of LFT automotive structures*. 2002, SAE Technical Paper.
13. Brasington, A., et al., *Automated fiber placement: A review of history, current technologies, and future paths forward.* Composites Part C: Open Access, 2021. **6**: p. 100182.
14. Kukwi, T., et al., *Continuous Improvement in Composite Manufacturing: A Review of Automated Fiber Placement Process Evolution and Future Research Prospects.* Applied Composite Materials, 2025: p. 1-48.
15. Research, C. *Automated Fiber Placements and Automated Tape Laying Machines Market – Growth, Share, Opportunities & Competitive Analysis, 2024–2032*. 2024 [cited 2025; Available from: https://www.credenceresearch.com/report/automated-fiber-placements-and-automated-tape-laying-machines-market.
16. Yap, T., et al., *In-plane properties of an in-situ consolidated automated fiber placement thermoplastic composite.* Composites Part A: Applied Science and Manufacturing, 2025. **188**: p. 108525.
17. Krueger, R. and A. Bergan, *Advances in thermoplastic composites over three decades–a literature review.* 2024.
18. Costen, R.C. and J.M. Marchello, *Tape-drop transient model for in-situ automated tape placement of thermoplastic composites.* 1998.

19. Hudson, T.B., et al. *Thermal response of thermoplastic composite tape during in-situ consolidation automated fiber placement using a laser heat source*. in *SAMPE Conference and Exhibition 2023*. 2023.

20. Fereidouni, M. and S.V. Hoa, *In-situ consolidation of thermoplastic composites by automated fiber placement: Characterization of defects.* Journal of Thermoplastic Composite Materials, 2025. **38**(2): p. 471-511.

21. Boon, Y.D., S.C. Joshi, and S.K. Bhudolia, *Filament winding and automated fiber placement with in situ consolidation for fiber reinforced thermoplastic polymer composites.* Polymers, 2021. **13**(12): p. 1951.

22. Marathe, U., et al., *4 Bridging conventional manufacturing through hybrid manufacturing processes.* Hybrid Composite Materials and Manufacturing: Fibers, Nano-Fillers and Integrated Additive Processes, 2024: p. 71.

23. Dumont, D., et al., *Interdiffusion of thermoplastics and epoxy resin precursors: investigations using experimental and molecular dynamics methods.* Polymer international, 2012. **61**(8): p. 1263-1271.

24. Zhao, Z., et al., *Study on the overmolding process of carbon-fiber-reinforced poly (aryl ether ketone)(PAEK)/poly (ether ether ketone)(PEEK) thermoplastic composites.* Materials, 2023. **16**(12): p. 4456.

25. Akkerman, R., M. Bouwman, and S. Wijskamp, *Analysis of the thermoplastic composite overmolding process: Interface strength.* Frontiers in Materials, 2020. **7**: p. 27.

26. Andrew Davis, S.H., *Injection Overmolding of Continuous Carbon Fiber Preforms*. 2021, IACMI: http://www.osti.gov/scitech/.

27. Primc, G. and M. Mozetič, *Surface modification of polymers by plasma treatment for appropriate adhesion of coatings.* Materials, 2024. **17**(7): p. 1494.

28. Domonkos, M., et al., *Applications of cold atmospheric pressure plasma technology in medicine, agriculture and food industry.* Applied Sciences, 2021. **11**(11): p. 4809.

29. Lapena, M.H. and C.M.A. Lopes, *Improvement of aerospace thermoplastic composite adhesion to coating with dielectric barrier discharge atmospheric pressure plasma surface treatment.* Plasma Processes and Polymers, 2023. **20**(1): p. 2200081.

30. Turkoglu Sasmazel, H., M. Alazzawi, and N. Kadim Abid Alsahib, *Atmospheric pressure plasma surface treatment of polymers and influence on cell cultivation.* Molecules, 2021. **26**(6): p. 1665.

31. Stepczyńska, M. and A. Śpionek, *Plasma Modification Effects of Thermoplastic Starch (TPS) Surface Layer: Film Wettability and Sterilization.* Materials, 2025. **18**(9): p. 2156.

32. Shaw, D.G., et al., *Accurate and robust static hydrophobic contact angle measurements using machine learning.* Langmuir, 2024. **40**(32): p. 16757-16770.

33. Sena, J., et al., *A Machine Learning Model for the Prediction of Water Contact Angles on Solid Polymers.* The Journal of Physical Chemistry B, 2025. **129**(10): p. 2739-2745.

34. Chiper, A.S. and G. Borcia, *Stable surface modification by cold atmospheric-pressure plasma: Comparative study on cellulose-based and synthetic polymers.* Polymers, 2023. **15**(20): p. 4172.

35. Mathijsen, D., *Long fiber thermoplastics are a key technology in expanding existing markets for composites.* Reinforced plastics, 2019. **63**(5): p. 267-272.

36. Vaidya, U. and K. Chawla, *Processing of fibre reinforced thermoplastic composites.* International Materials Reviews, 2008. **53**(4): p. 185-218.

37. Song, Y., et al., *CAE method for compression molding of carbon fiber-reinforced thermoplastic composite using bulk materials.* Composites Part A: Applied Science and Manufacturing, 2018. **114**: p. 388-397.

38. Nuruzzaman, D., et al. *Experimental investigation on the mechanical properties of glass fiber reinforced nylon*. in *IOP Conference Series: Materials Science and Engineering*. 2016. IOP Publishing.

39. Gupta, M. and K. Wang, *Fiber orientation and mechanical properties of short-fiber-reinforced injection-molded composites: Simulated and experimental results.* Polymer Composites, 1993. **14**(5): p. 367-382.

40. Alwekar, S., et al., *Manufacturing and characterization of continuous fiber-reinforced thermoplastic tape overmolded long fiber thermoplastic.* Composites Part B: Engineering, 2021. **207**: p. 108597.

41. Kim, H.G., *Effects of fiber aspect ratio evaluated by elastic analysis in discontinuous composites.* Journal of Mechanical Science and Technology, 2008. **22**: p. 411-419.

42. Robinson, I. and J. Robinson, *The influence of fibre aspect ratio on the deformation of discontinuous fibre-reinforced composites.* Journal of materials science, 1994. **29**(18): p. 4663-4677.

43. Yeole, P., H. Ning, and A.A. Hassen, *Development and characterization of a polypropylene matrix composite and aluminum hybrid material.* Journal of Thermoplastic Composite Materials, 2021. **34**(3): p. 364-381.

44. Chahine, G., et al., *Hybridizing of glass sheet molding compounds (SMC) with recycled carbon fiber (rCF).* Journal of Composite Materials, 2025: p. 00219983251319590.

45. Marathe, U., et al., *4 Bridging conventional manufacturing through hybrid manufacturing processes*, in *Hybrid Composite Materials and Manufacturing*, K. Vipin, Editor. 2025, De Gruyter: Berlin, Boston. p. 71-88.

46. Heer, N., et al., *Hybrid LFT-D and GMT glass reinforced nylon composite for optimization of part molding and performance.* 2022.

47. Gan, C., *Behavior of grid-stiffened composite structures under transverse loading*. 2003: Wayne State University.

48. Lee, H., et al., *Compressive behavior of automotive side impact beam with continuous glass fiber reinforced thermoplastics incorporating long fiber thermoplastics ribs.* Fibers and Polymers, 2017. **18**: p. 1609-1613.

49. Zhang, L., et al., *Review of automated fibre placement and its prospects for advanced composites.* Journal of Materials Science, 2020. **55**(17): p. 7121-7155.

50. Khodaei, A. and F. Shadmehri, *Intimate contact development for automated fiber placement of thermoplastic composites.* Composites Part C: Open Access, 2022. **8**: p. 100290.

51. Belhaj, M., et al., *Dry fiber automated placement of carbon fibrous preforms.* Composites Part B: Engineering, 2013. **50**: p. 107-111.

52. Georges Chahine, U.M., Liam Collins, Vinoy Thomas, Vipin Kumar, Ahmed Arabi Hassen, Halil Tekinalp, Soydan Ozcan, Uday Vaidya, *Effect of plasma treatment on LMPAEK/CF tape and composites manufactured by automated tape placement (ATP).* Composites Part A: Applied Science and Manufacturing, 2024.

53. Yadav, N. and R. Schledjewski, *Review of in-process defect monitoring for automated tape laying.* Composites Part A: Applied Science and Manufacturing, 2023: p. 107654.

54. Danezis, A., et al., *Heat transfer modelling of flashlamp heating for automated tape placement of thermoplastic composites.* Composites Part A: Applied Science and Manufacturing, 2021. **145**: p. 106381.

55. McArthur, S., et al., *An overview of current research in automated fibre placement defect rework.* Procedia Computer Science, 2024. **232**: p. 2167-2180.

56. Oromiehie, E., et al., *Automated fibre placement based composite structures: Review on the defects, impacts and inspections techniques.* Composite Structures, 2019. **224**: p. 110987.

57. Yassin, K. and M. Hojjati, *Processing of thermoplastic matrix composites through automated fiber placement and tape laying methods: A review.* Journal of Thermoplastic Composite Materials, 2018. **31**(12): p. 1676-1725.

58. Shadmehri, F., et al., *Effect of in situ treatment on the quality of flat thermoplastic composite plates made by automated fiber placement (AFP).* Advanced Manufacturing: Polymer & Composites Science, 2018. **4**(2): p. 41-47.

59. Islam, F., et al., *Modelling the effect of hot gas torch heating on adjacent tows during automated fibre placement consolidation of thermoplastic composites.* Journal of Thermoplastic Composite Materials, 2023. **36**(10): p. 4211-4236.

60. Van Hoa, S., M. Duc Hoang, and J. Simpson, *Manufacturing procedure to make flat thermoplastic composite laminates by automated fibre placement and their mechanical properties.* Journal of Thermoplastic Composite Materials, 2017. **30**(12): p. 1693-1712.

61. Rizzolo, R.H. and D.F. Walczyk, *Ultrasonic consolidation of thermoplastic composite prepreg for automated fiber placement.* Journal of Thermoplastic Composite Materials, 2016. **29**(11): p. 1480-1497.

62. Yeole, P., et al., *Mechanical characterization of high-temperature carbon fiber-polyphenylene sulfide composites for large area extrusion deposition additive manufacturing.* Additive Manufacturing, 2020. **34**: p. 101255.

63. Rahate, A.S., K.R. Nemade, and S.A. Waghuley, *Polyphenylene sulfide (PPS): state of the art and applications.* Reviews in Chemical Engineering, 2013. **29**(6): p. 471-489.

64. Chen, G., A.K. Mohanty, and M. Misra, *Progress in research and applications of Polyphenylene Sulfide blends and composites with carbons.* Composites Part B: Engineering, 2021. **209**: p. 108553.

65. Khan, H., et al., *Continuous, pilot-scale production of carbon fiber from a textile grade PAN polymer.* Materials Today Communications, 2022. **31**: p. 103231.

66. Arquier, R., et al., *Consolidation of Continuous Carbon Fiber-Reinforced PAEK composites: A review.* Materials Today Communications, 2022: p. 104036.

67. Mallick, P.K., *Fiber-reinforced composites: materials, manufacturing, and design*. 2007: CRC press.

68. Wasti, S., et al., *BAMBOO FIBER Overmolding Textile Grade Carbon Fiber Tape and Bamboo Fiber Polypropylene Composites.* SAMPE JOURNAL, 2023. **59**(2): p. 22-29.

69. Nohara, L.B., et al., *Study of crystallization behavior of poly (phenylene sulfide).* Polímeros, 2006. **16**: p. 104-110.

70. Perez-Martin, H., et al., *Crystallinity studies of PEKK and carbon fibre/PEKK composites: A review.* Composites Part B: Engineering, 2021. **223**: p. 109127.

71. Wool, R.P., *Polymer entanglements.* Macromolecules, 1993. **26**(7): p. 1564-1569.

72. Zhao, D., et al., *Crystallization mechanism and mechanical properties of CF/PPS thermoplastic composites manufactured by laser-assisted automated fiber placement.* Journal of Composite Materials, 2023. **57**(1): p. 49-61.

73. Gürler, N., S. Paşa, and H. Temel, *Silane doped biodegradable starch-PLA bilayer films for food packaging applications: Mechanical, thermal, barrier and biodegradability properties.* Journal of the Taiwan Institute of Chemical Engineers, 2021. **123**: p. 261-271.

74. Wei, H., et al., *Adhesion and cohesion of epoxy-based industrial composite coatings.* Composites Part B: Engineering, 2020. **193**: p. 108035.

75. Jarukumjorn, K. and N. Suppakarn, *Effect of glass fiber hybridization on properties of sisal fiber–polypropylene composites.* Composites Part B: Engineering, 2009. **40**(7): p. 623-627.

76. Paramasivam, A., M.V. Timmaraju, and R. Velmurugan, *Influence of preheating on the fracture behavior of over-molded short/continuous fiber reinforced polypropylene composites.* Journal of Composite Materials, 2021. **55**(29): p. 4387-4397.

77. Trauth, A. and K.A. Weidenmann, *Continuous-discontinuous sheet moulding compounds–effect of hybridisation on mechanical material properties.* Composite Structures, 2018. **202**: p. 1087-1098.

78. Fu, S.-Y., et al., *Tensile properties of short-glass-fiber-and short-carbon-fiber-reinforced polypropylene composites.* Composites Part A: Applied Science and Manufacturing, 2000. **31**(10): p. 1117-1125.

79. Cantwell, W.J. and J. Morton, *The impact resistance of composite materials—a review.* composites, 1991. **22**(5): p. 347-362.

80. Composites, T.A., *Toray Cetex TC1100 PPS.*

81. Cassie, A. and S. Baxter, *Wettability of porous surfaces.* Transactions of the Faraday society, 1944. **40**: p. 546-551.

82. Fu, Q., et al., *The impact of different low-pressure plasma types on the physical, chemical and biological surface properties of PEEK.* Dental Materials, 2021. **37**(1): p. e15-e22.

83. Zhang, S., et al., *Autohesion of plasma treated semi-crystalline PEEK: Comparative study of argon, nitrogen and oxygen treatments.* Colloids and Surfaces A: Physicochemical and Engineering Aspects, 2011. **374**(1-3): p. 88-95.

84. Oehr, C., *Plasma surface modification of polymers for biomedical use.* Nuclear Instruments and Methods in Physics Research Section B: Beam Interactions with Materials and Atoms, 2003. **208**: p. 40-47.

85. Švorčík, V., et al., *Modification of surface properties of polyethylene by Ar plasma discharge.* Nuclear Instruments and Methods in Physics Research Section B: Beam Interactions with Materials and Atoms, 2006. **244**(2): p. 365-372.

86. Chan, C.-M., T.-M. Ko, and H. Hiraoka, *Polymer surface modification by plasmas and photons.* Surface science reports, 1996. **24**(1-2): p. 1-54.

87. Yasuda, H. and T. Hirotsu, *Critical evaluation of conditions of plasma polymerization.* Journal of Polymer Science: Polymer Chemistry Edition, 1978. **16**(4): p. 743-759.

88. Heathman, N., et al., *In situ consolidation of carbon fiber PAEK via laser-assisted automated fiber placement.* Composites Part B: Engineering, 2023. **249**: p. 110405.

89. Korycki, A., et al., *Polyaryletherketone Based Blends: A Review.* Polymers, 2023. **15**(19): p. 3943.

90. Vieille, B., et al., *About the influence of stamping on thermoplastic-based composites for aeronautical applications.* Composites Part B: Engineering, 2013. **45**(1): p. 821-834.

91. Bonhomme, J., et al., *Fractography and failure mechanisms in static mode I and mode II delamination testing of unidirectional carbon reinforced composites.* Polymer Testing, 2009. **28**(6): p. 612-617.

92. Cheng, J., et al., *Failure behavior investigation of a unidirectional carbon–carbon composite.* Materials & Design, 2014. **55**: p. 846-850.

93. Danzi, F., et al., *Longitudinal failure mechanisms and crack resistance curves of unidirectional thermoplastic composites.* Engineering Fracture Mechanics, 2023. **282**: p. 109147.

94. Morent, R., et al., *Plasma surface modification of biodegradable polymers: a review.* Plasma processes and polymers, 2011. **8**(3): p. 171-190.

95. Avcı, R., et al., *Effect of atmospheric plasma treatment and wet blast on adhesion characteristics of carbon fiber reinforced LM-PAEK thermoplastic composites.* Composites Part B: Engineering, 2024. **278**: p. 111394.

96. Barile, M., et al., *Thermoplastic composites for aerospace applications*, in *Revolutionizing aircraft materials and processes*. 2020, Springer. p. 87-114.

97. Biron, M., *Thermoplastics and thermoplastic composites*. 2012: William Andrew.

98. Vaidya, U.K. and K. Chawla, *Processing of fibre reinforced thermoplastic composites.* International Materials Reviews, 2008. **53**(4): p. 185-218.

99. Boulos, M.I., et al., *Plasma in the aerospace industry*, in *Handbook of thermal plasmas*. 2023, Springer. p. 1509-1580.

100. Martines, E., *Special issue "plasma technology for biomedical applications"*. 2020, MDPI. p. 1524.

101. Alkoc, A., et al., *Experimental evaluation of atmospheric plasma treatment effects on different textures of CFRP composite for aircraft applications.* Advanced Composite Materials, 2024. **33**(6): p. 1303-1324.

102. Mandolfino, C., E. Lertora, and C. Gambaro, *Effect of cold plasma treatment on surface roughness and bonding strength of polymeric substrates.* Key engineering materials, 2014. **611**: p. 1484-1493.

103. Memos, G., E. Lidorikis, and G. Kokkoris, *Roughness evolution and charging in plasma-based surface engineering of polymeric substrates: The effects of ion reflection and secondary electron emission.* Micromachines, 2018. **9**(8): p. 415.

104. Noeske, M., et al., *Plasma jet treatment of five polymers at atmospheric pressure: surface modifications and the relevance for adhesion.* International journal of adhesion and adhesives, 2004. **24**(2): p. 171-177.

105. Thurston, R.M., J.D. Clay, and M.D. Schulte, *Effect of atmospheric plasma treatment on polymer surface energy and adhesion.* Journal of Plastic Film & Sheeting, 2007. **23**(1): p. 63-78.

106. Iqbal, H., S. Bhowmik, and R. Benedictus, *Surface modification of high performance polymers by atmospheric pressure plasma and failure mechanism of adhesive bonded joints.* International Journal of Adhesion and Adhesives, 2010. **30**(6): p. 418-424.

107. Chahine, G., et al., *Effect of plasma treatment on LMPAEK/CF tape and composites manufactured by automated tape placement (ATP).* Composites Part A: Applied Science and Manufacturing, 2025. **188**: p. 108540.

108. Composites, T.A., *Toray Cetex® TC1225 LMPAEK™*. 2025.

109. Audoit, J., et al., *Thermal, mechanical and dielectric behaviour of poly (aryl ether ketone) with low melting temperature.* Journal of Thermal Analysis and Calorimetry, 2019. **135**: p. 2147-2157.

110. Fowkes, F.M., *Attractive forces at interfaces.* Industrial & Engineering Chemistry, 1964. **56**(12): p. 40-52.

111. Fu, Q., et al., *Development of sol–gel icephobic coatings: effect of surface roughness and surface energy.* ACS applied materials & interfaces, 2014. **6**(23): p. 20685-20692.

112. Hawker, M.J., A. Pegalajar-Jurado, and E.R. Fisher, *Innovative applications of surface wettability measurements for plasma-modified three-dimensional porous polymeric materials: a review.* Plasma Processes and Polymers, 2015. **12**(9): p. 846-863.

113. Bormashenko, E., et al., *Phenomenological model of wetting charged dielectric surfaces and its testing with plasma-treated polymer films and inflatable balloons.* Colloids and Surfaces A: Physicochemical and Engineering Aspects, 2015. **487**: p. 162-168.

114. Mozetič, M., *Aging of Plasma-Activated Polyethylene and Hydrophobic Recovery of Polyethylene Polymers.* Polymers, 2023. **15**(24): p. 4668.

115. Friedrich, J.F., *The plasma chemistry of polymer surfaces: advanced techniques for surface design*. 2012: John Wiley & Sons.

116. Yasuda, H.K., *Plasma polymerization*. 2012: Academic press.

117. Liston, E., L. Martinu, and M.R. Wertheimer, *Plasma surface modification of polymers for improved adhesion: a critical review.* Journal of adhesion science and technology, 1993. **7**(10): p. 1091-1127.

118. Lee, L.-H., *Roles of molecular interactions in adhesion, adsorption, contact angle and wettability.* Journal of adhesion science and technology, 1993. **7**(6): p. 583-634.

119. Foerch, R., G. Kill, and M. Walzak, *Plasma surface modification of polyethylene: short-term vs. long-term plasma treatment.* Journal of adhesion science and technology, 1993. **7**(10): p. 1077-1089.

120. Morent, R., et al., *Non-thermal plasma treatment of textiles.* Surface and coatings technology, 2008. **202**(14): p. 3427-3449.

121. Tajima, S. and K. Komvopoulos, *Dependence of nanomechanical modification of polymers on plasma-induced cross-linking.* Journal of applied physics, 2007. **101**(1).

Overall Summary

In this dissertation, advanced manufacturing strategies for thermoplastic composites were investigated to overcome key structural and interfacial limitations of long fiber thermoplastics through a continuous fiber overmolding approach. Hybrid laminates were produced by overmolding CFRTP tape onto LFT substrates via ATP, achieving 192% higher flexural strength, 120% higher flexural modulus, and 129% higher tensile strength versus baseline LFT. To enhance interfacial bonding, CFRTP tapes were plasma-treated immediately before placement; 10-second air plasma exposure increased Ra from 0.3 nm to 0.8 nm and surface energy from 38 mJ/m² to 68 mJ/m², leading to 32% higher interlaminar shear strength and 28% reduction in delamination area under 3-point bending and drop-weight impact tests. A semi-empirical logarithmic model was formulated to predict Ra and contact angle evolution as functions of plasma power and exposure time, validated against AFM and goniometer data within 5% error. Demonstrated process speeds of 75 mm/s and cycle times under 5 min indicate direct compatibility with industrial ATP lines. This integrated ATP-plasma methodology thus meets automotive and aerospace targets for lightweight, high-performance structures and can be adapted to other polymer systems and multi-material architectures for scalable, next-generation transportation and energy applications.

Vita

Georges Chahine was born in Beirut, Lebanon. He received the Bachelor of Science degree in Physics and the Master of Science degree in Material Science and Nanotechnology from the Lebanese University in 2019 and 2020, respectively. In 2021, he began his doctoral studies at the University of Tennessee, Knoxville, where he earned the Doctor of Philosophy in Mechanical Engineering in November 2025. During his doctoral studies, Georges conducted research in collaboration with Oak Ridge National Laboratory, focusing on the design and manufacturing of sustainable composite materials, additive manufacturing, and automated tape placement. He contributed to multiple Department of Energy and Office of Naval Research projects and developed many patented technologies. His work has been recognized with several awards, including the Harold Giles Scholarship from the Society of Plastics Engineers and the Composites Excellence Award at CAMX 2022. His research interests include advanced composites manufacturing, sustainable materials, and automated manufacturing processes.